ISSN 1343-2230

CNS-REP-103
March, 2025

Annual Report
2023

Center for Nuclear Study,
Graduate School of Science, the University of Tokyo

Editors
Noritaka Kitamura
Hiroki Nagahama

Center for Nuclear Study

CNS Reports are available from:
Wako-Branch at RIKEN
Center for Nuclear Study,
Graduate School of Science, the University of Tokyo
2-1 Hirosawa, Wako
351-0198, Japan
Tel: +81-48-464-4191
Fax: +81-48-464-4554

Annual Report
2023

Center for Nuclear Study,
Graduate School of Science, the University of Tokyo

Preface

This is the annual report of the Center for Nuclear Study (CNS), Graduate School of Science, the University of Tokyo, for the fiscal year 2023 (April 2023 through March 2024). During this period, numerous research activities in various fields of nuclear physics have been conducted, producing a wide range of fruitful results. This report provides a summary of these research activities. Below are key highlights of the report.

The Center for Nuclear Study aims to elucidate the nature of nuclear system by producing the characteristic states where the Isospin, Spin and Quark degrees of freedom play central roles. These researches in CNS lead to the understanding of the matter based on common natures of many-body systems in various phases. We also aim at elucidating the explosion phenomena and the evolution of the universe by the direct measurements simulating nuclear reactions in the universe. In order to advance the nuclear science with heavy-ion reactions, we develop ECR ion source, CRIB and SHARAQ facilities in the large-scale accelerators laboratories RIBF. The OEDO facility has been developed as an upgrade of the SHARAQ, where a RF deflector system has been introduced to obtain a good quality of low-energy beam. A new project for fundamental symmetry using heavy RIs has been starting to install new experimental devices in the RIBF. We promote collaboration programs at RIBF as well as RHIC-PHENIX and ALICE-LHC with scientists in the world, and host international meetings and conferences. We also provide educational opportunities to young scientists in the heavy-ion science through the graduate course as a member of the department of physics in the University of Tokyo and through hosting the international summer school.

The Low Energy Nuclear Reaction group studies exotic structures in high-isospin and/or high-spin states in nuclei. In the spring of 2023, we focus on the analysis of the experimental data which were obtained before. As a result, the parts of ImPACT17-02-01 and -2, the transmutation of the long-lived fission products with protons and detereons, and the surrogate reaction of the neutron capture reaction, have been published. The data analysis of the other experiments are in progress. In addition, as a pilot experiment of the fusion reaction measurement at OEDO in the future, we launched a new project to evaluate the fusion reaction cross sections of the near symmetric system at HIMAC. Also the ASAGI board for the readout of SR-PPAC is being developed. The CNS GRAPE (Gamma-Ray detector Array with Position and Energy sensitivity) is a major instrument for high-resolution in-beam gamma-ray spectroscopy. The digital signal processing equipment for the GRAPE is under development.

The Exotic Nuclear Reaction group studies various exotic reactions induced by heavy-ion beams. We continued the data analysis of the the double charge exchange ^{48}Ca(^{12}C, ^{12}Be) reaction taken in 2021 for a search of double Gamow-Teller resonance.

The OEDO/SHARAQ group pursues experimental studies with RI beams by using the high-resolution beamline and the SHARAQ spectrometer, and the OEDO for the decelerated RI beams. The uniqueness of the OEDO-SHARAQ system is its versatile performance in low-energy RI production and high-resolution spectroscopy. Since there is no experiment in 2023, we focus on the analysis of the data and maintaining the beam line. The result of SHARAQ11, the search for a trineutron state, has been submitted. The results of the mass-measurement of proton-drip line nuclei has been summarized as a PhD thesis of the University of Tokyo. The experimental study of 0^- strength in nuclei using the parity-transfer charge exchange (^{16}O, ^{16}F) is in the final stage. We are also discussing the future plan of OEDO/SHARAQ.

The main activity of the nuclear astrophysics group is to study astrophysical reactions and special nuclear structures, using the low-energy RI beam separator CRIB. The experiments at CRIB with the presence of international collaborators on-site had been suspended since 2020, but restarted from the ^{14}O(α, p) reaction measurement performed in March, 2023. We carried out an experiment separated into two beamtimes in May 2023 and January 2024, using a ^{6}He beam at CRIB, for measuring ^{6}He+p elastic scattering and ^{6}He(p, t)/(p, d) transfer reactions. To obtain an improved detection efficiency of the ^{6}He beam, multi-wire drift chambers (MWDC) were first introduced for the main measurements at CRIB.

Main goal of the quark physics group is to understand the properties of many-body QCD system such as quark-gluon plasma at extremely high-temperatures and color-glass condensate at extremely high-energies. The group has been involved in the PHENIX experiment at Relativistic Heavy Ion Collider (RHIC) at Brookhaven National Laboratory, the ALICE experiment at Large Hadron Collider (LHC) at CERN, and the ePIC experiment at the Electron-Ion Collider (EIC) at BNL, where the EIC is the future collider project at BNL and will start its operation from 2030. As for ALICE, the group has involved in the data analyses, which include the measurement of low-mass lepton pairs in Pb-Pb collisions, the measurement of long range two particle correlations in p-Pb collisions, searches for thermal photons in high multiplicity pp collisions. The group has involved in the ALICE-TPC upgrade using a Gas Electron Multiplier (GEM), where the group is very active in the development and benchmarking of the online space-charge distortion corrections using machine learning techniques running on the Graphical Processing Unit (GPU). The group has started R&D for the MAPS silicon pixel detector for the ALICE ITS3 and ALICE3 upgrade. The group newly joined in the ePIC experiment for the EIC and started some activities for the development of streaming data acqusition system.

One of the major tasks of the accelerator group is the development of ion sources and the optimization of the beam transport system for the experimental devices installed in the E7 experiment room. In 2023, HyperECR ion source was operated for 1,888 hours. A novel stability control system for the ion source is currently under development using machine learning technology. For the first step, a beam current prediction model was developed using plasma images and control parameters. It was tested on several operation data and performed adequately in some cases. For the development of the pepper-pot emittance monitor, the experiment was planned and performed in the MALT (Micro Analysis Laboratory, Tandem accelerator, The University of Tokyo) to search the measurement error. The prototype of the beam shutter system to devoid heating the monitor while exposing ion beam was tested. The shutter speed was achieved within 0.27 second.

The development of a quantum sensor to search for a permanent electric dipole moment (EDM) with an optical lattice interferometer is in progress at RIKEN RIBF. In this fiscal year, we have developed a thermal ^{221}Fr atom source for its magneto-optical trapping. This new device allows to continuously supply thermal ^{221}Fr atoms into a magneto optical trap system, as a consequence realizing a large amount of laser-cooled ^{221}Fr atoms used for the EDM measurement. As the measurement precision strongly depends on the number of trapped ^{221}Fr, the newly developed apparatus is essential towards searching the EDM with high precision.

The nuclear theory group is conducting large-scale shell-model calculations, having a strong relationship to the project “Program for Promoting Researches on the Supercomputer Fugaku”. One of the key achievements in FY2023 is investigation of triaxiality based on our calculations reproducing rotational bands of nuclei around ^{166}Er. We are also performing shell-model calculations for the structure of neutron-rich nuclei in collaboration with experiments carried out in RIBF, RIKEN, focusing on the region around ^{54}Ca. In FY2023, we have accepted two graduate students from the University of Oslo, and instructed them on skills of large-scale shell-model calculations for analyzing experimental data concerning the Oslo method.

The 22nd CNS International Summer School (A3F-CNSSS23) took place from August 4 to 10, 2023. The school was organized by CNS and co-hosted by the Super Heavy Element Center (RCSHE) and the Center for Accelerator and Beam Applied Science (CABAS) at Kyushu University, with support provide by the JSPS A3F program. The shool was held in cooperation with the RIKEN Nishina Center and the Asian Nuclear Physics Association (ANPhA). This year, the school returned to an in-person format for the first time since 2019. The school, held in Nishina Hall at RIKEN, featured 7 lecturers and welcomed a total of 87 attendees, including five from Korea, five from India, and one from Vietnam.

Finally, I would like to thank Mr. Hoso and the other administrative staff members for their contributions throughout the year.

Yasuhiro Sakemi
Director of CNS
Yasuhiro Sakemi

Table of Contents

1a. Experimental Nuclear Physics: Low and Intermediate Energies

1b. Experimental Nuclear Physics: PHENIX Experiment at BNL-RHIC and ALICE Experiment at CERN-LHC

2. Accelerator and Instrumentation

3. Theoretical Nuclear Physics

4. Other Activities

Appendices

Experimental Nuclear Physics: Low and Intermediate Energies

Studying the impact of deuteron non-elastic breakup on ^{93}Zr + d reaction cross sections measured at 28 MeV/nucleon

T. Chillery, J. W. Hwang[a], M. Dozono[b], N. Imai, S. Michimasa,
T. Sumikama[c], N. Chiga[c], S. Ota[d], S. Nakayama[e]
for the ImPACT Collaboration

Center for Nuclear Study, Graduate School of Science, University of Tokyo
[a] *Center for Exotic Nuclear Studies, Institute for Basic Science (IBS), Daejeon 34126, Rep. of Korea*
[b] *Graduate School of Science, Kyoto University, Sakyo, Kyoto 606-8501, Japan*
[c] *RIKEN Nishina Center for Accelerator-Based Science, Wako, Saitama 351-0198, Japan*
[d] *Research Center for Nuclear Physics, Osaka University, Ibaraki, Osaka 567-0047, Japan*
[e] *Nuclear Data Center, Japan Atomic Energy Agency, Ibaraki, Japan*

Owing to the deuteron's low binding energy it is easily broken apart by the Coulomb and nuclear fields of a target nucleus. This non-elastic breakup enhances deuteron-induced reaction cross sections at energies above 50 MeV/nucleon [1, 2], where comparisons between measured data and statistical model outputs (i.e. DEURACS and TALYS) help improve our understanding of the underlying breakup mechanisms. However, there remains a lack of data at energies below 30 MeV/nucleon for long-lived fission product (LLFP) ^{93}Zr. To address this, in 2017 the optimized energy degrading optics [3] (OEDO) system was used to measure ^{93}Zr + d reaction cross sections at 27.7 MeV/nucleon, which is the lowest energy to date. This result may also assist transmutation facilities with treatment of ^{93}Zr ($T_{1/2}$ = 1.61 Myr) which remains a challenging LLFP in the treatment of nuclear waste. This report summarises the recently published letter [4] presenting the final results.

The ^{93}Zr secondary beam was produced in the BigRIPS separator from in-flight fission of 345 MeV/nucleon ^{238}U with a ^{9}Be 5 mm thick target. The beam was transported through the OEDO beamline with intensity 1.2 kpps, where it was used to bombard a cryogenically-cooled ($\simeq$ 40 K) 16.9 mg/cm^2 thick, 55 mm long deuterium gas target [5] installed at focal-plane S0. The gas target included Havar windows of approximately 10 µm thickness. The beamspot at S0 was focused using the OEDO radio-frequency deflector (RFD) and superconducting triplet quadrupole magnets, installed upstream of FE12. Details of the RFD's function are provided in Ref. [3]. The beamspot size at S0 in FWHM was 40 mm (12 mm) in X (Y). Fig. 1 shows a diagram of the OEDO-SHARAQ beamline around the S0 target.

Reaction products from the D$_2$ target were collected and momentum-analyzed by the SHARAQ spectrometer operating in QQD mode [6]. For each run, the SHARAQ D1 dipole magnet was set to one of five magnetic rigidity ($B\rho$) settings $\Delta B\rho/B\rho_0 = -9.5\%, -5.5\%, -1.5\%, +2.5\%$, and $+6.0\%$ where 0% is the central beam trajectory ($B\rho_0$ = 1.6210 Tm). Tracking and timing information from parallel plate avalanche counters were used to calculate the products' mass-to-charge (A/Q). Towards the back of S0 a 30 pad ionization chamber (IC) with 750 mm active depth filled with 130 Torr CF$_4$ gas was used to stop the beam and products, thus measuring their Bragg peaks for particle identification (PID). The Bragg curves were fitted event-by-event to extract mass (A) and atomic numbers (Z). The Z vs IC depth of ions is plotted in Fig. 2. Clear beam contamination is present in the Z = 41 region around range 755 mm, and this was resolved by applying two-dimensional cuts on the Z vs range to separate each fragment: Nb, Zr, and Y.

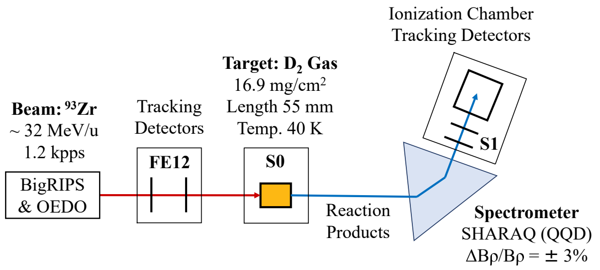

Figure 1: Diagram of experimental setup around the S0 target, see text for details.

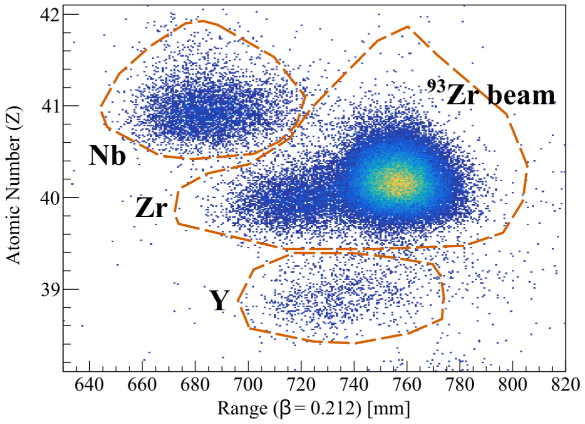

Figure 2: Atomic number (Z) vs range of ion ($\beta = 0.212$) in IC at SHARAQ setting $\Delta B\rho/B\rho_0 = -1.5\%$. Dashed lines represent the two-dimensional cuts used to select each Z.

The final PID was achieved by plotting A vs A/Q gated on each Z locus, shown in Fig. 3. Several loci are observed for the same isotope owing to the wide charge-state distributions encountered at this low energy, ~ 23.2 MeV/nucleon at S1. The total counts for all charge states were extracted from a dominant charge-state based on the deduced distribution in the present data. Consequently, the production cross-sections for individual fragments were calculated.

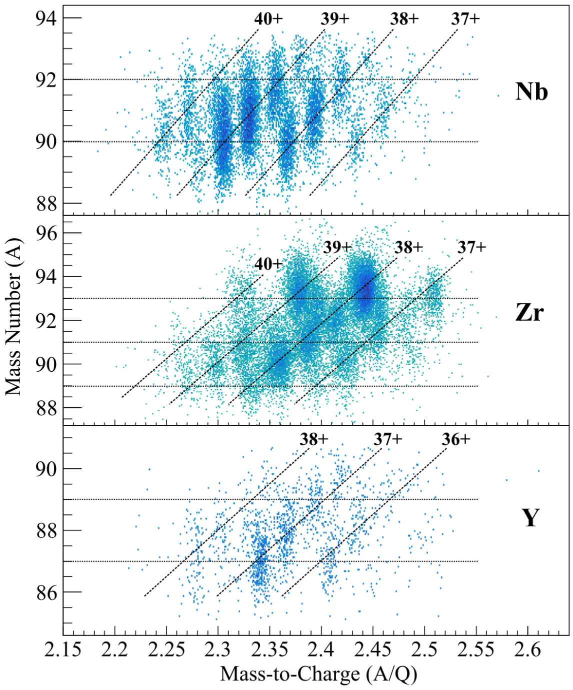

Figure 3: Mass number (A) vs mass-to-charge (A/Q) particle identification plot for SHARAQ setting $\Delta B\rho/B\rho_0 = -1.5\%$, gated on Z-loci in Fig. 2. Dashed lines are to guide the eye.

The ^{93}Zr + d cross sections as a function of incident deuteron energy are shown in Fig. 4. Measured data from this study are plotted at 55.8 MeV, where the hatched band represents the energy range covered in the D_2 target. The data of previous studies [7,8] are plotted at higher energies. The solid lines represent the DEURACS calculations, and dotted/dashed lines represent the TALYs calculations considering different deuteron breakup models. Our data was in quantitative agreement with the output of DEURACS and, in the case of Nb and Zr isotopes, TALYS. At our low energy the alpha emission channels dominate Y production, and thus the TALYS alpha optical model potential was adjusted to the Nolte model to best match the experimental data. However, the calculations still underestimate Y-production cross sections up to a factor 3 (11) using the Avrigeanu (Kalbach) breakup model. Future efforts are required for theory to better describe our new results and improve deuteron breakup models across the widest possible energy range.

Regarding our results impact on transmutation of nuclear waste, the increased Nb production may limit the effectiveness of low-energy deuteron-based treatments, simply because the half-lives of some products can be exceedingly long, importantly ^{92}Nb with $T_{1/2}$ = 34.7 Myr. The situation may be more complicated during transmutation at accelerator-based facilities, where nuclei produced from ^{93}Zr + d reactions may react with the deuteron beam themselves. Additionally, light nuclei produced in the beam-target interactions may continue to transmute the surrounding target material and improve transmutation yields. In future, detailed transmutation simulations should be performed using an extensive reaction network around the ^{93}Zr region.

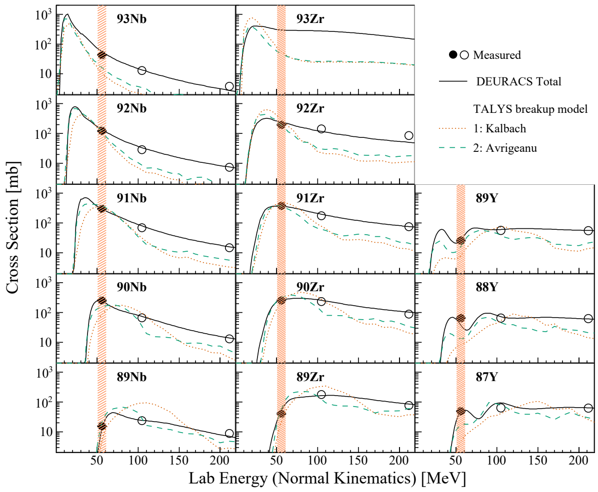

Figure 4: Cross sections for ^{93}Zr + d reactions as a function of lab energy (normal kinematics). Total error bars are smaller than the marker sizes. Black lines are from DEURACS calculations, and dashed (dotted) lines are from TALYS v1.96 calculations using Avrigeanu (Kalbach) breakup model.

In summary, the present data helps constrain models of deuteron-breakup on reaction cross sections and may assist accelerator-driven transmutation systems in their efforts to treat ^{93}Zr in nuclear waste. In future, coincidence measurements detecting evaporated light particles and γ-ray emissions alongside the heavy residual particles would be helpful.

References

[1] M. Avrigeanu *et al.* Eur. Phys. J. A **58** 3 (2022).
[2] S. Nakayama *et al.* J. Nucl. Sci. Technol. **58:7** 805-821 (2021).
[3] S. Michimasa *et al.* PTEP **2019** 043D01 (2019).
[4] T. Chillery *et al.* PTEP **2023** 121D01 (2023).
[5] H. Ryuto *et al.* NIM A **555** 1-5 (2005)
[6] S. Michimasa *et al.* NIM B **540** 194–198 (2023).
[7] K. Nakano *et al.* In EPJ Web of Conferences, **239** 20006 (2020).
[8] S. Kawase *et al.* PTEP **2017** 093D03 (2017).

Data analysis of the ^{130}Sn(d,p)^{131}Sn transfer reaction study performed at OEDO-SHARAQ

T. Chillery[a], N. Imai[a], S. Michimasa[a], D. Suzuki[b], D.S. Ahn[c], A. Chae[d], S. Cherubini[e], M. La Cognata[f], M. Dozono[g], M. Egeta[h], F. Endo[h], N. Fukuda[b], T. Haginouchi[h], S. Hanai[a], S. Hayakawa[a], J.W. Hwang[c], Y. Hijikata[b,g], S. Ishio[h], N. Iwasa[h], K. Kawata[a], S. Kubono[b], R. Kojima[a], L. Lamia[e], J. Li[a], N. Nishimura[b], K. Okawa[a], H.J. Ong[i], S. Ota[j], S. Palmerini[k], R.G. Pizzone[f], T. Saito[a], Y. Shimizu[b], S. Shimoura[a,b], T. Sumikama[b], H. Suzuki[b], H. Takeda[b], A. Tumino[f,l], X. Tang[i], H. Tanaka[m], M. Tanaka[b], T. Teranishi[m], Y. Togano[b], R. Yokoyama[a], R. Yoshida[f], K. Yoshida[b], M. Yoshitomo[b], Y. Wang[n], and Z. Xiao[n]

[a]CNS, University of Tokyo, [b]RIKEN Nishina Center, [c]CENS, IBS, [d]Sonkyunkwan University, [e]University of Catania, [f]INFN, LNS, [g]Kyoto University, [h]Tohoku University, [i]Institute of Modern Physics, [j]RCNP, Osaka University, [k]INFN sezione di Perugia, [l]Kore University of Enna, [m]Kyushu University, [n]Tsinghua University

The rapid (*r*) neutron-capture process is the prevailing theory to explain the origin of about half the heavy elements beyond iron [1]. The theory relies on inputs from β-decay rates, nuclear masses, and neutron-capture reaction rates. Focusing on the reaction rates, there remains a lack of data for neutron-rich nuclei and the model must therefore rely on theoretical inputs. In particular, the neutron-capture rate on tin isotopes around the N = 82 shell gap are unmeasured, and different models show disagreement up to several orders of magnitude [2]. There is a lack of knowledge on both the unbound states in the compound nuclei and their gamma-decay emission probabilities. These uncertainties make it challenging to definitively identify nucleosynthesis sites where the *r*-process occurs. To help in bridging this gap, a recent experimental campaign [3] was performed at the Radioactive Ion Beam Facility (RIBF) using the Optimised Energy Degrading Optics (OEDO) beamline [4, 5] to study the ^{130}Sn(n,γ)^{131}Sn reaction using the surrogate ratio technique via (d,p) transfer reactions. This report details the experimental setup and the preliminary data analysis performed during 2023.

The experiment was performed at the RIBF facility using the BigRIPS-OEDO beamline combined with the SHARAQ spectrometer. A cocktail beam including the radioactive ion (RI) ^{130}Sn was produced by in-flight fission of ^{238}U on a ^{9}Be target. The ^{130}Sn ions were identified event-by-event using 2D information of their time-of-flight and x-position near the start of OEDO, as shown in Fig. 1a, and hereinafter “beam" refers to ^{130}Sn only. The beam energy was degraded from 170 MeV/nucleon to 23.6 MeV/nucleon using a 5 mm thick angle-tuneable (6 mrad) wedge-shaped aluminium degrader.

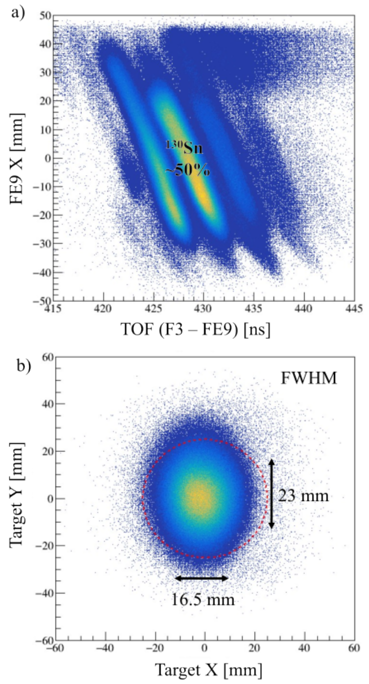

Figure 1: Beam properties measured at OEDO. a) Beam PID using X-position at wedge degrader (FE9) vs time-of-flight through BigRIPS-OEDO. $\sim$ 50% purity achieved for ^{130}Sn. b) Beamspot at secondary target (S0) position in TiNA. Red circle represents the target diameter of 50 mm.

A schematic of the setup around the target is provided in Fig. 2. Using superconducting triplet quadrupole magnets and the radio-frequency deflector (details in [5]) the beam was focused through OEDO onto a 287 μg/cm^2 CD$_2$ solid target mounted at S0. As shown in Fig. 1b the achieved beam spread in X (Y) had a FWHM of 16.5 mm (23 mm), within the targets 50 mm diameter. Installed at backward angles to the target, the charged-particle detection array “TiNA” consists of $dE - E$ telescopes constructed of (double-sided) silicon strip detectors ((D)SSD) and CsI scintillators. These detected light particles from beam-target interactions, in particular the protons of interest from ^{130}Sn(d,p). Downstream from the target the SHARAQ spectrometer was operated in QQD mode to separate and identify heavy ions. Tracking detectors installed before and after SHARAQ were used to measure the ions position and time-of-flight. At the end of S1 reaction products and any unreacted beam were deposited in a 30 pad ionisation chamber (IC) of 750 mm active depth filled with 130 Torr CF$_4$ gas, thus allowing to measure their Bragg curves and extract mass (A) and atomic numbers (Z) for particle identification.

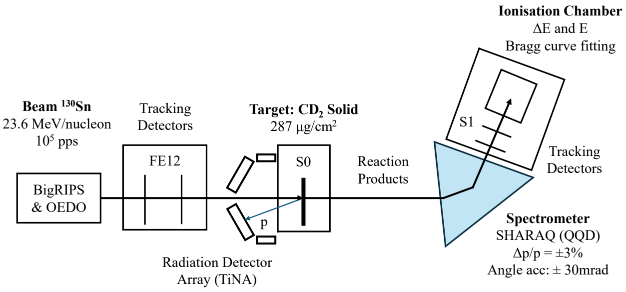

Figure 2: Schematic diagram of the experimental setup around the secondary target at S0. More details in the text.

The magnetic rigidity ($B\rho$) and flight-path-length (FPL) of the ions were determined via a multidimensional fit of the SR-PPAC tracking and timing information, using the beam events as reference and the SHARAQ dipole setting as central $B\rho$. The mass to charge (A/Q) was then determined via the equation

$$\frac{A}{Q} = \frac{B\rho}{\beta\gamma}\frac{e}{c \cdot m_u},$$

where γ is the Lorentz factor, β is velocity (FPL/TOF) scaled to the speed of light c, and $\frac{e}{c \cdot m_u}$ is a constant (0.3214 C·s·kg^{-1}·m^{-1}). The A/Q using velocity information either upstream or downstream of SHARAQ is shown in Fig. 3, where a resolution of 0.27% is achieved for ^{130}Sn^{47+}.

The TiNA detectors were energy calibrated using a standard triple alpha source and separately collected data of ^{130}Sn(Al,p). The $dE-E$ plot from TTT silicon detectors and CsI scintillators is provided in Fig. 4, where Z of light ions is proportional to $\sqrt{dE * E_{\text{total}}}$.

In summary the BigRIPS-OEDO beamline successfully produced low energy ^{130}Sn beam in spring 2022. Beam was focused onto a CD$_2$ solid target, with the heavy reaction products collected by the SHARAQ spectrometer and the light ions measured at backward angles using the TiNA array. A/Q information was extracted from the tracking information, and the protons of interest were identified using the $dE-E$ detectors. Work is now ongoing to extract the excitation energy spectrum using these proton energies combined with A/Q information from SHARAQ, and also to analyse the IC data for A and Z information of the heavy ions. Once the correspondence between TiNA and SHARAQ data is confirmed, the missing mass and angular distribution information will be extracted.

References

[1] T. Kajino *et al.* PPNP **107** 109-166 (2019).
[2] M.R. Mumpower *et al.* PPNP **86** 86-126 (2016).
[3] N. Imai *et al.* CNS Annual Report 2022.
[4] S. Michimasa *et al.* NIM B **540** 194–198 (2023).
[5] S. Michimasa *et al.* PTEP **2019** 043D01 (2019).

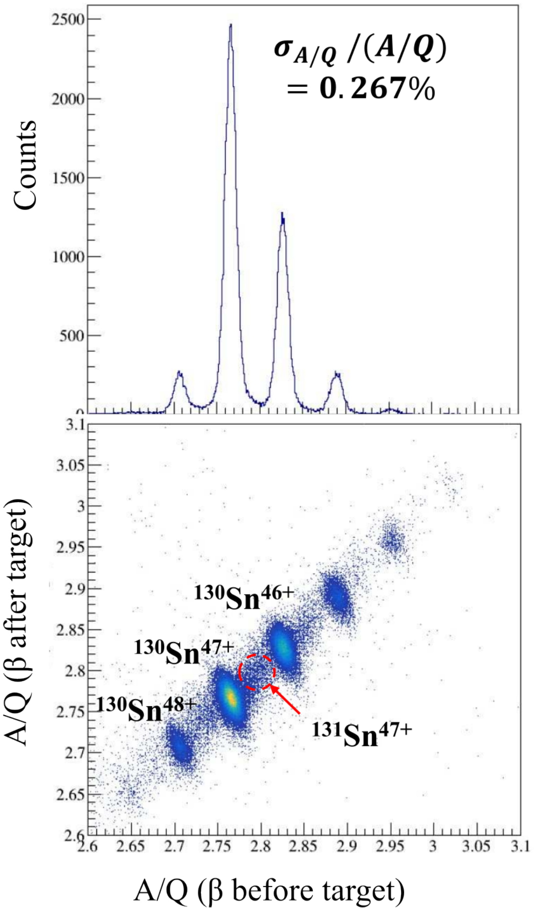

Figure 3: a) Mass-to-charge (A/Q) obtained at SHARAQ using velocity (β) upstream of target. Dominant peaks observed are different charge states of ^{130}Sn beam. b) 2D plot of A/Q measured at SHARAQ using different β. Region corresponding to ^{131}Sn^{47+} has been circled in red.

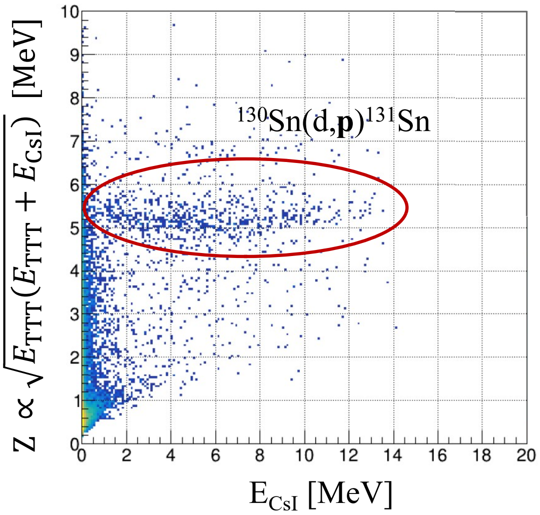

Figure 4: Energy spectrum measured at TiNA using TTT Silicon detectors (E_{TTT}) and CsI scintillators (E_{CsI}). The Y-axis is analogous to the atomic number of the detected nuclei. The proton energy region from ^{130}Sn(d,p)^{131}Sn is circled in red.

Neutron capture reaction cross-section of ^{79}Se through the ^{79}Se(*d,p*) reaction in inverse kinematics[1]

N. Imai, M. Dozono[a], S. Michimasa, T. Sumikama[b], S. Ota[c], S. Hayakawa, J.W. Hwang[d], K. Iribe[e], C. Iwamoto, S. Kawase[f], K. Kawata, N. Kitamura, S. Masuoka, K. Nakano[f], P. Schrock, D. Suzuki[b], R. Tsunoda, K. Wimmer[2g], D.S. Ahn[d], O. Beliuskina, N. Chiga[b], N. Fukuda[b], E. Ideguchi[c], K. Kusaka[b], H. Miki[h], H. Miyatake[i], D. Nagae[h], S. Omika[j], H.J. Ong[c], H. Otsu[b], H. Sakurai[b], H. Shimizu, Y. Shimizu[b], X. Sun[b], H. Suzuki[b], M. Takaki, H. Takeda[b], S. Takeuchi[h], T. Teranishi[e], Y. Watanabe[f], Y.X. Watanabe[i], K. Yako, H. Yamada[h], H. Yamaguchi, L. Yang, R. Yanagihara[c] Y. Yanagisawa[b], K. Yoshida[b], and S. Shimoura,

Center for Nuclear Study, Graduate School of Science, University of Tokyo
[a]*Department of Physics, Kyoto University*
[b]*RIKEN Nishina Center*
[c]*RCNP, Osaka University*
[d]*CENS, Institute of Basic Science*
[e]*Department of Physics, Kyushu Univ.*
[f]*Department of Advanced Energy Science and Engineering, Kyushu Univ.*
[g]*Department of Physics, Univ. of Tokyo*
[h]*Department of Physics, Tokyo Insititute of Technology*
[i]*WNSC, IPNS, KEK*
[j]*Department of Physics, Saitama University*

The neutron capture reaction cross-sections are important for understanding the origin of the elements in the universe as well as for the nuclear engineering. In some cases, the target nuclei are radioactive so that the measurement of the cross section is not feasible.

Though the halflife of ^{79}Se is as long as 3.2×10^5 years, it is still difficult to make an enriched target, which hinders measuring the direct neutron capture cross sections. This nucleus is located on the path of s-process nucleosynthesis. Because the first excited state has a β decay branch, the ratio of the daughter nucleus ^{79}Br to ^{80}Se can determine the temperature when the s-process took [1]. However, although the main path of the s-process is the neutron capture to proceed to ^{80}Se, because ^{79}Se is radioactive, the neutron capture cross section on ^{79}Se has not been measured directly.

The nucleus is also known as one of the long-lived fission products (LLFPs) of the nuclear wastes. It is supposed to be stored for millions of years in the deep geological repository, which has not been determined yet in Japan [2]. The transmutation of such LLFPs would be a possible way to avoid the inheriting of the nuclear waste to the future. To design the facility for the transmutation, cross sections of any neutron induced reactions must be evaluated precisely.

In the past, the neutron capture cross section was evaluated by measuring the photon strength function [3]. The neutron capture was deduced from the strength function assuming the level density, which are strongly model-dependent. As a result the evaluated cross section have a large uncertainty of a factor 7.

To evaluate the cross section of ^{79}Se(n,γ) independently, a surrogate ratio technique [4] was employed. In general, the compound neutron capture reaction is considered to be composed of two factors: the formation cross section of the compound states and the γ decay probability from the unbound states. The energy-dependent formation cross section can be obtained by using the global optical potential. On the other hand, the γ emission probability strongly depends on the nuclear structure of the nucleus. Once the γ emission probability is obtained experimentally, the neutron capture cross sections can be determined. In the surrogate method, the same unbound states as those populated by the compound reaction are assumed to be excited by an alternative nuclear reaction such as (*d, p*) reaction. In the case of (*d, p*) reaction, the excitation energy can be determined by measuring the recoiled protons. Therefore, when γ emission channel at each excitation energy is identified, the neutron capture cross section can be determined.

So far, for the surrogate ratio method, the γ emission probability was determined by measuring deexcitation γ rays which requires the decay scheme from the unbound state. On the other hand, in our new method, the probability was determined by measuring reaction residues in coincidence with the recoiled proton, instead of measuring γ ray. The transfer reaction in the inverse kinematics made feasible the measurement. In this study, we also measured the ^{77}Se$(d,p)^{78}$Se reaction as well as ^{79}Se$(d,p)^{80}$Se. Since the ^{77}Se$(n,\gamma)^{78}$Se reactions were already measured at 550 keV, we can verify the method by ^{77}Se$(n,\gamma)^{78}$Se reaction cross section by using the surrogate method.

The secondary ^{77,79}Se beams were produced at RIBF by the in-flight fission of ^{238}U beams with a rotating Be target of 3 mm thickness. By tuning the thicknesses of the

---

[1] Condenced report of Physics Letters B 850, 138470 (2024).

[2] Present Address:GSI, Darmstdt, Germany

degraders at F1 and F2 the beam energy was adjusted to 120 MeV/nucleon at F5. The beam energy was degraded with a thick Al degrader at F5 to 23 MeV/nucleon.

The energy was further degraded to 20 MeV/nucleon at the secondary target by passing through the beam line detectors of parallel plate avalanche counte (PPAC)s. Diamond detectors of 3×3 cm^2 and 300 μm thickness were placed at F3 and F5 to measure the timing when the beam passed through. The small active area of the diamond limited the momentum slit at F1 $\pm 1\%$. The narrow momentum slit and good time resolution enabled us to identify the beam only with the time-of-flight (TOF) between F3 and F5.

Two PPACs were installed upstream of the secondary target, FE12, to register the timing and the trajectory of the beams on the target. TOF between F5 and FE12 was measured to measure the respective beam energy. The RF deflector at OEDO decreased the beam spot in a diameter of 2 cm (σ) at a deuterated polyethylene CD$_2$ target of 4 mg/cm^2 thickness. The target size was 3 cm in diameter. The recoiled particles of (d, p) reactions were detected by six telescopes, each of which consisted of SSD at the first layer and two CsI(Tl)s detectors at the second layer. The telescope covered the scattering angles from 100 to 150 degrees in the laboratory frame. The SSD was divided to 16 channels in polar angle. The momenta of the outgoing nuclei were analyzed by the first part of the SHARAQ spectrometer. At the exit of the D1 magnet of the spectrometer, two PPACs and an ionization chamber were installed as the focal plane detectors. PPACs gave us the TOF of ions. The trajectory obtained from PPACs also gave the $B\rho$ values of the residual nuclei. The ionization chamber yielded the energy loss (dE) and the range in the gas. The TOF-dE-range and $B\rho$ information enables us to identify the ions.

In the surrogate ratio method, the spin distribution of the reference nucleus is required to be the same as that of the reaction of the interest. In the present case the ground state spin parity of ^{77}Se is $1/2^-$, while that of ^{79}Se is $7/2^+$. On the other hand, both nuclei have the long-lived isomeric states. The spin parity of the isomers for ^{77,79}Se are $7/2^+$ and $1/2^-$, respectively.

The isomer ratio was measured to be $87 \pm 7\%$ in ^{77}Se beams. On the other hand, for ^{79}Se the ratio was measured to be $29 \pm 7\%$ in the past experiment at RIBF with the same primary beam of ^{238}U and the Be target [5]. Considering that the fission reaction produces the high excited states, the isomer ratio can be considered as a result of the number of the magnetic substates of $7/2^+$ and $1/2^-$. Namely, the $7/2^+$ state was around 80% in both the beams.

The spin distributions of the neutron capture reactions are compared to those of the transfer reaction in Fig. 2. The panel (a) shows spin distributions for the neutron capture reactions on ^{79}Se($7/2^+$) (solid) and the isomeric state of ^{79}Se($^*1/2^-$) (dashed) with 0.2 MeV. The spin distribution on the isomeric state centers around $J = 2$. The panel (b) compares the spin distributions on ^{77}Se ground state of $1/2^-$ (solid) and the isomeric state of $7/2^+$ (dashed). These two figures clearly demonstrate that the spin of the target nuclei are important to determine the cross sections by the surrogate ratio method. The panel (c) presents the spin distributions of the transfer reactions on the ground states of ^{77,79}Se by dashed and solid lines, respectively. The spin distribution are found to be the same, indicating that the contamination of the isomeric states in ^{77,79}Se beams won't affect the final result.

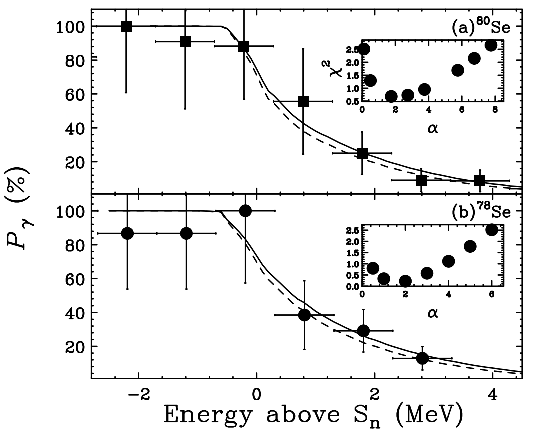

Figure 1: Experimental P_γ for (a) ^{80}Se and (b) ^{78}Se, respectively, as a function of the excitation energy above S_{1n}. The solid and dashed lines are the γ emission probabilities using different models of the level density [6,7]. The insets of both panels present the χ^2 distributions as a function of α.

The experimental P_γs for ^{78}Se and ^{80}Se obtained by the (d, p) reaction are shown in Figs. 1(a) and (b). Although the statistical error is large, the P_γ for ^{80}Se was observed to be larger than that for ^{78}Se at around 1 MeV. The P_γ values from the excited states after the binary reaction were calculated using TALYS-1.9, where the spin distribution in each excitation energy, and the γ emission probabilities from a given excitation energy and spin were accounted for. In the calculation, the spin-distributions assuming the pre-equilibrium reaction of Fig.2(a) were adopted. P_γ curves for ^{78,80}Se which include the excitation-energy dependence of the energy resolution are presented in Figs. 1(a) and (b). The solid (dashed) curves are the results with the Constant Temperature + Fermi Gas model [6] (Back-shifted Fermi-gas model [7]) for the level density. The theoretical P_γ curves for both nuclei are reasonably in agreement with the experimental P_γ values.

The (n, γ) cross-sections were also evaluated from $E_n =$ 0.8 to 4 MeV in 1 MeV steps by employing the surrogate ratio method. Because the ground state spins of ^{77,79}Se are different, the cross-sections of ^{77}Se$_{g.s.}(n, \gamma)$ cannot be used as the first term in Eq. (1) to determine the cross-sections of the ^{79}Se$_{g.s.}(n, \gamma)$ reaction. In Figs. 2 (c) and (d), calculations of the neutron capture reaction at $E_n = 0.2$ MeV with both the ground state (solid line) and the isomeric state (dashed line) of ^{77,79}Se are presented. The total spin distribution depends on the initial spin of the target nucleus. In (c), the results with $E_n = 0.2, 3$ MeV are presented, indicating as the neutron energy increases, spin-populations with the ground and the isomeric state gets closer to each other, but they are not identical, as in the case of the transfer reactions in (a).

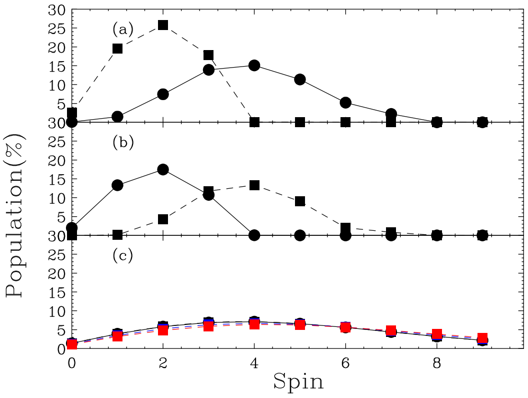

o

Figure 2: The spin distribution of nuclear reactions. (a) those for neutron capture reactions on ^{79}Se(g.s.) (solid) and the isomeric state (dashed). (b) those for neutron capture reactions on ^{77}Se(g.s.) (solid) and the isomeric state (dashed). (c) those for neutron transfer reactions on ^{77}Se(g.s) (dashed) and ^{79}Se(g.s.) (solid). See the text for details.

The cross-sections using the surrogate-ratio method support TENDL2019 rather than TENDL2017 and TENDL2021 which are lower than the presented results of the surrogate-ratio method.

In summary, we studied the one-neutron transfer reaction on the long-lived radioactive isotope of ^{79}Se in the inverse kinematics at approximately 20 MeV/nucleon. The gamma emission probabilities of the unbound states were directly determined by identifying the reaction residues instead of measuring γ rays. Although the total spin distribution populated by the transfer reaction was calculated to be different from those of the neutron capture reactions around $E_n \simeq 1$ MeV, the normalization factor of Γ_γ determined by the transfer reaction was able to evaluate the neutron capture cross-sections with the theoretical spin distribution. The presented result of the surrogate-ratio method is consistent with TENDL2019, JENDL-5.0 and ENDF/B-VIII.

Acknowledgments

We would like to thank the RIKEN Nishina Center and the CNS, the University of Tokyo, accelerator staff for their excellent beam delivery. This study was supported by the ImPACT Program of the Council for Science, Technology and Innovation (Cabinet Office, Government of Japan), JSPS KAKENHI Grant Numbers 19H01903 and 19H01914. We are grateful to Prof. Z.G. Xiao, Dr. O. Iwamoto, and Dr. A. Mengoni for their valuable discussions on the presented result. N.I. would like to thank Dr. A. Makinaga for providing their numerical data.

References

[1] F. Kappler, H. Beer, and K. Wisshak, Rep. Prog. Phys. **52**, 945 (1989).
[2] https://www.numo.or.jp/en/ .
[3] A. Makinaga et al., Phys. Rev. C **94**, 044304 (2016).
[4] J. E. Escher et al., Rev. Mod. Phys. **84**, 353 (2012).
[5] S. Takeuchi et al. RIKEN Accel. Prog. Rep. **49**, 86 (2016).
[6] A. Gilbert and A.G.W. Cameron, Can. J. Phys. **43**, 1446 (1965).
[7] W. Dilg, W. Schantl, H. Vonach, and M. Uhl, Nucl. Phys. A **217**, 269 (1973).

TOF-Bρ mass measurement of proton-rich pf-shell nuclei using SHARAQ spectrometer

S. Hanai[a], S. Michimasa[a], N. Imai[a], R. Yokoyama[a], D.S. Ahn[b], M. Amitani[c,d], H. Baba[d], T. Chillery[a], M. Dozono[e,d], F. Endo[f,d], M. Fukuda[g,d], N. Fukuda[d], C. Fukushima[c,d], M. Fukutome[g,d], T. Haginouchi[f,d], S. Hayakawa[a], Y. Hijikata[e,d], J.W. Hwang[b], E. Ideguchi[h,d], S. Ishio[f,d], N. Iwasa[f,d], K. Kameya[f,d], K. Kawata[a], R. Kojima[a], K. Kusaka[d], J. Li[a], Y. Nakamura[c,d], H. Nishibata[i,d], D. Nishimura[c,a,d], K. Okawa[a], S. Ota[h,a], D. Suzuki[c], H. Suzuki[c], T. Saito[a], Y. Shimizu[d], S. Shimoura[a,d,h], T. Sumikama[d], H. Takahashi[c,d], H. Takeda[d], H. Tanaka[i,d], M. Tanaka[d], T. Teranishi[i,d], T. Tomiyama[c,d], T. Uesaka[d], R. Urayama[f,d], K. Yako[a], Y. Yanagisawa[d], K. Yoshida[d], and M. Yoshimoto[d]

[a] *Center for Nuclear Study, Graduate School of Science, The University of Tokyo*
[b] *Center for Exiotic Nuclear Studies, Institute for Basic Science*
[c] *Department of Natural Sciences, Tokyo City University*
[d] *RIKEN Nishina Center*
[e] *Department of Physics, Kyoto University*
[f] *Department of Physics, Tohoku University*
[g] *Department of Physics, Osaka University*
[h] *Research Center for Nuclear Physics, Osaka University*
[i] *Department of Physics, Kyushu University*

Some nuclei near the proton dripline are known to undergo decay through proton emission rather than β^+ or α decays. The phenomenon of two-proton radioactivity ($2p$ decay), where two protons are simultaneously emitted during nuclear decay, was theoretically predicted over 60 years ago [1] and was eventually discovered in proton-rich nuclei such as ^{45}Fe [2,3] and ^{48}Ni [2] in the early 2000s. Understanding the energy level structure and one- and two-proton separation energies is crucial to evaluating the two-proton emission probability while tunneling through the Coulomb and centrifugal potentials of those nuclei. The separation energies can be directly determined from the mass differences with one- and two-proton-deficient nuclei. Therefore, systematic mass measurements around the $2p$ radioactive nuclei significantly contribute to comprehending the emission mechanism of two protons from a nucleus.

We conducted direct mass measurements of proton-rich fp-shell isotopes near the proton dripline, including ^{45}Fe, using the TOF-$B\rho$ technique [4] at the OEDO-SHARAQ. The isotopes were produced by fragmenting the ^{78}Kr primary beam at 345 MeV/nucleon in a ^{9}Be target with a thickness of 2.2 g/cm^2. They were separated by the BigRIPS separator and transported to the OEDO beam line followed by the SHARAQ spectrometer. The detailed detector setup was reported in the previous report [5]. High-resolution tracking detectors [6] and precise timing detectors for TOF were installed in the achromatic and momentum-dispersive foci along the beamline. The measurements were performed using a combination of these state-of-the-art detectors and the high-resolution performance of the OEDO-SHARAQ dispersion-matching mode, which has a momentum resolution of $1/15000$ [7].

Figure 1 presents the preliminary mass spectrum obtained from the current measurements. The horizontal and vertical axes represent mass-to-charge ratio and yields, respectively. The obtained spectrum includes proton-rich Ti, Cr, Fe, and Ni isotopes in the vicinity of the proton dripline. The known masses of isotopes measured simultaneously, labeled by $A = 2Z - 1$, $2Z - 2$, $2Z - 3$, $2Z - 4$, were utilized for calibrations of the atomic masses.

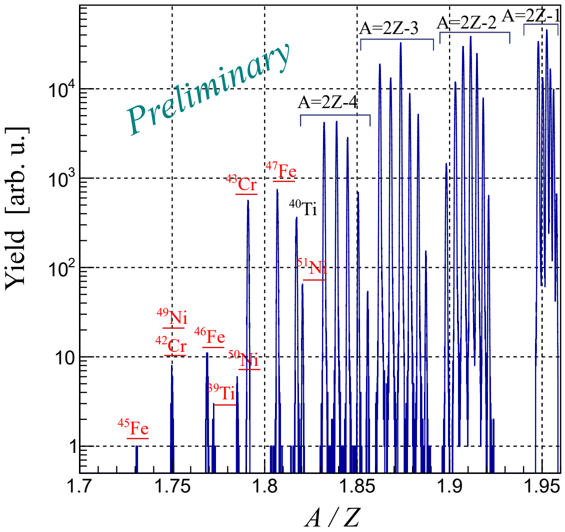

Figure 1: Mass spectrum of the current measurements. The nuclei with underscore represent unknown mass nuclei.

A detailed analysis is currently in progress, and the masses of underlined nuclei will be determined for the first time. The new insights into the proton dripline from Ca to Ni isotopes from this experiment will impact our understanding of nuclear structural evolution towards two-proton radioactivity.

References

[1] V. I. Goldanskii *et.al.*, Nucl. Phys. **19**, 484 (1960).
[2] C. Dossat *et.al.*, Phys. Rev. C. **72**, 054315 (2005).
[3] K. Miernik *et.al.*, Eur. Phys. J. A **42**, 431 (2009).
[4] S. Michimasa *et al.*, Phys. Rev. Lett. **121**, 022506 (2013).
[5] S. Hanai *et al.*, in this report.
[6] S. Hanai *et al.*, Prog. Theo. Exp. Phys. **2023**, 123H02 (2023).
[7] S. Hanai *et al.*, Accel. Prog. Rep **55**, 92 (2022).

Analysis status of the measurement of the double charge exchange (^{12}C, ^{12}Be(0_2^+)) reaction aiming for the observation of double Gamow–Teller giant resonance

A. Sakaue for the RIBF-141R1 collaboration

Center for Nuclear Study, Graduate School of Science, University of Tokyo

Double Gamow–Teller (DGT) transition is a nuclear process such that both of the spin and the isospin are flipped twice without change in the orbital angular momentum. The existence of the giant resonance in DGT transition (DGTGR) was predicted in 1989 [1], but it still remains unobserved experimentally. The experimental information of the DGTGR will provide insights about two-phonon excitations. Moreover, it is suggested that the observables of the DGTGR such as the strength or the centroid energy give a constraint to the nuclear matrix element of neutrino-less double β decay ($0\nu\beta\beta$) [2].

We are aiming at the observation of the DGTGR of the double charge exchange (DCX) reaction of (^{12}C, ^{12}Be(0_2^+)). The first measurement using this reaction at RIBF was performed in 2021 [3]. The DCX reaction was measured on a ^{48}Ca target with the primary beam with the energy of 250 MeV/nucleon. The ^{12}Be was momentum analyzed by BigRIPS spectrometer with a sufficient resolution of 1.6 MeV(FWHM). The isomeric state of ^{12}Be(0_2^+) was identified by measuring the de-excitation γ-ray by DALI2.

A preliminary result of excitation energy spectra for the ^{48}Ca(^{12}C,^{12}Be(0_2^+)) reaction is shown in Fig. 1. The contributions from accidental coincidence events with room-background γ-rays are evaluated from the inclusive spectra which is not gated by DALI2. Such events are subtracted in Fig. 1. Here we focus on the excitation energy region of $E_{\rm ex} < 34$ MeV. It is because there seems to be contamination of the ^{12}C(^{12}C, ^{12}Be(0_2^+))^{12}O events coming from the graphene sheet attached to the ^{48}Ca target for the region of $E_{\rm ex} > 34$ MeV. In addition, the expected DGT strength lies below 35 MeV for following reasons. As the central energy of the single GT resonance is $\sim$ 12 MeV from the ground state of ^{48}Ca with the width of 5 MeV [4], we expect that the DGTGR lies around $12\times2\sim$ 24 MeV, which corresponds to $E_{\rm ex}$ =20 MeV in ^{48}Ti, with the width of $5\times\sqrt{2}\sim$7 MeV. The shell model calculation also predicts that most of the DGT strength lies below 35 MeV [2]. In the preliminary spectrum, there is an enhancement around 20 MeV especially at the forward angle.

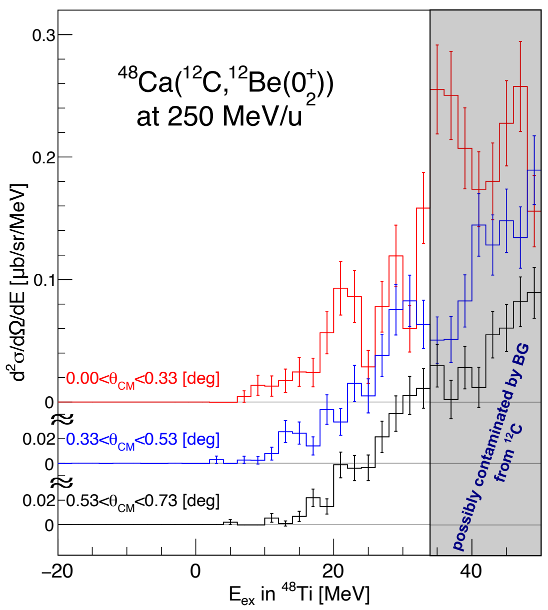

Figure 1: Excitation energy distribution of differential cross section of ^{48}Ca(^{12}C, ^{12}Be(0_2^+)) reaction at each angular region of 0-0.33, 0.33-0.53, and 0.53-0.73°.

To evaluate the DGT component contained in the observed structure, the angular distributions were compared with the calculated ones. The angular distribution of DCX reaction was estimated by performing coupled channel calculations using ECIS97 [5]. The reaction was divided into two steps of ^{48}Ca+^{12}C $\rightarrow$ ^{48}Sc+^{12}B and ^{48}Sc+^{12}B $\rightarrow$ ^{48}Ti+^{12}Be transitions. The angular distribution is characterized by the combination of the transfer of the orbital angular momentum ΔL in each step. The following three types of ΔL combinations are considered. The first type is $\Delta L=0$ in both of the transitions from the initial state to the intermediate state and from the intermediate state to the final state (we named it "$\Delta L_{\rm DCX}=0$"), which corresponds to the DGT transition. The other two types are $\Delta L=1$ or $\Delta L=2$ for the transition from the initial state to the intermediate state, and $\Delta L=0$ for from the intermediate state to the final state ("$\Delta L_{\rm DCX}=1$" or "$\Delta L_{\rm DCX}=2$").

The experimentally obtained angular distributions at each energy bin, $\sigma^{\rm exp}(\theta_{\rm cm},E_{\rm ex})$, were decomposed by the combination of $\Delta L_{\rm DCX}$ =0, 1, and 2. We performed the fit together with the background due to the accidental coincidence as

$$\begin{aligned}&\sigma^{\rm exp}(\theta_{\rm cm},E_{\rm ex})\\&=\sum_{\Delta L_{\rm DCX}=0,\,1,\,2}\left\{a_{\Delta L_{\rm DCX}}\cdot\sigma^{\rm calc}_{\Delta L_{\rm DCX}}(\theta_{\rm cm},E_{\rm ex})\right\}\\&\quad+\sigma_{\rm BG}(\theta_{\rm cm},E_{\rm ex}),\end{aligned}\qquad(1)$$

where $\sigma^{\rm calc}_{\Delta L_{\rm DCX}}(\theta_{\rm cm},E_{\rm ex})$ are the calculated angular distributions, $a_{\Delta L_{\rm DCX}}$ are the fitting coefficients for them. $\sigma_{\rm BG}(\theta_{\rm cm},E_{\rm ex})$ is the cross section of the accidental coincidence background evaluated from the inclusive spectra. We performed the decomposition by 4 MeV width of the excitation energy. The fitting coefficients are determined by the maximum likelihood method. The excitation energy distribution of the decomposed results are shown in Fig. 2 with the observed cross sections. The stacking histograms show the background (cyan), the $\Delta L_{\mathrm{DCX}} = 0$ (red), 1 (blue), and 2 (black) components, respectively. There is noticeable strength of $\Delta L_{\mathrm{DCX}} = 0$ around 20 MeV. The integrated cross section from 0 to 34 MeV for the $\Delta L_{\mathrm{DCX}} = 0$ component is $0.5^{+0.5}_{-0.1}$ μb/sr for the most forward angular region. Here the error only gives the statistical error.

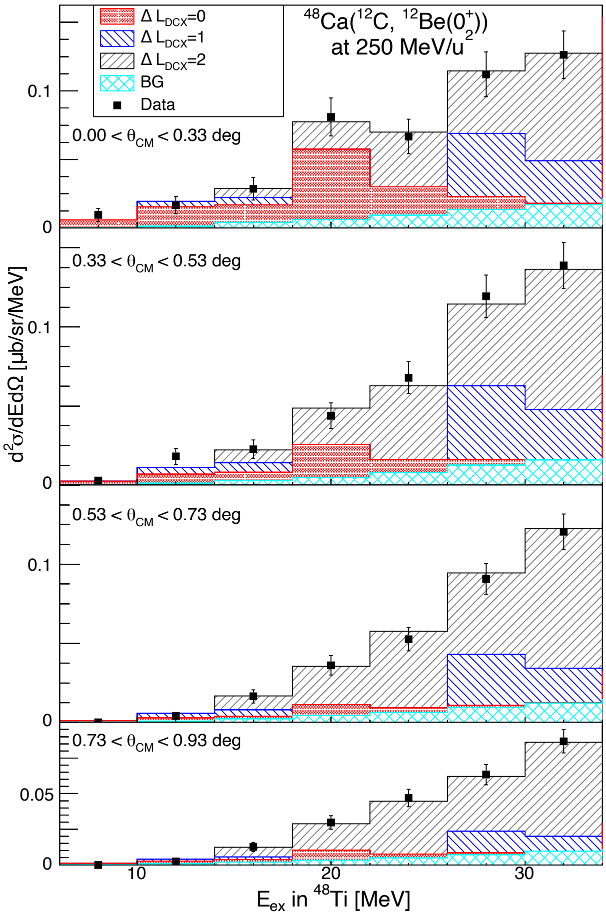

Figure 2: Measured cross section distribution by 4 MeV bin of excitation energy and the decomposed results.

The DGT transition strength B(DGT) is deduced from the extracted cross section of $\Delta L_{\mathrm{DCX}} = 0$ by comparing with the calculated cross section. Figure 3 shows the excitation energy distribution of B(DGT) deduced from the data (black points). The sum of the B(DGT) over 0 to 34 MeV is approximately 24. The central energy is 20 MeV and the width is 10 MeV. The evaluation of the uncertainties of these values is now in progress. Magenta curve shows the shell model calculation [2] scaled by 0.2. The trend of the energy distribution of the data is found to match to the shell model calculation.

We are now dedicated to the finalization of the results.

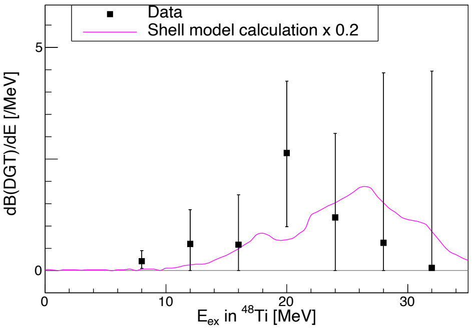

Figure 3: Extracted distribution of DGT strength B(DGT).

References

[1] N. Auerbach *et al.*, Ann. Phys. **192**, 77 (1989).
[2] N. Shimizu *et al.*, Phys. Rev. Lett. **120**, 142502 (2018).
[3] A. Sakaue *et al.*, RIKEN Accel. Prog. Rep. **56**, 6 (2023).
[4] K. Yako *et al.*, Phys. Rev. Lett. **103**, 012503 (2009).
[5] J. Raynal, Phys. Rev. C **23**, 2571 (1981).

β-delayed neutron emissions from $N > 50$ gallium isotopes

R. Yokoyama[a,b], R. Grzywacz[b,c], B. C. Rasco[c,b], N. T. Brewer[c,b], K. P. Rykaczewski[c],
I. Dillmann[d], J. L. Tain[e], and S. Nishimura[f] for the BRIKEN collaboration

[a] *Center for Nuclear Study, the University of Tokyo, 2-1 Hirosawa, Wako, Saitama 351-0198, Japan*
[b] *Department of Physics and Astronomy, University of Tennessee, Knoxville, TN 37996, USA*
[c] *Department of Physics, Oak Ridge National Laboratory, Oak Ridge, TN 37830, USA*
[d] *TRIUMF, Vancouver, British Columbia V6T 2A3, Canada*
[e] *Instituto de Fisica Corpuscular, CSIC-Universitat de Valencia, E-46071 Valencia, Spain*
[f] *RIKEN, Nishina Center, 2-1 Hirosawa, Wako, Saitama 351-0198, Japan*

β-delayed multi-neutron emission is expected to be the dominant decay mode for the nuclides far from stability, patticularly along the astrophysical *r*-process path. The number of neutrons emitted in decays of neutron-rich nuclei is an important input for the abundance calculations as it affects the final isobaric abundance pattern by providing neutrons for the late-time capture process and altering the decay path back to stability [1]. Until recently, the neutron emission probabilities (P_{xn}) for the *r*-process abundance calculations relied on predictions [2] based on the simplified assumption that only x-neutron emissions will occur when β-decay feeds a state above the x-neutron separation energy (S_{xn}), and the effect of less-than-x-neutron channels are negligible.

As we measured the β decays of $^{84-87}$Ga at RIBF using a high-efficiency array of ^{3}He neutron counters (BRIKEN), we have found large one-neutron emission probability (P_{1n}) values and unexpectedly small P_{2n} values, even for those Ga isotopes where the major part of the B(GT) is expected to be concentrated above S_{2n}. This was interpreted as a signature of one-neutron emission from two-neutron unbound states. By assuming sequential emissions of neutrons from a state above S_{2n} in the daughter nucleus, the final number of neutrons emitted in the the sequence depends on whether or not the first neutron took more energy than $S_{2n} - S_{1n}$. If the first emission populated a state below S_{1n}, two-neutron emission is no longer possible. This result underscores the importance of modeling the competition between multi-neutron emission channels as reported in a Rapid Communication paper [3]. The Hauser–Feshbach statistical model [4] was then applied to the global calculation by Möller *et al.* [5], which provided P_{xn} predictions based on more realistic model.

In this paper, we have performed an updated analysis of the decay of gallium isotopes. As we calculated the branching ratios using the statistical model, we found that the decay patterns were sensitive to the level densities of the daughter nuclei. In the statistical model code by Kawano *et al.* [4], shell and pairing energies from the mass formula by Koura *et al.*, KTUY05, were applied to the Gilbert–Cameron formula [6] to generate phenomenological nuclear level densities [7].

We performed shell-model calculations using the NuShellX code with the jj45pna interaction to estimate level densities of the Ge isotopes. Owing to our computational limit, levels up to ≈7 MeV were calculated for all the spins and parities. The shell-model level densities were fitted by the constant temperature level density formula,

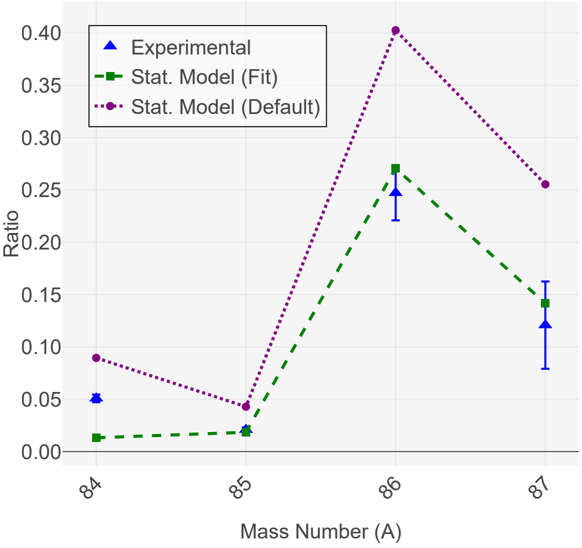

Figure 1: P_{2n}/P_{1n} ratio in the decay of Ga isotopes. The red circle shows the experimental value, while the dashed and solid lines show the statistical model predictions obtained by using default and shell-model-based parameters for the level densities, respectively.

$$\rho = \frac{1}{T} \exp\left(\frac{E - E_0}{T}\right) \tag{1}$$

where the shell correction (δw), pairing correction (Δ), and scaling factor (f_{tweak}) in E_0 were free parameters. The shell-model level densities were consistently lower than the default ones in the statistical model code. (See original paper [8] for details.)

Figure 1 shows the P_{2n}/P_{1n} ratios in the decays of $^{84-87}$Ga and the statistical model calculations obtained by using different level densities. The default level densities consistently predicted larger P_{2n} ratios for all four Ga isotopes. This is because a higher level density above S_{1n} in the 1n daughter nucleus can result in a higher probability of emitting a second neutron. The experimental ratios agree better when shell-model level densities are used, which could mean the level densities of those Ge isotopes were lower than when default parameters were used. This result reveales the need for a detailed understanding of the level densities and decay scheme, which could be studied by neutron spectroscopy.

References

[1] R. Surman, M. Mumpower, and A. Aprahamian, JPS Conf. Proc. **6**, 010010 (2015)

[2] P. Möller *et al*., Phys. Rev. C **67**, 055802 (2003)

[3] R. Yokoyama *et al*., Phys. Rev. C **100**, 031302 (2019)

[4] T. Kawano *et al.*, Phys. Rev. C **78**, 054601 (2008)

[5] P. Möller *et al*., Phys. Rev. C **100**, 031302 (2019)

[6] A. Gilbert *et al*., Can. J. Phys. **43**, 1446 (1965)

[7] T. Kawano *et al*., J. Nucl. Sci. Technol. **43**, 1 (2006)

[8] R. Yokoyama *et al*., Phys. Rev. C **108**, 064307 (2023)

Re-measurement of heavy-ion fusion cross section of ^{136}Xe+^{64}Zn system using inverse kinematics

J. T. Li, N. Imai, R. Yokoyama, T. Chillery, S. Michimasa, R. Kojima, N. Kitamura, D. Nishimura[a],
J. Sonoda[a], R. Kageyama[a], C. Fukushima[a], Y. Nakamura[a], M. Amitani[a], D. Suzuki[b], E. Takada[c]
Center for Nuclear Study, Graduate School of Science, University of Tokyo
[a]*Tokyo City University*
[b]*RIKEN Nishina Center*
[c]*QST-HIMAC*

Heavy-ion fusion reactions are powerful in expanding the chart of nuclides as well as exploring the nuclear structure, especially for high excited states. The dynamical evolution of the di-nuclear system is rather complicated, as indicated in Fig. 1. To form the evaporation residues (ERs), two colliding nuclei need to overcome the potential barrier to form a compound state, and then the compound nuclei (CN) need to survive against the fission. For heavy systems, another barrier above the potential barrier occurs due to the increasing surface energy, thus extra energies are required to form CN. The pre-equilibrium fission-like process is referred to as quasi-fission (QF). QF prevents the formation of CN and thus hinders the fusion-evaporation cross section significantly. QF may be induced by various degrees of freedoms of the entrance channel [1], including charge product, mass asymmetry, static deformation, etc. The dynamics of QF has not been established due to the lack of experimental data.

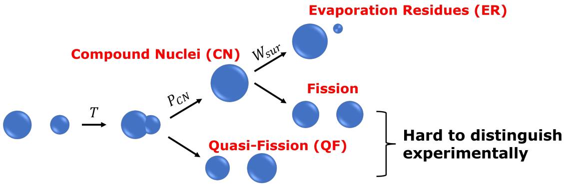

Figure 1: Schematics of the heavy-ion collision.

To understand QF quantitatively, a project to study heavy-ion fusion reactions of near-symmetric system is now ongoing at CNS. As the first step, the measurement of ^{136}Xe + ^{nat}Zn was performed as the commissioning experiment in 2022 at HIMAC [2], but there was a difficulty in identifying α decays of ERs due to the geometry of the detectors. In 2023, the same system was studied again with a modified geometry. The schematics of the updated setup is shown in Fig. 2. ^{136}Xe beam with the energy of 6 MeV/u was delivered by the LINAC, to obtain the desired beam energy, angle-tunable Al degraders were used [2]. The beam energy was then determined by the time-of-flight measured using a microchannel plate and a plastic scintillator. The natural zinc target with a thickness of 1 µm was backed with an 18-µm-thick graphene sheet. The thickness was chosen so that after the fusion reaction, beam would pass through while the ERs would stop and α-decay in the graphene sheet. The target and the backing material were tilted by 45° with respect to the beam axis. Two mosaic-type Si array [3,4] along with a Pad type Si PIN photodiode were placed around the target to measure the decayed α particles from ERs. The arrays were aligned parallel with the target to minimize the energy loss of α particles inside the target and the backing material. In addition, activation measurements were performed after the beam time of each day. The setup is shown in Fig. 3. A HPGe detector was used for the activation measurement, and it was surrounded by lead bricks. The count rate of the natural background was reduced from 30 to 4 cps after shielding.

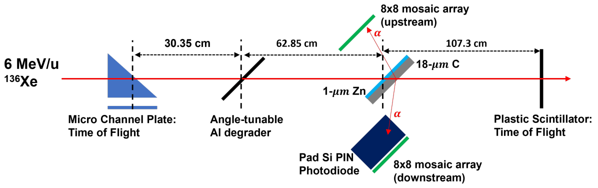

Figure 2: Schematics of the experimental setup.

Figure 3: Setup of the activation measurement.

To measure the α decay of ERs, beam pulsing modes with 6 spills on and off (1.65 s / spill) were applied in the experiment. Figure 4 presents the α-energy spectrum measured by the upstream array during the beam-off period at E_{Lab} = 650 MeV. The x-axis is the scattering angle of the detected α particles with respect to the beam direction. The angular dependence of α energies is evident, resulting from the different emission angles of α particles, which leads to the variation in the travelling distance inside the target and the backing material.

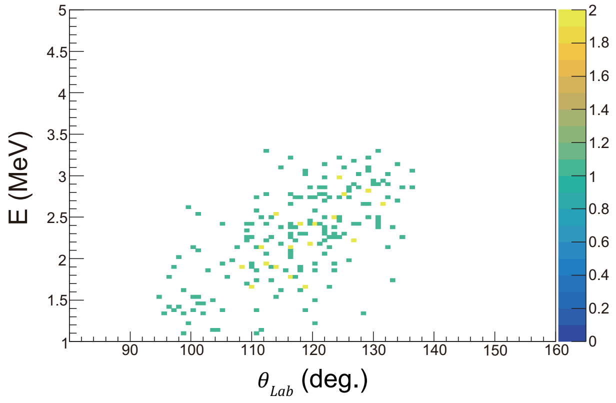

Figure 4: Angular dependence of α particles measured by the upstream array during the beam-off period at $E_{Lab} = 650$ MeV.

Figure 5 illustrates the extracted excitation functions of neutron-evaporation channel in ^{136}Xe + ^{64}Zn system, the y-axis is the reduced cross sections. The black squares are the data measured in this experiment, the horizontal error bar represents the energy loss of the beam in the target. It can be seen that the extracted excitation function aligned with the previous data that measured the system producing the same CN (purple, blue dots) [5, 6], and was reproduced well by the calculation using statistical model HIVAP [7].

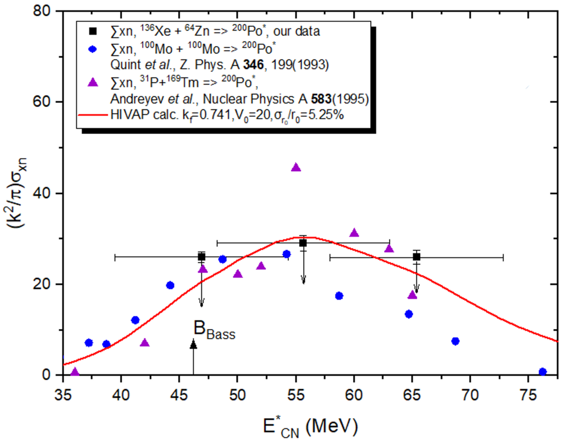

Figure 5: Excitation function of neutron-evaporation channel in ^{136}Xe + ^{64}Zn system.

In the activation measurement, β-delayed γ rays emitted from ^{155,157}Dy and $^{155-159}$Ho, produced from the fusion reaction between the beam and the Al degrader, have been identified. The search for γ rays produced by the fusion reaction between the beam and the zinc target is ongoing.

In summary, a fusion experiment using low energy ^{136}Xe beam and the zinc target was performed again. Evident kinematic curves of α particles were observed. The extracted excitation functions agreed well with HIVAP calculations and previous experimental results. Analysis of the α-decay spectroscopy at other beam energies as well as the off-line γ spectroscopy are now in progress.

References

[1] A. C. Berriman *et al.,* Nature **413**, 144 (2001).
[2] J. T. Li *et al.,* CNS Annual Report 2022, 17 (2024).
[3] J. T. Li *et al.,* CNS Annual Report 2021, 39 (2023).
[4] J. T. Li *et al.,* CNS Annual Report 2022, 37 (2024).
[5] A. B. Quint *et al.,* Z. Phys. A **346**, 199 (1993).
[6] A. N. Andreyev *et al.,* Nucl. Phys. A **583** (1995).
[7] W. Reisdorf, Z. Phys. A **300**, 227 (1981).

^{10}C $+\alpha$ elastic scattering: a study of the proton rich ^{14}O nucleus and α-clustering

N. R. Ma[a,b], M. Sferrazza[c], H. Yamaguchi[a], P. Descouvemont[d], S. Okamoto[f], S. Hayakawa[a], and H. Shimizu[a]

[a]Center for Nuclear Study, Graduate School of Science, University of Tokyo
[b]Department of Nuclear Physics, China Institute of Atomic Energy
[c]Département de Physique, Université Libre de Bruxelles (ULB), 1050 Brussels, Belgium
[e]Physique Nucléaire Théorique et Physique Mathématique, Université Libre de Bruxelles (ULB), 1050 Brussels, Belgium
[f]Department of Physics, Kyoto University, Kita-Shirakawa-Oiwake, Sakyo, Kyoto 606-8502, Japan

The measurement of ^{10}C $+\alpha$ elastic scattering was performed at CRIB with two main goals: to investigate the structure of the ^{14}O nucleus (in the energy range of 13–18 MeV) and to explore the possibility of resonances with α cluster structures, as observed in the mirror nucleus ^{14}C [1]. The ^{10}C $+\alpha$ elastic scattering was studied using the thick-target inverse kinematics method and a low-energy ^{10}C radioactive beam. The detail experimental setup and primary data analysis work had been described in the previous annual report [2].

Primary data analysis provides the ^{10}C $+\alpha$ elastic scattering yield, combined with the number of incident ^{10}C particles, the effective target thickness and the solid angle of the detector obtained from Geant4 simulation, the differential cross section $(d\sigma/d\Omega)_{\rm cm}$ (DCS) was calculated. The ^{10}C $+\alpha$ elastic scattering excitation function over a wide angular range of $\theta_{\rm c.m.} = 110 \sim 180^\circ$ and a wide energy range of $E_{\rm ex}$= 12.5 $\sim$ 20.0 MeV were obtained, as shown in Fig. 1. The peak structure at several fixed energies are visible, which validates the correctness of the kinematics calculation. In particular, resonant scattering peaks near $E_{\rm c.m.}$ = 3.3, 4.2, 5.4, 6.3 and 7.9 MeV ($E_{\rm ex}$= 13.4, 14.3, 15.4, 16.4 and 18.0 MeV) are observed. The angular dependence of the DCS may reflect the spin value for the resonances: the peaks near $E_{\rm c.m.}$ = 3.3 and 5.4 MeV ($E_{\rm ex}$= 13.4 and 15.4 MeV) are retained to the lower $\theta_{\rm c.m.}$ suggesting that they are from low-spin resonances. On the other hand, the peaks near $E_{\rm c.m.}$ = 4.2, 6.3, and 7.9 MeV ($E_{\rm ex}$= 14.3, 16.4 and 18.0 MeV) attenuate rapidly with decreasing of $\theta_{\rm c.m.}$ suggesting that the spins of the resonances around these energies are higher ($J > 3$).

We have performed an R-matrix analysis [3] for the experimental data with the AZURE2 code [4] in order to determine the resonance parameters: energy $E_{\rm ex}$ spin J, parity π and width Γ_α. The error analysis of all parameters was also completed by MINOS Error Analysis function of AZURE2. A typical channel radius of 5.0 fm was used, and small variations around this value provide similar results. The calculated spectrum was broadened with the experimental resolution stated above.

We started the analysis by considering the previous information available in literature in the energy region of our experiment. Only a few resonances are known in the energy region $E_{\rm ex}$=13–18 MeV; for two resonances, spins and parities have been proposed (see the discussion below). Previous work reported the resonances at 12.84, 13.01 14.15, 14.64 and 17.4 MeV using the ^{14}N(^{3}He, t)^{14}O reaction with no spins assigned [5]. With two-proton stripping reaction ^{12}C(^{12}C,^{10}Be)^{14}O, four resonances were reported in ^{14}O: 6.27, 9.9, 14.1 and 15.7 MeV, with tentative spin assignments of (4^+) and (5^-) for the resonances at 14.1 and 15.7 MeV respectively. The authors indicate the uncertainty of these spin assignments since the shape of the angular distributions of the cross-section for these levels do not show an expected spin dependence [6]. The differential cross section for ^{14}O was also measured in the reaction ^{13}C(p, π^-)^{14}O using a proton beam at 100 MeV, and one strong level has been observed at 14.15 MeV for which a possible spin of (5^-) was suggested [7] [8]. Other levels were also reported at 14.6 and 17.4 MeV [7] [8].

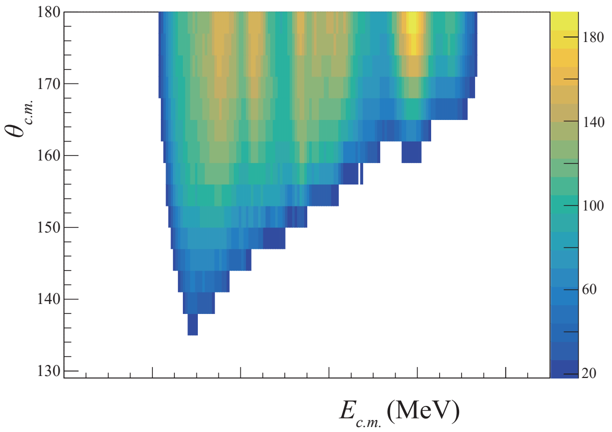

Figure 1: Energy ($E_{\rm c.m.}$) vs the angular ($\theta_{\rm c.m.}$) distribution of the ^{10}C+α scattering measured by the telescope #1.

The present experiment, however, indicates the presence of more resonances than the ones reported in literature in this energy range. In order to constrain the parameters, we have fitted the three angular ranges simultaneously. The best fit is shown for the three segments in Fig. 2 and the resonance parameters are reported in Table. 1.

The results reported in Table. 1 indicate that two levels, the 0^+ and the 2^+ at 13.43 and 14.88 MeV respectively, with relatively large reduced widths θ^2_α (36.4% and 23%). As mentioned in the introduction, α cluster states have a significant fraction of the Wigner limit ($\theta^2_\alpha \approx 10-50\%$), in contrast to compact states that present smaller θ^2_α values.

The excitation energies of the π-bond linear-chain states

Table 1: Resonance parameters in ^{14}O determined in the present work - $E_{\rm c.m.}$, $E_{\rm ex}$, J^π, Γ_α.

Experimental results					Literature	
$E_{\rm c.m.}$ MeV	$E_{\rm ex}$ MeV	J^π	Γ_α keV	θ^2_α	$E_{\rm ex}$ MeV	J^π
2.82	12.94	1^-	252 (44)	39.3%	12.84 (5)[a]	
3.32	13.43	0^+	511 (143)	36.4%	13.01 (5)[a]	
4.18	14.29	4^+	6 (2)	3.6%	14.1[b] / 14.15 (4)[c]	(4^+)[b] / (5^-)[c]
4.77	14.88	2^+	385 (296)	23.0%	14.64 (6)[a]	
5.21	15.33	(0^+)	295 (191)	9.7%		
5.56	15.68	(1^-)	8 (7)	0.3%	15.7[d]	(5^-)[d]
6.06	16.17	(3^-)	13 (6)	0.7%		
6.26	16.38	(4^+)	7 (2)	0.7%		
7.41	17.52	1^-	61 (33)	1.5%	17.40 (6)[a]	
7.56	17.68	(5^-)	1 (5)[e]	0.1%		
7.93	18.05	4^+	11 (3)	0.6%		

[a] See [5]

[b] Kraus et al. propose a resonance at 14.1 MeV with a possible spin (4^+) [6].

[c] Korkmaz et al. propose a spin (5^-) for a resonance at 14.15 MeV [8].

[f] A level at 15.7 MeV is reported with a tentative spin of (5^-) by Kraush et al [6].

[e] The error on Γ_α for this resonance is very large in comparison also to the value: this suggests the important incertitude on this level and the strong correlation with the doublet. However, this resonance is needed to reproduce the data.

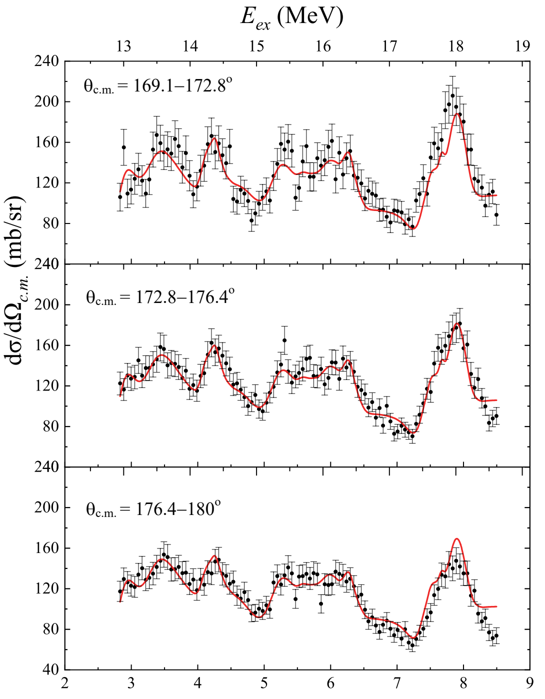

Figure 2: Experimental center-of-mass cross section of the ^{10}C+α scattering $(d\sigma/d\Omega)_{\rm c.m.}$ as a function of $E_{\rm c.m.}$ in the bottom axis and as a function of the excitation energy $E_{\rm ex}$ in the top axis. The DSC data are fitted with the R-matrix calculation using AZURE2 (lines are the fits, $\chi^2/ndof = 337/291$). From top to bottom $\theta_{\rm c.m.}$ = 169.1°–172.8°, 172.8°-176.4° and 176.4°–180° respectively.

in ^{14}O are plotted against $J(J+1)$ in Fig. 3, together with the experimental candidates of the linear-chain cluster states in the present work (the 0^+ and the 2^+), as well as the cluster band proposed in [1] for ^{14}C. According to [9], the first two π-bond states in ^{14}O emerge at 14.37 MeV (0^+) and 15.98 MeV (2^+), which may correspond with the two cluster states observed in the present work at 13.42 MeV (0^+) and 14.88 MeV (2^+), with, however, energy offsets of about 1 MeV.

In the present R-matrix analysis of ^{14}O, we identified in a 4^+ resonance at 18.05 MeV forming a doublet with 5^-, similarly to the previous results of ^{14}C but with around four times smaller θ^2_α of 0.6%, indicating the non α-cluster nature for this state (the θ^2_α for the 4^+ in ^{14}C is 2.4(9)% [1]). A notable feature of the theoretical calculation in [9] is that the π-bond state in ^{14}O with J^π=4^+ is fragmented into two states at 17.36 and 18.13 MeV as shown in Fig. 3, while the 4^+ state in ^{14}C stays as a single state. This suggests a possibility that the predicted cluster states could be observed as fragments having smaller widths. While the predicted 4^+ level at 18.13 MeV has similar energy of the observed 18.05 MeV resonance, another observed (4^+) level at 16.38 MeV of excitation energy with θ^2_α of 0.7% could be a possible candidate for the other predicted fragmented 4^+, although with an energy difference between the two 4^+ of 1.67 MeV, larger than the predicted 0.77 MeV. The possible fragmented 4^+ resonance may qualitatively explain the smaller Γ_α in ^{14}O; however, we can not exclude a possibility that the 4^+ could be another resonance of different structure than of the 4^+ in the mirror nucleus ^{14}C. On the other hand, the theory [9] appears to disagree with the experiments on several points: 1) the theory predicts small energy shifts be-

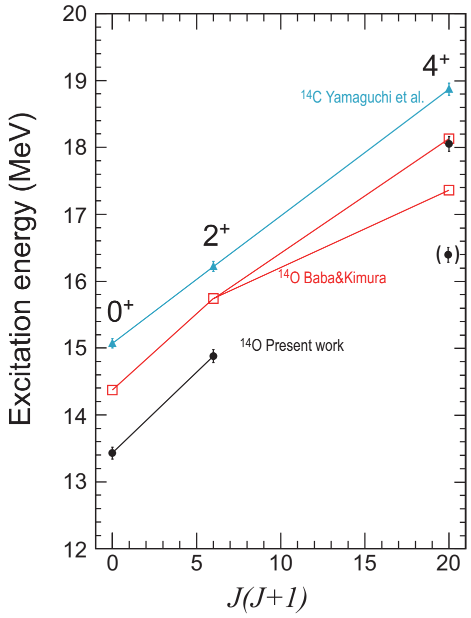

Figure 3: Excitation energies of the resonances in ^{14}O plotted against $J(J+1)$ for the predicted linear chain band [9] (open square) and by the present work (solid circles). The candidate of the linear-chain band in ^{14}C proposed in [1] is also plotted for comparison (solid triangle). The lower 4^+ state in the present work is with a tentative J^π assignment and plotted with parentheses.

tween ^{14}O and ^{14}C for the π-bond states, but the experimental candidates for them have energy shifts of 0.8-1.6 MeV, comparable to the difference in their α-threshold energies, and 2) the calculated Γ_α seem to be systematically larger than the experimental observed resonances. These observation may suggest a different clustering picture of ^{14}O compared to ^{14}C and necessities of further theoretical and experimental works for a more comprehensive understanding.

In summary, we studied the structure of the proton-rich nucleus ^{14}O with the resonant elastic scattering $^{10}\mathrm{C}+\alpha$ reaction. A complex structure was observed with many new resonances observed in the energy range of 13–18 MeV. The R-matrix fit allows to determine the properties of the resonances (energy, spin, parity and width). The results were compared with published data, and some spin assignment are proposed (for example we assign 4^+ for the 14.2 MeV level). Possible α-cluster-like states are proposed for the 0^+ and 2^+ at 13.44 and 14.88 MeV, respectively, similarly to what was found in the mirror symmetric ^{14}C nucleus. A further experimental work is needed for a better understanding of the structure of this nucleus.

References

[1] H. Yamaguchi, D. Kahl, S. Hayakawa, *et al.*, Phys. Lett. B **766**, 11 (2017).

[2] N.R. Ma, M. Sferrazza, H. Yamaguchi, *et al.*, CNS Annual Report **766** (2020).

[3] P. Descouvemont, D. Baye, Rep. Prog. Phys. **73**, 036301 (2010).

[4] R.E. Azuma, E. Uberseder, E.C. Simpson, *et al.*, Phys. Rev. C **81**, 045805 (2010).

[5] F. Ajznberg-Selove, Nucl. Phys. A **523**, 1 (1991).

[6] L. Kraus, A. Boucenna, I. Linck, *et al.*, Phys. Rev. C **37**, 2359 (1988).

[7] E. Korkmaz, L.C. Bland, W.W. Jacob, *et al.*, Phys. Rev. Lett. **58**, 104 (1987).

[8] E. Korkmaz, L.C. Bland, W.W. Jacob, *et al.*, Phys.Rev. C **40**, 813 (1989).

[9] T. Baba, M. Kimura, Phys. Rev. C **99**, 021303 (2019).

Data analysis of the ^{26}Si(α, p)^{29}P reaction for the nucleosynthesis in the X-ray bursts

K. Okawa[a], M. J. Kim[b], K. Y. Chae[b], S. Hayakawa[a], S. Adachi[c], S. M. Cha[d], T. Chillery[a], N. N. Duy[b], T. Furuno[c], G. M. Gu[b], S. Hanai[a], N. Imai[a], D. Kahl[e], T. Kawabata[c], C. H. Kim[b], D. Kim[d], S. H. Kim[b], S. Kubono[f], M. S. Kwag[b], J. Li[a], N. R. Ma[a], S. Michimasa[a], K. Sakanashi[c], H. Shimizu[a], O. Sirbu[e], N. K. Uyen[b], H. Yamaguchi[a], R. Yokoyama[a], and Q. Zhang[a]

[a] *Center for Nuclear Study, Graduate School of Science, University of Tokyo*
[b] *Department of Physics, Sungkyunkwan University*
[c] *Department of Physics, Osaka University*
[d] *Center of Exotic Nuclear Studies, Institute for Basic Science (IBS)*
[e] *Extreme Light Infrastructure Nuclear Physics (ELI-NP)*
[f] *RIKEN Nishina Center*

1. Introduction

Type I X-ray bursts (XRBs) are thermonuclear explosions occurring in a binary system consisting of an accreting neutron star and a main-sequence companion star. Some of the important observables of these phenomena are the light curve and recurrence time, which are the time variation of the X-ray flux and intervals of repeating bursts, respectively. The properties of the X-ray binary system can be understood by comparing these observations of XRBs with astrophysical models. XRBs are mainly powered by the triple-α reaction, αp-process and rp-process, and these models require accurate nuclear physics data to perform realistic simulations. Cyburt et al. [1] investigated how sensitive nuclear reactions are to the XRB light curve, and their research indicated that the ^{26}Si(α, p)^{29}P reaction significantly influences the light curve. To experimentally determine the reaction rate, Almaraz-Calderon *et al.* [2] studied the energy level structure of ^{30}S through ^{28}Si(^{3}He, n)^{30}S and ^{32}S(p, t)^{30}S transfer reactions. However, their measurements were limited to energy levels up to 12.04 MeV, and allowed only random spin assignments, lacking sufficient data above the α-threshold (9.343 MeV), which is a critical region to estimate the ^{26}Si(α,p)^{29}P reaction rate. To obtain adequate data, we performed a direct measurement of the ^{26}Si(α, p)^{29}P reaction, and obtained the cross section from the direct measurement for the first time.

2. Experimental setup

The measurement was performed at the Center for Nuclear Study Radioisotope Beam Separator (CRIB) [3]. The primary ^{24}Mg^{8+} beam bombarded on the ^{3}He gas target and the secondary ^{26}Si^{14+} beam was produced by the ^{3}He(^{24}Mg, ^{26}Si)n reaction. The averaged intensity of the ^{26}Si^{14+} beam was 2.8×10^4 pps, and its purity was 18.4%. In the target chamber filled with ^{4}He gas at 250 Torr, five position-sensitive ΔE-E telescopes were installed as shown in Figure 1. Beam tracking information was obtained by two delay-line Parallel Plate Avalanche Counters (dl-PPACs) [4]. Mylar foil ($C_{10}H_8O_4$) was used for the windows to seal the ^{4}He gas. The thick target method in inverse kinematics [5] was used to investigate a wide range of the reaction energy. With this experimental setup, the ^{26}Si(α, p)^{29}P reaction was measured up to a center-of-mass energy of about 7.5 MeV ($T \sim 9$ GK). We also performed $^{\mathrm{nat}}$Ar gas target measurement at 53.5 Torr to observe the background events, in which the detected protons are produced by other material than the ^{4}He gas target.

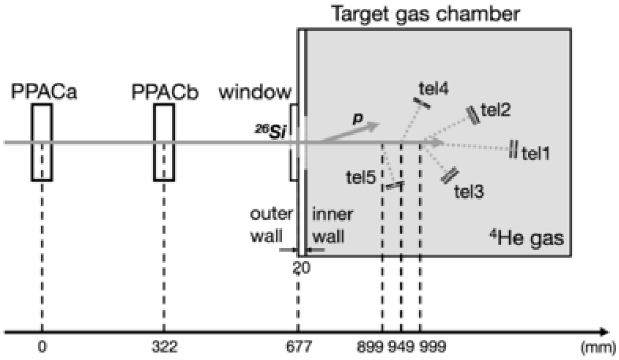

Figure 1: Experimental setup of the target chamber.

3. Analysis

We reported the first experimental cross section in Ref [6], but it had several limitations: the method of estimating background events, the disregard of transitions to excited states of ^{29}P, and the rough estimation of systematic errors. Previously, we assumed that all reactions were transitions to the ground state. To estimate the effect of transitions to the excited states, we performed calculations using the TALYS code [7]. As shown in Figure 2, we found that even the effect of the transition to the 10th excited state ($E_x = 4.95$ MeV) could not be ignored in the high energy region. If the reaction to the xth excited state occurs, we cannot assume that the proton events detected at low energy are of background origin; it is possible that they originate from (α, p_x) reactions. Therefore, the background subtraction was done based on the number of incident ^{26}Si beams, although previously it was based on the number of low energy proton events.

Next, to investigate the effect of transitions to excited states, we compared the results using the kinematics assuming all events are transitions to the ground state with those using the kinematics assuming all events are transitions to the first excited state. As shown in Figure 2, the result changed by about 50% depending on the kinematics. Although we only considered the effect of the first excited states here, the effect on the results is significant, indicating the necessity to include the effects of higher excited states, as long as the reaction cross sections are non-negligible. However, as shown in Figure 3, it was not possible to estimate which reaction was responsible for each event, due to the limitations of the timing resolution.

Simulations were performed to estimate systematic errors, taking into account the energy spread of the beam, the error in the detection position, and the energy resolution of the detector, to obtain a more accurate estimate of systematic errors. The horizontal error bars in Figure 2 are the systematic errors obtained in the simulation, while the vertical error bars represent the statistical error with the background subtracted.

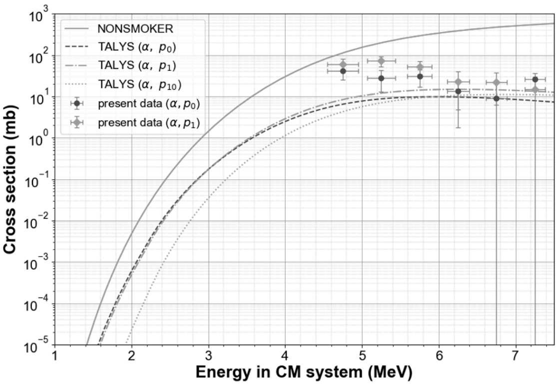

Figure 2: Present cross section and statistical model calculation. The solid line represents the NON-SMOKER cross section [8] used in the X-ray burst model calculation. The dashed lines represent the TALYS calculation [7] of the (α, p_0), (α, p_1) and (α, p_{10}) reactions, as examples. The data points denoted as (α, p_0) / (α, p_1) are obtained by analysis assuming the kinematics where the final state of ^{29}P is always in the ground state / the first excited state, respectively.

4. Summary and outlook

We analyzed the data taking into account transitions to excited states of ^{29}P to obtain more accurate reaction cross-sections and obtained new results. Due to the limitations of the timing resolution, it was not possible to identify the final state of ^{29}P event-by-event. On the other hand, statistical model calculations indicate that transitions to higher excited states should also be considered. One possibile solution is to assign a random excited state to each (α, p) event with a probability based on the statistical model calculation. The current analysis, assuming all the reaction are (α, p_0) or (α, p_1) showed that the data obtained are about an order of magnitude smaller than the NON-SMOKER model values [8], suggesting a significant impact on the X-ray burst model. For a more accurate evaluation, it is necessary to properly treat the events transitioning to higher excited states, and we believe that a comparison with the ongoing analysis of the ^{26}Si$(\alpha,\alpha)^{26}$Si resonance scattering [9] will provide more complementary results.

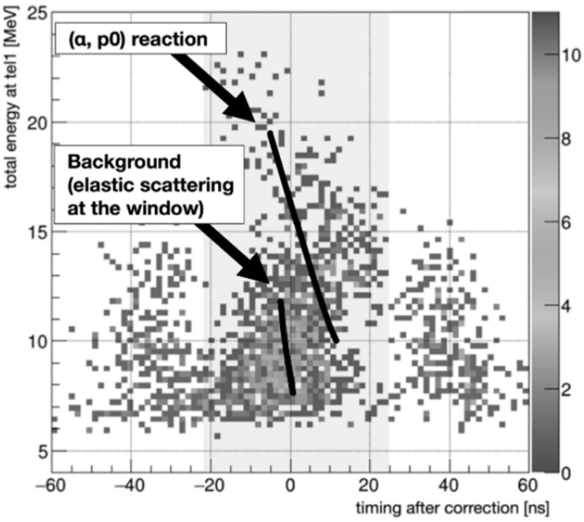

Figure 3: Energy vs. Timing plot of proton events at telescope 1. Only events within the grayed region were selected, as events outside this region are considered beam-like background events. The solid lines are the relationship expected for the (α, p_0) reaction and elastic scattering at target chamber.

References

[1] R. H. Cyburt *et al.*, Astrophys. J. **830**, 55 (2016).
[2] S. Almaraz-Calderon *et al.*, Phys. Rev. C **86**, 065805 (2012).
[3] Y. Yanagisawa *et al.*, Nucl. Inst. and Meth. A, **539**, 74 (2005).
[4] H. Kumagai *et al.*, Nucl. Inst. and Meth. A **470**, 562 (2001).
[5] K. Artemov *et al.*, Sov. J. Nucl. Phys. **52**, 408 (1990).
[6] K. Okawa *et al.*, CNS Annual Report, (2022).
[7] T. Koning *et al.*, Eur. Phys. J. A, **59**, 131 (2023).
[8] T. Rauscher, NON-SMOKER database, `https://nucastro.org/nonsmoker.html`.
[9] M. J. Kim *et al.*, CNS Annual Report, (2021).

A study of ^{6}He+p reaction: elastic scattering and neutron transfer reactions

Q. Zhang[a,b], M. Sferrazza[c], H. Yamaguchi[a], S. Hayakawa[a], K. Okawa[a], P. Descouvemont[c], D. S. Ahn[d], S. H. Ahn[d], K. Chae[e], S. Cherubini[f], T. Chillery[a], A. Di Pietro[f], S. Etelaeniemi[g], G. Gu[e], S. Hanai[a], Y. Honda[g], J. Hu[i], J. Hwang[d], N. Imai[a], T. Kawabata[g], C. Kim[e], M. J. Kim[d], S. Kim[e], N. Kitamura[a], M. La Cognata[f], J. T. Li[a], Y. Y. Li[i], Y. F. Lin[g], F. L. Liu[a,j], S. Masuoka[a], V. Phong[k], G. Pizzone[f], K. Sakanashi[g], S. Soki[g], C. Soomi[d], G. Takayama[g], M. Tanaka[l], F. Tatsuya[g], N. Tian[i], J. H. Won[d], K. Yako[a]

[a] *Center for Nuclear Study, the University of Tokyo*
[b] *School of Nuclear Science and Technology, Lanzhou University*
[c] *Department of Physics, Université Libre de Bruxelles*
[d] *Center for Exotic Nuclear Studies, Institute for Basic Science*
[e] *Department of Physics, Sungkyunkwan University*
[f] *INFN - Laboratori Nazionali del Sud*
[g] *Department of Physics, Osaka University*
[i] *Institute of Modern Physics, Chinese Academy of Sciences*
[j] *Department of Nuclear Physics, China institute of atomic energy*
[k] *RIKEN*
[l] *Division for Experimental Natural Science, Kyushu University*

The nuclear reaction ^{6}He+p was studied at a beam energy 8 MeV/u. ^{6}He is the lightest halo nucleus and is well described by a three-body model (α+n+n), two-neutron system around an alpha particle [1]. The nucleus is bound by $\sim$1 MeV against the α+n+n breakup. By investigating nuclear reactions with halo nuclei, information on the nucleons transfer process and on the halo structure itself can be obtained [2–4].

The experiment was performed in May 2023 and February 2024 at the CNS Radio-isotope Beam Separator (CRIB). A ^{7}Li^{3+} beam at energy 8.3 MeV/u with the intensity of 4.4 eμA was extracted from the AVF cyclotron to bombard the cryogenic gas cell, filled with deuterium gas. The ^{6}He ions were produced via the ^{7}Li(d, ^{3}He)^{6}He reaction in inverse kinematics. The ^{6}He beam energy at the F3 chamber was 7.86 MeV/u, and the intensity reached to 6×10^5 cps with a purity higher than 87% under the optimal experimental conditions. Two multi-wire drift chambers (MWDC) [5] were used to monitor the beam intensity [6] and track the beam particles event by event. Figure 1 shows a schematic of the setup used: the MWDCa (upstream), the MWDCb (downstream), and the six telescopes, as well as the relevant distances. The tracking efficiencies of MWDCa and MWDCb were better than 90% and 95%, respectively, when their supplied voltages were -895 V and -796 V, respectively. The CH$_2$ target (50 um) and carbon target (25 um) were used to study the nuclear reactions mentioned above and background events, respectively. Six silicon telescopes were used in the F3 chamber to measure the elastic and transfer reactions. The active size of each layer was 50 × 50 mm^2 and the distance between each layer of the six telescopes was less than 10 mm. For each telescope, a double-sided silicon detector (16 × 16 strips, 42–301 um) was used as the first layer to measure the hit position and the energy loss (ΔE) of the products. The remaining silicon detectors of each telescope measured the residual energies of the particles. The angular resolution for each telescope was $\sim$1 degree in the laboratory system. Proton (p), deuteron (d), triton (t), alpha (α), and ^{6}He were identified by the ΔE-E method, as shown in Figure 2.

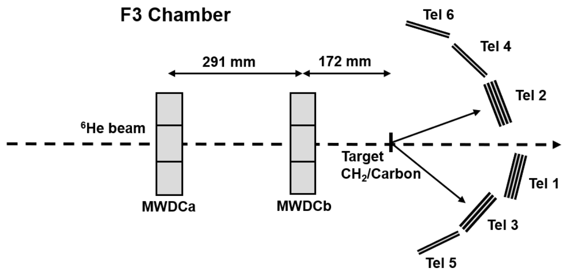

Figure 1: Schematic of the detector setup in the F3 chamber. Six silicon telescope were located at different angles. The figure shows also the MWDC and the distances.

The analysis is in progress. Figure 3 shows the preliminary results of the kinematical loci of protons (proton energy versus angle in the laboratory frame). The locus of the elastic proton (p_0) scattering from ^{6}He is clearly visible (solid curve). We also observe the inelastic protons (p_1) scattering from the ^{6}He(p, p_1)^{6}He, where ^{6}He is at the first excited state ($J^\pi = 2^+$, $E_x = 1.8$ MeV), as indicated by the dashed curve. The differential cross section of the elastic scattering and neutron transfer reactions will be deduced by considering the geometry of the six telescopes and selecting the corresponding kinematical region.

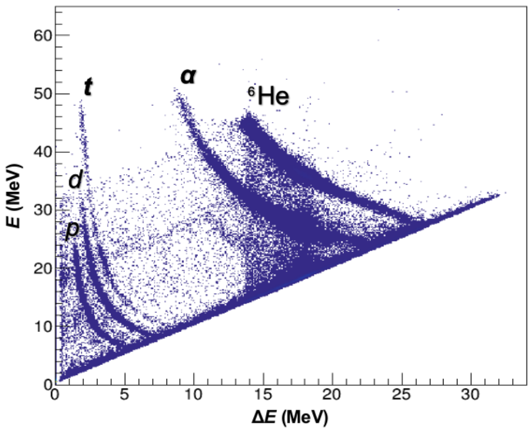

Figure 2: ΔE-E plot of the detected particles at the telescope 1. In the figure the different reaction products are indicated.

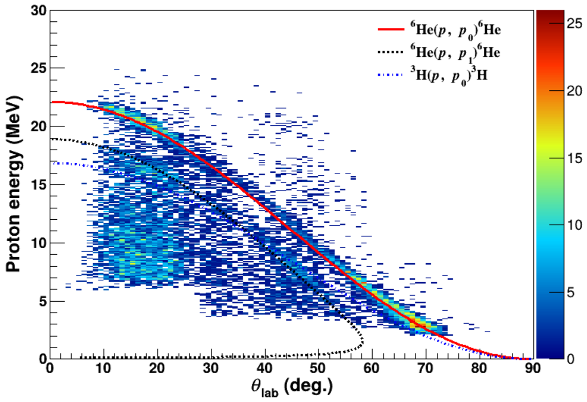

Figure 3: Proton energy versus θ_{lab} of proton with the kinematic curves of the ^{6}He(p, p_0)^{6}He (solid curve), ^{6}He(p, p_1)^{6}He (dashed curve) and ^{3}H(p, p_0)^{3}H (dashed-dotted curve) reactions.

References

[1] S. V. Stepantsov *et al.*, Phys. Lett. B **542**,35 (2002).
[2] P. Descouvemont, C. Daniel, D. Baye, Phys. Rev. C **67**, 044309, (2003).
[3] L. Giot *et al.*, Phys. Rev. C **71**, 064311 (2005).
[4] R. Wolski *et al.*, Phys. Lett. B **467**, 8 (1999).
[5] H. Miya *et al.*, Nucl. Instr. and Meth. in Phys. Res. B **317**, 701 (2013).
[6] S. Hayakawa *et al.*, CNS Annual report 2022, CNS-RE-102, (2024).

Experimental Nuclear Physics: PHENIX Experiment at BNL-RHIC and ALICE Experiment at CERN-LHC

Measurement of long-range two-particle correlation and $v_2(\eta)$ over a wide pseudorapidity range in p–Pb collisions at $\sqrt{s_{\rm NN}}$ = 5.02 TeV

Y. Sekiguchi for the ALICE Collaboration

Center for Nuclear Study, Graduate School of Science, the University of Tokyo

1. Introduction

The measurements of long-range two-particle correlation are a useful tool to study the properties of Quark Gluon Plasma (QGP). Striking correlations over a long range in $\Delta\eta$ on the near side ($\Delta\varphi \sim 0$), the so-called "ridge," have been observed in heavy ion collisions at RHIC and the LHC [1, 2]. They are well understood as derived from the collective expansion of the initial collision geometry and its fluctuations in heavy-ion collisions. The ridge structure was also observed in small collision systems such as pp and p–Pb collisions [3]. Extending these measurements over a wider range in pseudorapidity and final-state particle multiplicity is important to understand better the origin of these long-range correlations in small collision systems. We present results on long-range two-particle correlations with pseudorapidity gap $|\Delta\eta| \sim 8$ and the second-order azimuthal anisotropy as a function of pseudorapidity in p–Pb collisions at $\sqrt{s_{\rm NN}}$ = 5.02 TeV. These measurements utilize the Forward Multiplicity Detector (FMD) to extract $v_2(\eta)$ over the unprecedented range of about 8 units of pseudorapidity ($-3.1 < \eta < 4.8$). This study greatly extends the previous study by CMS ($|\eta| < 2$) [4]. To gain a comprehensive understanding of the source of anisotropic flow in small collision systems, the results are compared with a hydrodynamic calculation.

2. Experimental condition

The main sub-detectors in this analysis are the FMD and the Time Projection Chamber (TPC). The TPC is used for charged particle tracking. It covers a pseudorapidity of $|\eta| < 0.8$, where a 2π coverage in azimuthal angle is ensured. The FMD is located at $-3.4 < \eta < -1.7$ (FMD3) and $1.7 < \eta < 5.1$ (FMD1,2) with 2π acceptance in azimuthal angle. The FMD counts the charged-particle multiplicities with a granularity of $\Delta\varphi = 1/20\pi$ and $\Delta\eta = 0.05$. For event trigger and centrality determination, the V0 detectors, which are located at $-3.7 < \eta < -1.7$ (V0C) and $2.8 < \eta < 5.1$ (V0A), are used. Minimum-bias events are triggered by using a coincidence signal between V0A and V0C. The positive pseudorapidity denotes the Pb-going direction.

3. Analysis

The two-particle correlations between the trigger and associated particles are measured as a function of the pseudorapidity difference $\Delta\eta$ and the azimuthal angle difference $\Delta\varphi$ for a given event. The associated yield ($N_{\rm asso}$) to a trigger particle as a function of $\Delta\eta$ and $\Delta\varphi$ between two charged particles is defined as

$$\frac{1}{N_{\rm trig}}\frac{d^2N_{\rm asso}}{d\Delta\eta d\Delta\varphi} = \frac{S(\Delta\eta,\Delta\varphi)}{B(\Delta\eta,\Delta\varphi)}, \qquad (1)$$

where $N_{\rm trig}$ is the total number of triggered particles in the event class, the signal distribution $S(\Delta\eta,\Delta\varphi) = \frac{1}{N_{\rm trig}}\frac{d^2N_{\rm same}}{d\Delta\eta d\Delta}$, is the associated yield per trigger particle in the same event, and the background function $B(\Delta\eta,\Delta\varphi) = \alpha\frac{d^2N_{\rm mixed}}{d\Delta\eta d\Delta\varphi}$ is the pair yield between trigger in one event and associated particles from other events with the same multiplicity and primary-vertex position along the beam direction. The α factor is chosen so that $B(\Delta\eta,\Delta\varphi)$ is unity at the bin with the maximum value.. By dividing $S(\Delta\eta,\Delta\varphi)$ by $B(\Delta\eta,\Delta\varphi)$, pair acceptance and pair efficiency are corrected. Top three panels in Fig. 1 show the associated yield per unidentified hadron trigger particles for TPC-FMD1,2 (left), TPC-FMD3 (center), and FMD1,2–FMD3 correlations (right) in 0–5% central events. On the other hand, for the 60–100% peripheral collisions, three panels of three conditions are shown in the down. For all three combinations, the near-side ridge structure is observed in the 0–5% event class, while no significant ridge is observed in 60–100%.

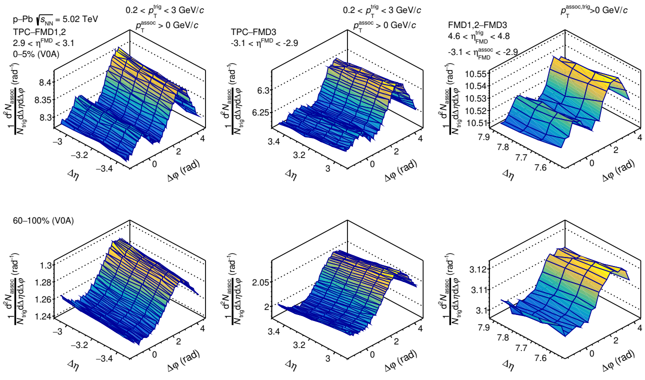

Figure 1: Correlation functions between TPC-FMD1,2 (left), TPC-FMD3 (center), and FMD1,2-FMD3 (right) in 0–5% (top) and 60–100% (bottom) p–Pb collisions.

The template fitting procedure [5] is employed to estimate and subtract the non-flow contamination due to dijet. The correlation function $Y(\Delta\varphi)$ is assumed to be a superposition of a non-flow contribution, which is estimated by scaling the correlation function from peripheral events and the flow contribution. The template fit function is defined as

$$Y(\Delta\varphi) = FY_{\rm peri}(\Delta\varphi) + G\{1 + 2\sum_{n=2}^{3} V_{n,n}\cos(n\Delta\varphi)\} \qquad (2)$$

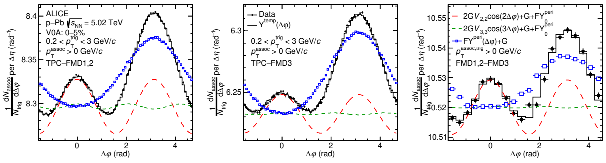

Figure 2: Projection of the correlation function of TPC–FMD1,2 (left), TPC–FMD3 (central), and FMD1,2–FMD3 (right) correlations in 0–5% p–Pb collisions with the template fit.

where $Y(\Delta\varphi)$ and $Y_{\mathrm{peri}}(\Delta\varphi)$ are the correlation functions in central and peripheral events, respectively. $F, G, V_{n,n}$ are free parameters. Assuming that the relative modulation of the two-particle correlation function is solely due to the modulation of the single-particle distribution, the modulation of the two-particle correlation measured in two different pseudorapidity ranges for particles A and B can be factorized as $V_{2,2}(\eta_A,\eta_B) = v_2(\eta_A)v_2(\eta_B)$. If this factorization holds, for example, the second azimuthal anisotropy at the TPC acceptance is obtained by three relative modulations of TPC-FMD1,2, TPC-FMD3, and FMD1,2-FMD3 as

$$v_2(\eta^{TPC}) = \sqrt{\frac{V_{2,2}(\eta^{TPC},\eta^{FMD1,2})V_{2,2}(\eta^{TPC},\eta^{FMD3})}{V_{2,2}(\eta^{FMD1,2},\eta^{FMD3})}}, \tag{3}$$

which is the so-called “3×2PC” method. Figure 3 shows the p_{T}-integrated v_2 as a function of η for the 0–5%, 5–10%, 10–20%, and 20–40% centrality classe. Non-zero v_2 is observed at $-3.1 < \eta < 4.8$ in up to 0–40% p–Pb collisions. It suggests the formation of collectivity across the entire pseudorapidity region. Figure 3 also shows comparisons with the (3+1)D hydrodynamic model, which employs 3D Glauber-initial conditions, viscous hydrodynamics based on MUSIC, and the UrQMD model to simulate the dynamics in the hadronic phase [6]. The hydrodynamic model qualitatively describes data for all centrality classes over the entire pseudorapidity region. It suggests that the collectivity exists over a wide rapidity region in small collision systems and v_2 mainly originates from the 3D initial geometry and develops over the course of the hydrodynamic evolution.

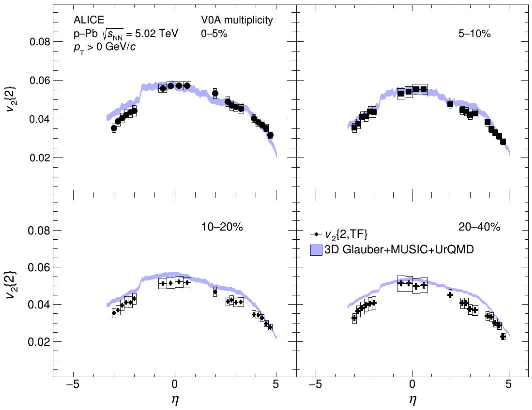

Figure 3: p_{T}-integrated v_2 as a function of η in various centrality classes and comparisons with the (3+1)D hydrodynamic calculation.

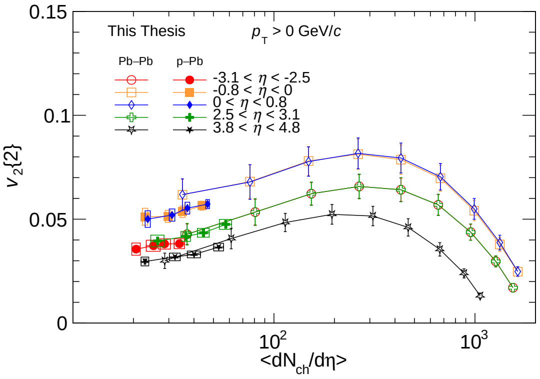

Figure 4: v_2 as a function of charged-particle pseudorapidity density for five different pseudorapidity regions in p–Pb and Pb–Pb collisions.

Figure 4 shows v_2 as a function of charged-particle multiplicity density for five different pseudorapidity regions in p–Pb collisions at $\sqrt{s_{\mathrm{NN}}} = 5.02$ TeV and Pb–Pb collisions at $\sqrt{s_{\mathrm{NN}}} = 2.76$ TeV. The v_2 in Pb-Pb is obtained by the standard Q-cumulant method with non-flow subtraction using pp collisions [7]. It is found that the pseudorapidity dependence of v_2 is not just simply driven by the local multiplicity; v_2 independently depends on both η and $dN_{ch}/d\eta$ and the v_2 smoothly transitions from p–Pb to Pb–Pb within the error range.

4. Summary

The long-range two-particle correlations are measured using TPC and FMD in p–Pb collisions. The long-range correlations are observed up to $\Delta\eta \sim 8$. Non-zero v_2 is observed over a wide pseudorapidity range, which is extracted using the 3×2PC method. The hydrodynamic model describes the data over the entire rapidity region in up to 0–40%. It suggests that the collectivity exists over a wide rapidity region in small collision systems and v_2 mainly originates from the 3D initial geometry and develops over the course of the hydrodynamic evolution. In the same rapidity region, v_2 scales with the charged-particle multiplicity density, and the v_2 smoothly transitions from p–Pb to Pb–Pb within the error range. It suggests that there is a common underlying physics between small and large systems.

References

[1] PHOBOS Collaboration, Phys. Rev. Lett. **104**, 062301 (2010).
[2] ALICE Collaboration, Phys. Lett. B **708**, 249 (2012).
[3] CMS Collaboration, JHEP **09**, 091 (2010).
[4] CMS Collaboration, Phys. Rev. C **96**, 014915 (2017).
[5] ATLAS Collaboration, Phys. Rev. Lett. **116**, 172301 (2016).
[6] W. Zhao et al. arXiv:2203.06094 (2022).
[7] ALICE Collaboration, Phys. Lett. B **762**, 376 (2016) .

Production of direct photons via internal conversions in Pb–Pb collisions at $\sqrt{s_{\rm NN}}$ = 5.02 TeV with ALICE at the LHC

D. Sekihata and T. Gunji

Center for Nuclear Study, Graduate School of Science, University of Tokyo

1. Introduction

The goal of performing high-energy heavy-ion collisions is to understand the properties of the quark-gluon plasma (QGP), which is a phase of matter composed of deconfined quarks and gluons under extreme conditions at high temperature and high energy density [1, 2]. Photons and dileptons are one of the tools to investigate the space-time evolution of the high-energy heavy-ion collisions. These electromagnetic probes are produced by various sources during the entire evolution and traverse the medium without strong interaction. Thus, they carry undistorted information at the time of their production [3].

Thermal photons emitted from partonic and hadronic phases, and prompt photons produced by the initial hard scattering are called direct photons. Thermal photons carry information on the thermodynamics of the system and prompt photons are suitable for testing perturbative QCD (pQCD) calculations. Since experimental photon yields are dominated by background due to photons from hadronic decays, the decay photons are simulated and subtracted. The simulated decay photons, so called "hadronic cocktail", are based on their measured yields with realistic detector resolution. For the non-measured hadrons, their transverse momentum ($p_{\rm T}$) spectra are scaled from the measured pions called $m_{\rm T}$-scaling technique.

The measurement of real direct photons at low $p_{\rm T}$ is challenging due to the large background from π^0 decays which amounts $\sim$ 85% of total backgrounds, followed by $\eta \sim$ 12%, $\omega \sim$ 2% and $\eta' \sim$ 1%. An alternative approach to measure the direct photons is to measure direct virtual photons via dielectron channels [4]. One of the advantages of dielectrons compared to real photons is that the dominant background of π^0 decays is significantly reduced by measuring virtual direct photons in the dielectron invariant mass ($m_{\rm ee}$) region above the π^0 mass of 135 MeV/c^2. The fraction of direct virtual photons over inclusive virtual photons in the kinematic range of quasi-real photons ($p_{\rm T,ee} \gg m_{\rm ee}$) is expected to be equivalent to that of real photons in the mass-less limit $m_{\rm ee} \to 0$ [5]. Therefore, the measurement of direct virtual photons decaying into dielectrons is independent and complementary to that of direct real photons.

2. Analysis

In November and December of 2018, ALICE took data in Pb–Pb collisions at $\sqrt{s_{\rm NN}}$ = 5.02 TeV with enhanced triggers for central and semi-central collisions. The number of events for physics analyses is 65 M in the 0-10% and 55 M in the 30-50% centrality classes respectively. In this analysis, charged particles with $p_{\rm T} > 0.2$ GeV/c and pseudorapidity $|\eta| < 0.8$ are selected. The tracking detectors at the central barrel of ALICE are Inner Tracking System (ITS) consisting of 6 silicon layers and Time Projection Chamber (TPC). For the electron identification, the specific ionizing energy loss in unit length dE/dx measured in ITS, TPC and the time of flight with the TOF detector are used.

In the pair analysis, there are huge combinatorial backgrounds in unlike-sign pairs (ULS: e^+e^-). The combinatorial background is estimated by the like-sign technique (LS: e^+e^+ or e^-e^-). Signal S is defined as

$$S = N_{+-} - 2R\sqrt{N_{++}N_{--}},$$

where R is a correction factor for different detection efficiencies between electrons and positrons obtained from the event mixing technique by

$$R = \frac{N_{+-}^{\rm mix}}{2\sqrt{N_{++}^{\rm mix}N_{--}^{\rm mix}}}$$

The reconstruction efficiency for dielectron pairs is evaluated in the Monte-Carlo simulation together with detector response.

3. Results and discussions

The efficiency-corrected dielectron invariant mass ($m_{\rm ee}$) spectrum is shown in Figure 1.

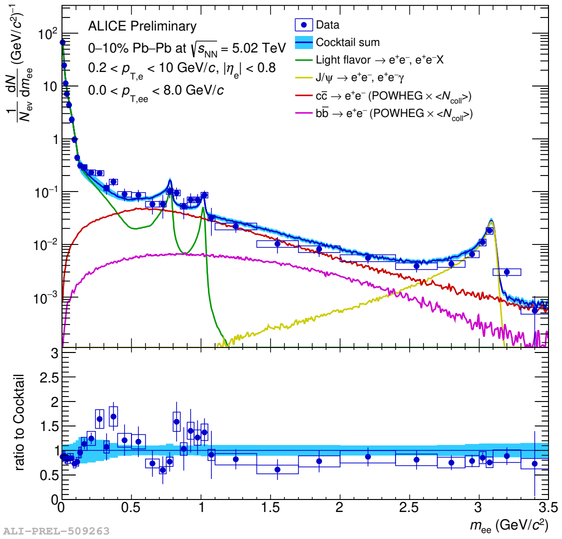

Figure 1: The $m_{\rm ee}$ spectrum in 0–10% central Pb–Pb collisions at $\sqrt{s_{\rm NN}}$ = 5.02 TeV. The vertical bar shows statistical error, while the box shows the systematic error.

Then, the direct virtual photon signal is extracted from the $m_{\rm ee}$ spectrum with the template fit consisting of 3 components. The fitting function is defined as

$$\frac{dN}{dm_{ee}} = rf_{\rm dir} + (1-r)f_{\rm LF} + f_{\rm HF},$$

where $f_{\rm LF}$ is the light-flavor cocktail, $f_{\rm HF}$ is the heavy-flavor cocktail and $f_{\rm dir}$ is the direct photon template given by Kroll-Wada formula [5] which describes the relation between real photon production and dielectron production. The r is the only free parameter and is interpreted as direct photon fraction ($\gamma^{\rm direct}/\gamma^{\rm inc}$). In order to avoid the $\pi^0 \to e^+e^-\gamma$ (Dalitz) decays, The fitting is performed in the mass range of $0.12 < m_{\rm ee} < 0.34$ GeV/c^2. Both $f_{\rm dir}$ and $f_{\rm LF}$ are separately normalized to the data at $m_{\rm ee} < 30$ MeV/c^2, because a process dependent factor of the π^0 Dalitz decay is close to unity in this mass region. Thus, the functional forms of $f_{\rm dir}$ and $f_{\rm LF}$ are identical. $f_{\rm HF}$ is in absolute yield. An example of the template fit is shown by Figure 2.

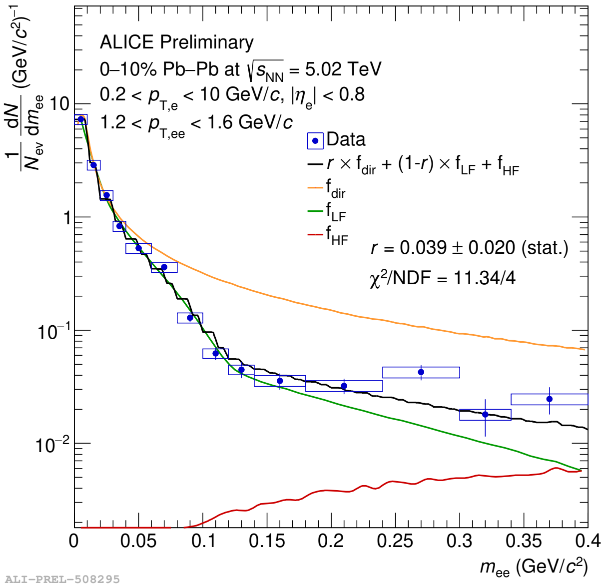

Figure 2: The template fit for direct photon extraction in 0–10% central Pb–Pb collisions at $\sqrt{s_{\rm NN}} = 5.02$ TeV for $1.2 < p_{\rm T} < 1.6$ GeV/c.

Finally, the direct photon yields are constructed by $\gamma^{\rm dir} = r\gamma^{\rm inc}$. The inclusive photon $\gamma^{\rm inc}$ is measured with photon conversion method at the same energy in the same centrality class. Figure 3 shows the $p_{\rm T}$ spectrum of the direct photon in 0–10% central Pb–Pb collisions at $\sqrt{s_{\rm NN}} =$ 5.02 TeV compared with theoretical models. The dominant systematic uncertainty is due to the fit range variation and the light-flavor cocktail. The new ALICE data points are slightly higher than the pQCD calculation (i.e. photons from hard scatterings at the initial stage). On the other hand, the state-of-the-art model [6] including photons from pre-equilibrium, thermal radiations and hard photons tends to overpredict the direct photon yields at low $p_{\rm T}$.

4. Summary

The measurement of dielectron production is performed in 0–10% central Pb–Pb collisions at $\sqrt{s_{\rm NN}} = 5.02$ TeV. The virtual photon signal is extracted from the mass range of $0.12 < m_{\rm ee} < 0.34$ GeV/c^2. The direct photon yields are higher than the pQCD calculation, which can be interpreted as thermal contributions. On the other hand, the state-of-the-art model including photons from pre-equilibrium, thermal radiations and hard photons tends to overpredict the direct photon yields at low $p_{\rm T}$.

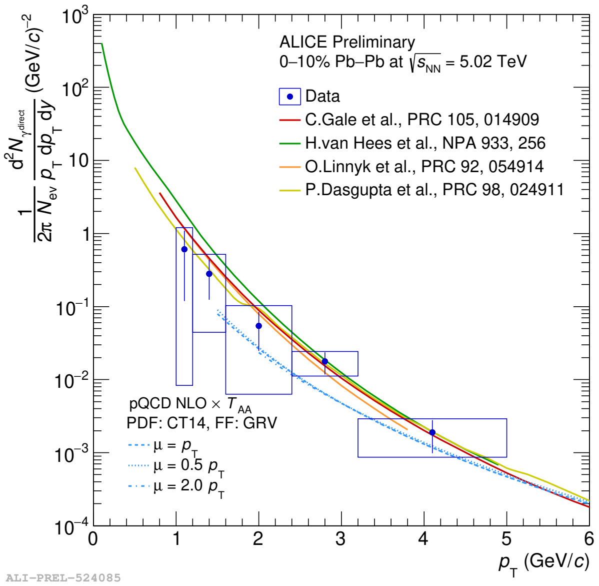

Figure 3: The direct photon spectrum in 0–10% central Pb–Pb collisions at $\sqrt{s_{\rm NN}} = 5.02$ TeV compared with theoretical models.

References

[1] A. Bazavov et al., Phys. Rev. D **85**, 054503 (2012)

[2] S. Borsányi et al., Phys. Lett. B **730** 99-104 (2014)

[3] J. E. Alam et al., Phys. Rep. **273**, 243 (1996)

[4] A. Adare et al. (PHENIX Collaboration), Phys. Rev. C **81**, 034911 (2010)

[5] Norman M. Kroll and Walter Wada, Phys. Rev. **98**, 1355 (1955)

[6] C. Gale et al., Phys. Rev. C **105**, 014909 (2022)

Accelerator and Instrumentation

Position finding algorithm for SR-PPAC

R. Kojima, S. Hanai, S. Ota[a], M. Dozono[b], N. Imai, S. Michimasa[c], S. Shimoura[c], J. Zenihiro[b], K. Inaba[d], Y. Hijikata[b c]

Center for Nuclear Study, Graduate School of Science, University of Tokyo
[a]*Research Center for Nuclear Physics, Osaka University*
[b]*Department of Physics, Kyoto University*
[c]*RIKEN (The Institute of Physical and Chemical Research)*
[d]*QST (National Institutes for Quantum Science and Technology)*

1. Introduction

Strip Readout PPAC (SR-PPAC) has been developed in CNS as a tracking detector for high intensity RI beams [1–3]. The SR-PPAC is a parallel plate avalanche counter with an anode plane sandwiched between two cathode planes. One of the cathode is segmented as strips in horizontal (X) direction while the other in vertical (Y) direction. When a beam penetrates the SR-PPAC perpendicular to the plates (Z direction), filling gas in the SR-PPAC is ionized and the ionized electrons make an avalanche while they are traveling to the anode. The positive ions exposed after the electron transit induces the mirror charges on the cathode strips near the avalanche point. The mirror charge on every cathode strip is recorded by the read-out system. The Position Finding Algorithm (PFA) in our analysis uses a response function between the observed signal strength and the event number assuming an uniform distribution of the beam injection over the strip [4]. This method is very powerful because it needs only intrinsic properties of the signals. However, with this method we can not predict the systematic error of the PFA. It is very important to optimize the detector configuration and improve the resolution. For that purpose, we examine two PFAs using the induced charge profile on the cathode and compare the predicted errors with the experimental data.

2. Induced charge profile on cathode

The induced charge profile can be calculated by solving the boundary problem of the potential between the anode and the cathode and by using the reciprocity theorem [5,6]. The mirror charge density at (x,y) on the cathode is given by

$$\begin{aligned}\sigma(x,y) = \quad & -\tfrac{4N_{\rm ini}}{ab}\textstyle\sum_{n,m=0}^{\infty}\sin(\alpha_n x)\sin(\alpha_n x_0)\times \\ & \sin(\beta_m y)\sin(\beta_m y_0)\tfrac{\sinh[\gamma_{nm}(D-z_0)]}{\sinh(\gamma_{nm}D)},\end{aligned} \tag{1}$$

$$\alpha_n = \frac{n\pi}{a},\ \ \beta_m = \frac{m\pi}{b},\ \ \gamma_{nm} = \pi\sqrt{\frac{n^2}{a^2}+\frac{m^2}{b^2}}. \tag{2}$$

where (x_0, y_0, z_0) is the ion position with total charge $N_{\rm ini}$ between the anode and the cathode, a and b are the electrode's size in X and Y and D is the gap between the anode and the cathode. z_0 is measured from the anode surface. Because the number of avalanche ions increases exponentially along Z direction, the charge density caused by the avalanche ions is obtained by integrating all the ions as

$$\sigma_{\rm ava} = \int_0^D \frac{\exp(\alpha z)}{D}\sigma(x,y)dz, \tag{3}$$

where α is the number of produced secondary ion per unit length. The integration of the charge density $\sigma_{\rm ava}$ over the strip widths w in X and b in Y gives the charge amount on one X strip. When the avalanche point locates $0 < x_0 < \frac{w}{2}$, the mirror charge on the most and the second most significant strips become

$$\mathscr{Q}_0(x_0) \quad = \textstyle\int_{-\frac{w}{2}}^{\frac{w}{2}}\int_{-\frac{b}{2}}^{\frac{b}{2}}\int_0^D \frac{\exp\{(\alpha z)\}}{D}\sigma(x,y)dxdydz \tag{4}$$

$$\mathscr{Q}_1(x_0) \quad = \textstyle\int_{\frac{w}{2}}^{\frac{3w}{2}}\int_{-\frac{b}{2}}^{\frac{b}{2}}\int_0^D \frac{\exp\{(\alpha z)\}}{D}\sigma(x,y)dxdydz. \tag{5}$$

The total charge on the cathode is given as

$$\begin{aligned}Q_{\rm cath} = -\tfrac{4N_{\rm ini}}{\pi^2}\textstyle\int_0^D\sum_{n,m=0}^{\infty}\frac{1-(-1)^n}{n}\frac{1-(-1)^m}{m}\times \\ \exp\{(\alpha z)\}\sin(\alpha_n x_0)\sin(\beta_m y_0)\tfrac{\sinh[\gamma_{nm}(D-z)]}{\sinh(\gamma_{nm}D)}dz.\end{aligned} \tag{6}$$

Figure 1 shows the mirror charges Q_0 to Q_4 on the strips as a function of the distance from the strip center x_0 in a range of half strip width. All charges are normalized to the total charge $Q_{\rm cath}$. The gap D is 4.0 mm and the electrode size a and b are both 150 mm, αD is 11.1 and the strip width w is 2.58 mm. The summentions of n and m are carried out up to 100. In the calculation, the diffusion effect is not taken into account. The systematic errors of PFAs are predicted using this charge profile.

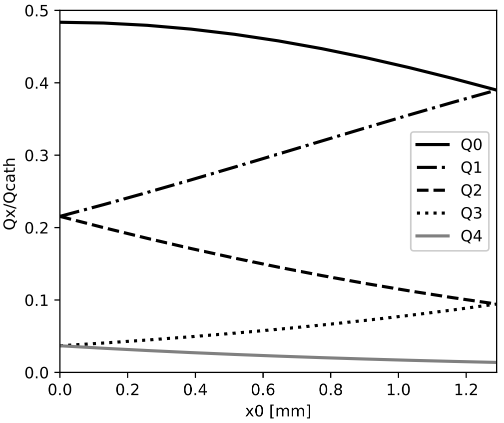

Figure 1: Mirror charges induced on the strips as a function of the avalanche position x_0 from the center of strip in the range $0 < x_0 < w/2$.

3. Charge information reconstruction

In our read-out system, charge information is converted to time duration of the digital signal by Amplifier-Shaper-Discriminator (ASD) board using the Time over Threshold (ToT) method [7]. It enables us to take charge information much faster than integrating the signal with a flash ADC. On the other hand, ToT method causes a strong non-linearity between the charge amount and the time duration. To use the mirror charge profile for the PFAs, the charge information should be reconstructed. It is done by simulating ASD circuit using the circuit simulator LTSpice. The induced current of the cathode strip I_{det} is an input of the circuit shown in Fig. 2. Details of the circuit can be found in Ref. [7]. In the limit of infinite size of the electrodes, the total charge on the cathode in Eq.6 can be simplified to

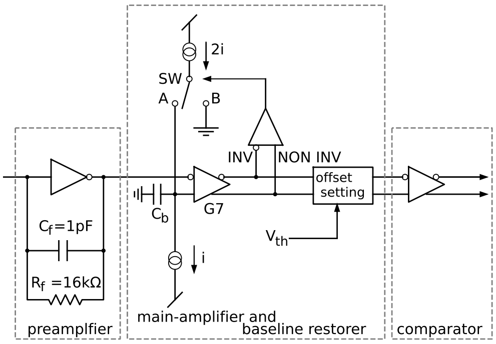

Figure 2: Block diagram of the ASD chip.

$$Q_{\text{cath}}(z) = \int_0^z \frac{N_{\text{ini}}}{D} \exp\{(\alpha z')\} \frac{D-z'}{D} dz'. \tag{7}$$

It is valid when the avalanche locates near the center of the electrodes. Then the induced current can be expressed as

$$I_{\text{det}} \propto -\frac{d}{dt} Q_{\text{cath}} = \frac{N_{\text{ini}}}{t_1} \left(1 - \frac{t}{t_1}\right) \exp\left\{\left(\alpha D \frac{t}{t_1}\right)\right\}, \tag{8}$$

where t_1 is the transit time of avalanche electrons from the gap D. Figure 3 shows I_{det} at the condition of $D = 4.0$ mm , $\alpha D = 11.1$, $t_1 = 24$ ns and the total charge is 1 pC. The electron transit time is simulated using Magboltz [8] applying the bias 690V between the anode and the cathode and filling i-C_4H_{10} gas at 10 Torr. These conditions are the same used in the position resolution measurement, whose data will be analyzed in Sec.5. Figure 4 shows the simulated signal time duration from the comparator out of the circuit with various input currents, whose total charges are indicated in the Y-axis. The multiplication by the avalanche (αD) is kept constant while the initial charge is changed. The solid line is the exponential curve fitted by the first 4 points in low input charge side. Using this curve, the charge amounts are reconstructed from the time duration before applying the PFAs. For each different setting of the gas type, the pressure of gas, the bias and the gap D, the conversion curve should be prepared.

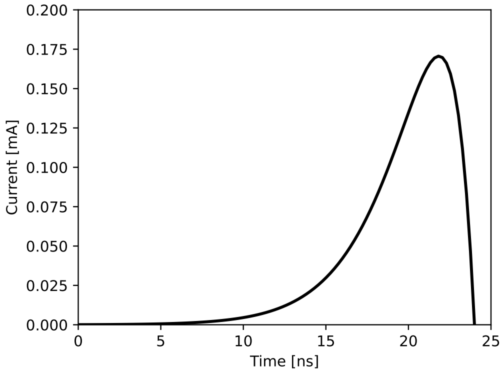

Figure 3: The cathode strip signal with the total charge 1 pC. The electron transient time is 24 ns.

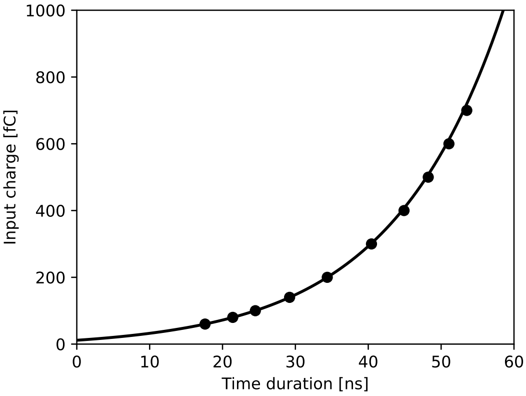

Figure 4: The simulated relation between the signal time duration from the ASD and the charge from the cathode strip.

4. Position finding algorithm

We test two PFAs commonly used for the segmented detectors. Both PFAs use the charge information from three strips. The first PFA is the ratio method [9, 10], which defines the avalanche position x_{ratio} as

$$x_{\text{ratio}} = \frac{w}{2} \left(\frac{Q_1 - Q_2}{Q_0 - Q_2} \right). \tag{9}$$

As seen from Fig. 1, $Q_1 - Q_2$ defines the triangular area between Q_1 and Q_2 lines and $Q_0 - Q_2$ defines the quadrilateral area between Q_0 and Q_2 lines. When the avalanche locates at the center of a strip ($x_0 = 0$), x_{ratio} becomes 0 because $Q_1 - Q_2 = 0$, while the avalanche occurs between the strip ($x_0 = w/2$), $Q_0 = Q_1$ resulting in $x_{\text{ratio}} = 1$. The systematic error of the ratio algorithm is shown as a solid line in Fig. 5. The error is continuous along the avalanche position. The second PFA is the generalized ratio method [11], which defines the angle κ as

$$\kappa = \tan^{-1} \left(\frac{Q_1 - Q_2}{Q_0 - Q_2} \right). \tag{10}$$

and the avalanche position x_{RG} as

$$x_{\text{GR}} = \frac{w}{2} \left(\frac{\tan^{-1}(b(\kappa - \pi/4))}{\tan^{-1}(b\pi/4)} \right). \tag{11}$$

b is the parameter chosen to minimize the systematic error. The systematic error of the generalized ratio method is

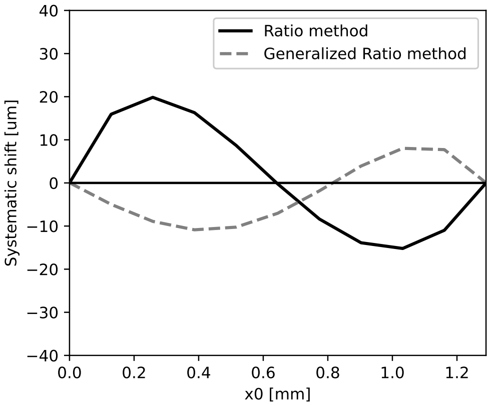

Figure 5: The predicted systematic error of the ratio method (solid line) and the generalized ratio method (broken line) as a function of true position in the range $0 < x_0 < w/2$.

shown as broken line in Fig. 5. In this case, $b = 1.27$ is chosen. The error is also continuous and its maximum value is about 10 μm smaller than that of the ratio method.

5. Comparison of data and model prediction

The data of position resolution measurement with ^{132}Xe beam at HIMAC [2] is analyzed using the two PFAs. In the experiment, two LP-MWDCs were used as a position reference. The results of X and Y planes are shown in Fig. 6 and in Fig. 7, respectively. In the top panels of the figures, the position differences between the reference (MWDC) and the position deduced by the ratio method (SRPPAC) are shown. The black dots show the data in the left half of the strips and the gray dots in the right half. The position difference distributions are shown in the bottom left panels. The gray dot lines are the Gaussians fitted to the data. The standard deviations are 118 μm in X and 124 μm in Y including the MWDC's resolution, 63 μm. The position resolutions of the SR-PPAC in sigma are thus 100 μm in X and 107 μm in Y, respectively. The black lines in bottom right panels show the average of position differences in each w/20 bin in the range $-w/2 <$ MWDC $< w/2$. There seems no discontinuity in the strip as predicted by the PFA models in Fig. 5. The periodic structure in the residual can not be seen. It might be because the predicted errors are much smaller than the obtained resolutions. The results of the generalized method are similar and not shown here. The systematic error difference might be also too small compared to the resolution. In conclusion, two PFAs using the charge distribution work well to give the similar resolutions to the result with the previous PFA. The systematic error seems smooth as predicted from the PFA models. Further analysis, for example the injection angle dependence and the signal height dependence, and the resolution measurements at the different conditions will be done in near future.

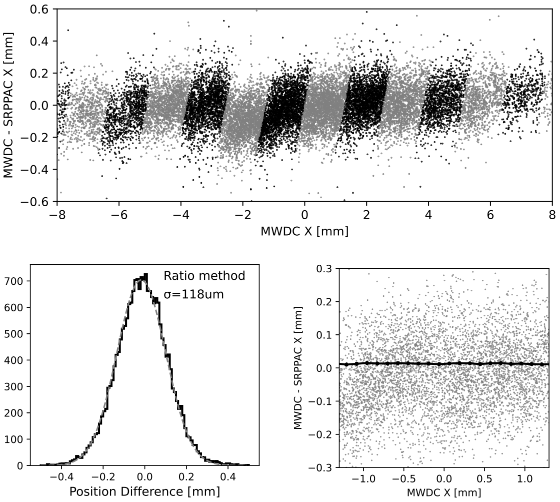

Figure 6: Residual in X plane as function of the reference position (top) and residual distribution and a Gaussian fitting result (bottom left) and the averaged residual in each w/20-size bin in the range $-w/2 <$ MWDC $< w/2$.

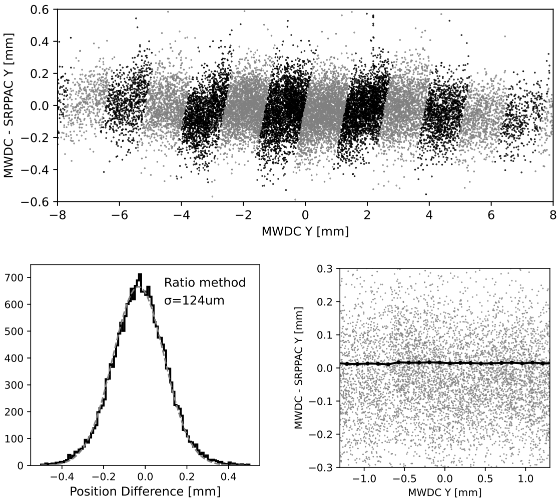

Figure 7: Same figure as Fig. 6 but of Y plane.

References

[1] R. Nakajima, Master thesis, The University of Tokyo, 2018.

[2] S. Hanai, *et,al.*, PTEP Vol.2023, Issue 12 (2023).

[3] S. Hanai, *et al.*, CNS Annual Report.2019 pp.47.(2021)

[4] S. Hanai, *et al.*, CNS Annual Report.2020 pp.35.(2022)

[5] J. .D. Jackson, Classical Electrodynamics. 2nd ed. (Wiley, New York. 1975).

[6] H. Sakasai, JAERI-Research 2004-017.

[7] ATLAS Thin Gap Chamber Amplifier-Shaper-Discriminator ICs and ASD Boards, ATLAS Internal Note MUON-NO-1 October, 1999.

[8] S. F. Biagi, Nucl. Instr. and Meth. A, **283**(1989), p. 716.

[9] J. Chiba, *et al.*, Nucl. Instr. and Meth. **206**(1982) 451.

[10]K. Lau and J. Pyrlik, Nucl. Instr. and Meth. A, **366**(1995), 209-309.

[11]H. van der Graff *et al.* Nucl. Instr. and Meth. A, **307**(1991) 220.

Readout test of SR-PPAC with ASAGI board

R. Tsuchiya[a], R. Kojima, S. Hanai, N. Kitamura, S. Michimasa[1] N. Imai[2]

Center for Nuclear Study, Graduate School of Science, University of Tokyo
[a]Department of Physics, Rikkyo University

At the RIBF, the intensity of unstable nuclear beams produced by nuclear reactions is increasing thanks to the enhancement of heavy ion beam intensity. Since heavy ion beams cause significant damage to detectors, beamline detectors with the minimal amount of material and high discharge immunity are required. The conventional beamline detectors for position detection at the RIBF are Delay line-PPAC (Parallel Plate Avalanche Counter). To increase the beam intensity tolerance and improve the position resolution, CNS is developing a Strip Readout-PPAC (SR-PPAC) [1], which can achieve better positional resolution through charge-weighted averaging. However, since the gain of the versatile RPA-132 type preamplifier is low, it is demanded to apply the higher bias to obtain sufficiently large signal, which increases the chance of spark. Also, these preamplifiers have been no longer manufactured. The purpose of this study is to evaluate the performance of SR-PPAC using ASAGI (AGASA based General Interface for wire) [2] with ASD card (Amplifier, Shaper, Discriminator card), which is being developed by the SPADI-Alliance led by RCNP of Osaka University, RIKEN Nishina Center, KEK, CNS University of Tokyo, and Tohoku University.

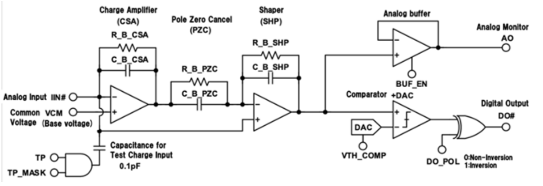

Figure 1: The configuration for one channel of the ASD circuit.

ASAGI incorporates an ASD card with four built-in functions: amplifier, shaper, discriminator, and pole zero cancellation. While the RPA-132 has a conversion gain of 0.8 V/pC, ASAGI can achieve a much higher conversion gain of 32 V/pC. ASAGI can also vary the conversion gain from 68 mV/pC to 32 V/pC by changing the combination of resistor and capacitance of the amplifier, pole zero cancellation, and shaper. Figure 1 is the diagram for one channel of the ASD circuit. The number of resistors connected can be varied from 1 to 4 and the number of capacitors from 1 to 8 using a dedicated parameter file to obtain amplified waveforms for various purposes. *R_B_SHP*, *C_B_SHP*, *R_B_PZC*, *C_B_PZC*, *R_B_CSA*, and *C_B_CSA* are the resistance of Shaper, the capacitance of the Shaper, the resistance of Pole Zero Cancellation, the capacitance of Pole Zero Cancelation, the resistance of Charge Amplifier, and the capacitance of Charge Amplifier, respectively.

First, as an experiment, a square wave from the pulsar was injected to the test input of ASAGI, where the same parameter file used in previous studies was used again to confirm the same output as observed in previous studies and different parameters were also used to examine the changes.

Square waveforms from a function generator (FCG) were applied to ASAGI's test pulse input (TP) at a frequency of 1.0 kHz . The input amplitude was 650 mV and the pulse width was 500 ns. An offset of +325 mV was set so that the voltage value at negative pulse was 0 V. The FCG output signal was split into two, and the one was connected to an oscilloscope with 1 MΩ to trigger the oscilloscope, and the other signal was amplified by ASAGI and the analog monitor output (analog output) was connected to the oscilloscope (50Ω impedance). In this experiment, *R_B_SHP* was varied from 1 to 4, and the remaining five, *C_B_SHP*, *R_B_PZC*, *C_B_PZC*, *R_B_CSA*, and *C_B_CSA* were all fixed to be 1.

The first step in the operation procedure was to create a parameter file corresponding to the settings. Next, the created parameter file was uploaded to FPGA through Python using SiTCP communication protocol. Then, the amplified waveforms were measured with an oscilloscope, and the imaging and waveform information were recorded in the experimental longnote. Figure 2 shows the relationship between the *R_B_SHP* and peak of the analog test output. This figure shows that the peak value increases as the resistance increases, however, the increase cannot be described as a linear increase.

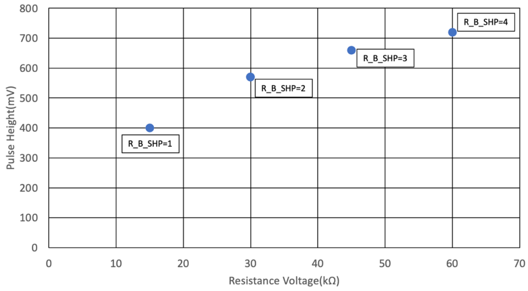

Figure 2: The peak height of test output as a function of the resistance.

Also, when SR-PPAC and ASAGI were connected via 2 m long SAMTEC cable, it was found that the capacitance of the cable, 24 pF/ft, lowers the pulse height of the ASAGI output. Therefore, we created a conversion board that allows SR-PPAC to be directly connected to ASAGI's input without cables. Figure 3 shows a photo of the modifled adopter board of SR-PPAC to the ASAGI, in which only

---

[1] Present affiliation:RIKEN Nishina Center

[2] Corresponding author

1 channel of ASAGI was connected to the SR-PPAC.

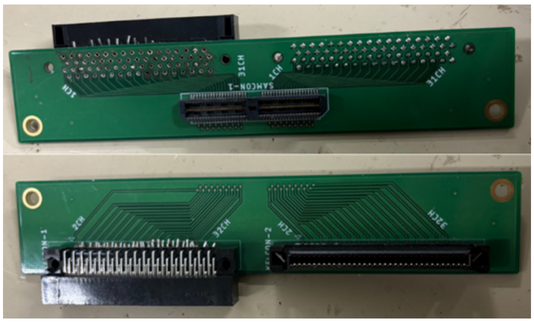

Figure 3: The adoptere board from SR-PPAC to the ASAGI.

The test signal from the BNC inc. pulsar was connected to the anode of the SR-PPAC and the signal from the SR-PPAC was amplified by ASAGI to evaluate how much its amplified signal was improved when the cable was replaced with the converter board. The parameters were set to $R\_B\_SHP = 4$, $C\_B\_SHP = 1$, $R\_B\_PZC = 1$, $C\_B\_PZC = 4$, $R\_B\_CSA = 4$, and $C\_B\_CSA = 1$. This is the setting where the conversion gain is the highest at 32 V/pC. The test signals were set to a frequency of 1.000 kHz, a rise time of 0.05 μs, a fall time of 0.5 μs, an amplitude of 0.13137 V, and a signal width of 1.00 ms. The experimental results are shown in Fig. 4. The blue line shows the analog output when the conversion board was used, and the orange line shows the analog output when the cable was used. The peak values were 626 mV for the board and 295 mV for the cable, and the FWHMs were 88 ns for the converter board and 128 ns for the cable, respectively. When using the samtec cable, the rise time was longer than the case with the adopter board by 24 ns. The small pulse height was caused by the large capacitance of the cable.

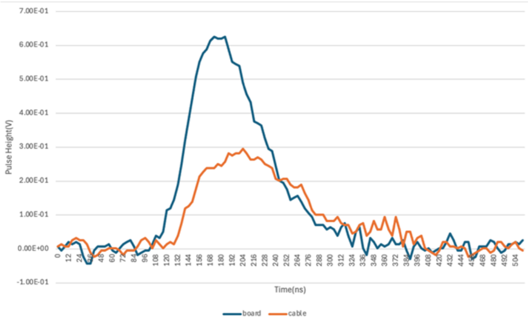

Figure 4: The outputs of the ASAGI with and without the samtec cable between the SR-PPAC and the ASAGI board. See the text for the detail.

The present study indicates that the direct connection of the ASAGI to the SR-PPAC is important to get the fast signals. Since two ASAGI cards are needed for one SAMTEC connector of SR-PPAC, and there are three SAMTEC connectors in a SR-PPAC, it is necessary to design a conversion board that can hold six ASAGI cards. The following four conditions are necessary for development.

- there are three SAMTEC connectors (64-pin) (SAMTEC-QTE-040-01-X-D) on the SR-PPAC.
- two KEL connectors (68pin) (FX2C-68P-1.27DSAL(71)) of ASAGI must correspond to one SAMTEC connector.
- the path difference within the board should be as small as possible.
- each of the 6 ASAGI connectors should be able to be used as a test input and analog output.

Based on the above, we are currently designing the board using EAGLE board design software. The future outlook, though, is, the SR-PPAC is installed in a vacuum chamber. The board we are designing will be ordered to a company, and all channels of SR-PPAC will be read by ASAGI. The final goal is to optimize the parameter files of ASAGI for SR-PPAC.

References

[1] S. Hanai *et al.*, NIMB 541, 194 (2023).
[2] Open-It KEK / R&D Project / ASIC for Gas Amp Shaper discriminAtor (AGASA), https://openit.kek.jp/project/agasa

Simulation Study of Prototype Silicon Pixel Sensor for ALICE Detector Upgrade

T. Katsuno, Y. Yamaguchi, T. Gunji[a]

Graduate School of Advanced Science and Engineering, Hiroshima University
[a]Center for Nuclear Study, Graduate School of Science, University of Tokyo

1. Introduction

Understanding of the properties of the Quark Gluon Plasma (QGP) is one of the goals for the ALICE experiment through various particle measurements. During the LHC Long Shutdown 3 (LS3), ALICE plans to replace the two most-inner layers of the Inner Tracking System (ITS) based on a new Monolithic Active Pixel Sensor (MAPS) [1]. Subsequently a new detector complex based on the newly developed MAPS detectors is proposed for the ALICE 3 experiment as the successor of ALICE after the LS4. Advantages of the new MAPS are reduction of material budget, improvement of the position resolution, increase of the flexibility, low power consumption and so on.

The 65 nm-CMOS technology enables higher integration for improving the position resolution as well as thinner sensor thickness for reducing material budget [2]. It refers to the process used to manufacture integrated circuits with a minimum feature size of 65 nm. A sensor can be thinned to less than 50 μm with the minimum pixel size of 15 μm×15 μm.

The first beam test in Japan was conducted in last March with the Korean ALICE group to validate prototype MAPS chips with different geometries [3]. A lot of efforts are being made for assessment of detailed specifications, including an optimal pixel size, sensor structure, readout and so on. The simulation study of the new MAPS response is ongoing with Allpix Squared simulation [4]. Comparisons of the simulation data with the beam test data are crucial for understanding the new MAPS response such as the motions of electrons and holes inside a sensor, the charge sharing capability. The multiple scattering effect is evaluated by simulation using reasonable beam size and injection direction. In this report, the current status of the simulation study of the new MAPS response is described.

2. Allpix Squared Simulation

Allpix Squared is a simulation tool specially dedicated to semiconductor based on GEANT4. It can simulate electron and hole motions in a sensor when electrons and holes are produced by energy deposit due to the passage of charged particles. The telescope configuration of the beam test is implemented in the simulation and the telescope analysis has been done in the exact same way with the beam data analysis [3].

The following settings are equivalent to the experimental conditions. Figure 1 shows the simulated telescope setup. A 3 GeV/c electron is injected to the telescope in one event and its injection direction is indicated by an arrow in Fig. 1. To reduce a data size, the beam focal point is limited within 50 μm, equal to about 4 pixels×4 pixels at the center of DUT. The position of each chip is shifted slightly to reproduce the actual experimental condition. The prototype sensor as the device under test (DUT) is sandwiched between three reference planes (RPs) on each side. It is noted that the electric field inside the sensor is assumed to be linear due to unavailability of the actual field map. A realistic field needs to be implemented in the near future, but the qualitative characterization of the chip response can be done with the current simulation condition. The DUT back bias voltage is 3 V to 10 V, and the pixel size is 22.5 μm×22.5 μm with a matrix size of 48×28. The RP back bias is 3 V, and the pixel size is 27 μm×29 μm with a matrix size of 512×1024.

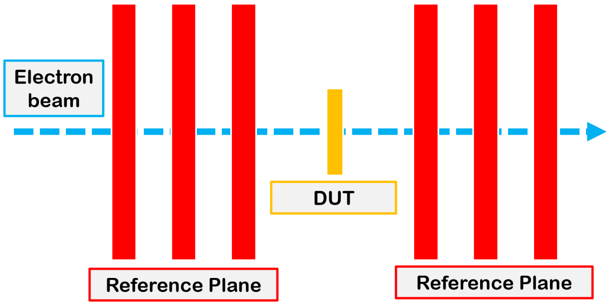

Figure 1: Telescope setup in simulation. An arrow indicates the electron beam direction. DUT is sandwiched between three RPs on each side.

3. Telescope Analysis

A cluster size is defined as the number of pixels with charge in one event. A seed charge is the largest charge signal in a cluster and some fraction of a total charge is shared to surrounding pixels around the seed pixel. Figure 2 shows the cluster and seed charge distributions for DUT. The closed and open symbols represent the cluster and seed charge distributions, respectively. They can be fitted well with a Landau-Gaussian indicated by solid lines.

Figure 3 shows the DUT cluster size distribution with 10 V back bias voltage. The averaged DUT cluster size is about 2, which is similar to the real data. A signal is sometimes spread in more than 4 pixels in the case of a tilted beam. A beam hit position, x_{hit}, at DUT is reconstructed by center-of-gravity calculation using the charge and position information of a cluster.

The expected hit position, x_{exp}, is obtained using extrapolation of the particle track calculated by hits of 6 RPs. The residual is calculated by $x_{hit} - x_{exp}$ in each event. Figure 4 shows the DUT residual distribution with a Gaussian fit. The residual distribution is well-described by Gaussian. The position resolution is defined as the width of the Gaussian fit. The obtained position resolution in the x axis is 9.37±0.06 μm and the resolution in the y axis is consistent too. It is larger than 6.50 μm which is calculated as the pixel pitch divided by $\sqrt{12}$. The charge sharing efficiency and multiple scatterings may make the position resolution larger.

Figure 5 shows the DUT hit maps with 3 and 5 GeV/c electrons. The initial beam size is 50 μm radius. However, the hit region of DUT is much larger than the initial beam size. The hit region with 5 GeV/c electrons is smaller than the one with 3 GeV/c electrons. Thus, the beam spreading is due to multiple scatterings by passing through RPs and the air.

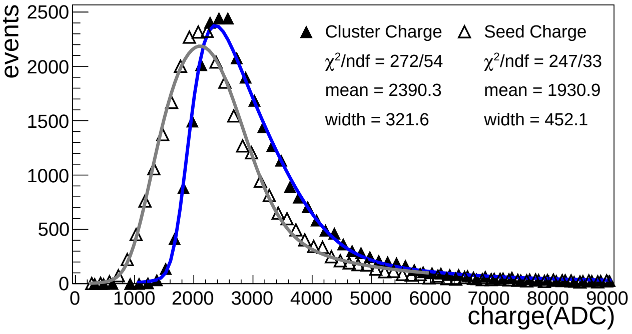

Figure 2: Cluster and seed charge distributions for DUT with 10 V back bias voltage. The closed and open symbols represent the cluster and seed charge distributions together with Landau-Gaussian fits.

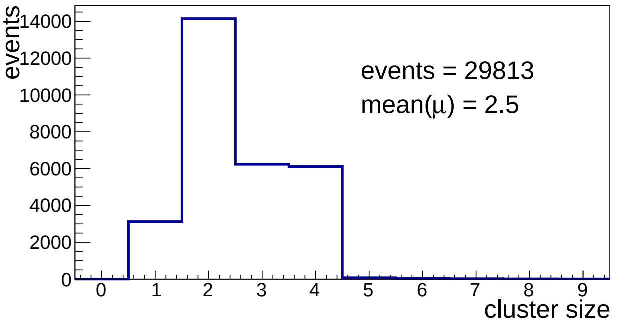

Figure 3: Cluster size distribution for DUT with 10 V back bias voltage.

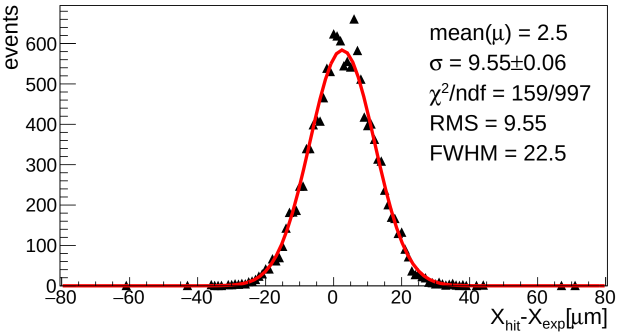

Figure 4: The residual ($x_{hit} - x_{exp}$) distribution in the x axis for DUT with 10 V back bias voltage. The expected hit position, x_{exp}, is obtained from tracking with only RPs. The reconstructed hit position of the DUT signal is x_{hit}.

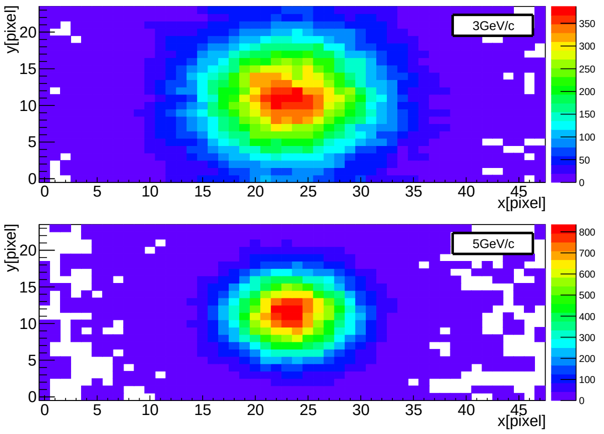

Figure 5: Hit maps on DUT with 10 V back bias voltage with 3 GeV/c (top) and 5 GeV/c (bottom) electrons.

4. Summary and Outlooks

The new MAPS detector has been developed for the upgrade of the current ITS as well as ALICE 3. Telescope simulation for prototype MAPS characterization has been done using the Allpix Squared. The simulated position resolution of the MAPS results in 9.37 μm, which is larger than the ideal value. It is figured out that multiple scatterings before the MAPS makes the resolution worse. Further study with a realistic field configuration will be performed for quantitative characterization of the new MAPS response.

References

[1] ALICE collaboration, CERN-LHCC-2024-003/ALICE-TDR-021 (2024).
[2] M. Manghisoni *et al.*, Nucl. Instr. Meth. A **624** (2010) 373.
[3] R. Wada *et al.*, CNS Annual Report 2023.
[4] S. Spannagel *et al.*, Nucl. Instr. Meth. A **901** (2018) 164.

Characterization of 65 nm-CMOS silicon sensor developed for ALICE 3 Outer Tracker

R. Wada, T. Gunji[a], T. Katsuno, R. Kohara[a], H. Murakami[b], Y. Yamaguchi,
on behalf of ALICE 3-J and KoALICE teams

Graduate School of Advanced Science and Engineering, Hiroshima University
[a] *Center for Nuclear Study, Graduate School of Science, University of Tokyo*
[b] *Kobayashi-Maskawa Institute for the Origin of Particles and the Universe, Nagoya University.*

1. Introduction

The ALICE 3 experiment will begin from 2035 for further study of Quark-Gluon Plasma (QGP). The main part of the ALICE 3 detector will be composed of state-of-art silicon pixel detectors based on a new CMOS sensor technology. Various measurements including heavy quark hadrons can be performed thanks to an excellent tracking capability of the ALICE 3 detector, providing deeper insights on important QCD phenomena such as quark confinement, a partial restoration of the chiral symmetry breaking and so on.

The Monolithic Active Pixel Sensor (MAPS) is one of the next generation silicon pixel detectors based on a fine-pitch CMOS technology. A sensor and a readout circuit are implemented on the same chip. Its beneficial features are a high density pixel matrix with an extremely thin material, low power consumption and so on. In particular, the 65 nm-CMOS technology is the cutting edge technology for a MAPS detector and prototype 65 nm-CMOS MAPS sensors are under development for the Vertex detector and the Outer tracker for ALICE 3 [1]. Extensive efforts are underway to characterize the prototype MAPS sensors. In this report, the current status of the prototype sensor characterization is described, especially through the telescope beamtest at PF-AR in KEK in the March 2024.

2. Telescope test at KEK PF-AR beam line

The prototype MAPS sensors have been produced with three types of an internal electric field structure [2], namely Standard, Modified, Modified with a gap, respectively. The Standard sensor has a limited depleted region while a fully depleted region is realized in the Modified one with an additional low-dose n-type implant. A gap in the n-type implant increases the lateral electric field and the speed of the charge collection. These structural differences lead to differences in electron and hole collection efficiencies as well as charge sharing capability.

The first prototype MAPS characterization was done at the KEK PF-AR beam line. 3 GeV/c electrons were injected into a telescope setup with approximately 130 Hz/cm^2 and a size of 8×2 cm^2 (x-y size of beam). Figure 1 shows the telescope setup consisting of one device under test (DUT), six reference planes (RPs), and two scintillators. A chip size of the prototype MAPSs as DUT is 1.08×0.54 mm^2 containing 48×24 pixels with a pitch of 22.5 μm. All prototype MAPSs with different electric field structures were tested. First an analog signal from DUT goes through the proxy board for conversion of a data format which can be read by a DAQ board. The ALPIDE sensors [2], developed for the Inner Tracking System 2 (ITS2) currently running in ALICE, were used for RPs. A pixel size of the ALPIDE sensor is 27×29 μm^2 and a chip size is 15×30 mm^2, respectively. ALPIDE provides a digital output signal directly transmitted to a DAQ board. As shown in Fig. 1, 3 RPs were placed in each back and forth of DUT. RPs and DUT are equally spaced 25 mm between them. Two scintillators with a size of 10×15 mm^2 were located behind the 6th RP. A coincidence of the scintillators gives an event trigger.

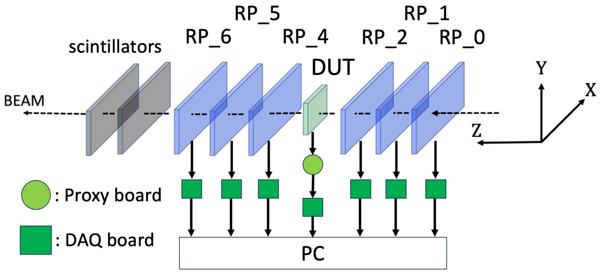

Figure 1: Telescope setup.

3. Analysis

First, alignment of positions for RPs and DUT has been performed. It is assumed that an electron trajectory is straight. The X(Y) axes of RP_1-5 are shifted to match the X(Y) axis of RP_0. Next, hit positions in neighboring RPs are connected by a straight line. A rotation correction of the X-Y plane and a fine adjustment of the X(Y) axis are done based on a fitted straight line. The positions for RPs are fixed at this step. Then, tracking by a straight line is made with the hit positions in RPs. DUT alignment is finally done based on the track obtained in the previous step. DUT rotation and X(Y) axis adjustment are done with respect to a trajectory of the track after correcting the shift of the X(Y) axis for DUT from RP_0.

In this analysis, two following criteria are defined for selection of the events in which an electron goes through the active area of DUT: (1) all RPs must have hits, (2) only one track is found in a given event. A hit position in each RP is calculated as $R=\sqrt{X^2+Y^2}$. Figure 2 shows the difference, ΔR, of a hit position from an expected hit position by the track. The ΔR distributions are shown by solid lines for RP_0 and RP_4, dashed lines for RP_1 and RP_5, and dotted lines for RP_2 and RP_6. Possible causes of different distributions are mis-alignment, multiple scatterings and individual difference of the RP response.

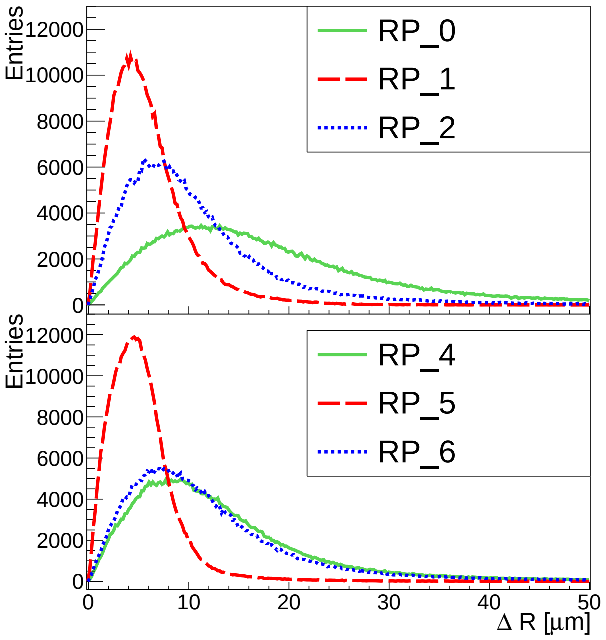

Figure 2: Distributions of the difference, ΔR, of a hit position from an expected hit position by the track for each RP.

In this Telescope setup, the scintillators are larger than the DUT. The ratio of geometrical acceptance coverages by DUT and the scintillators is about 0.0039%. Thus, the expected number of the DUT hit events is calculated by 432588 × 0.0039%∼1687, where 432588 is the number of recorded triggered events. Actually, the number of events in which a track is expected to penetrate the DUT is 1463. The cause of the difference from the expected value is under investigation.

After the event selection, clustering is performed with the following procedure. Firstly, the pixel with the highest amount of charge is searched and it is defined as a seed pixel. The neighboring pixels with the seed pixel are checked and they are included in a cluster if they have a hit. The hit position is defined as the center of gravity calculated from each pixel charge in the cluster. Then association of a cluster on DUT to the track is done by searching in a region within 100 μm from the track projected point.

Figure 3 shows the charge distribution of the track-associated clusters together with the pedestal. Normalization is done by the number of events. The close and open symbols represent the track-associated cluster and pedestal distributions, respectively. The cluster charge by energy deposit of the electron beam must be separated from the pedestal, but they look identical because fake clusters by noise may be dominant. The minimum charge for one pixel should be required to remove fake clusters.

Figure 4 shows the difference, ΔX, of a hit position from an expected hit position by the track. As described above, fake clusters make the distribution rather flat.

4. Summary & Outlooks

The 65 nm-CMOS MAPS sensors are under development for ALICE 3. Characterization of the prototype sensors has been done with the telescope setup at the KEK PF-AR beam line. Event selection was done to ensure that electrons penetrated the active region of the prototype sensor. However, looking at the charge distribution and the difference of a hit position from the track projected point for the track-associated clusters, fake clusters by noise may be dominant. Further efforts are needed to remove such fake clusters. The minimum charge and χ^2/ndf at tracking as a track quality can help.

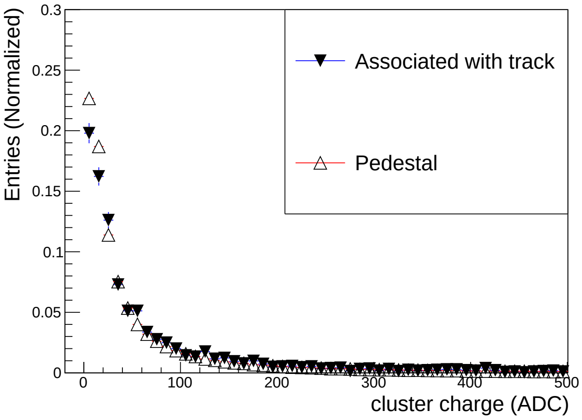

Figure 3: Comparison of the charge distribution of the track-associated clusters together with the pedestal.

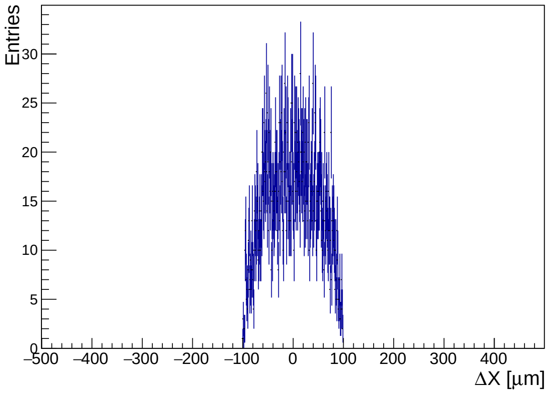

Figure 4: The difference, ΔX, of a hit position from an expected hit position by the track for DUT.

References

[1] ALICE Collaboration, arXiv:2211.02491v1 (2022) 12.

[2] G. Aglieri for ALICE Collaboration, Ncul. Instr. Meth A **845** (2017) 2.

[3] R. Ricci *et al.*, Ncul. Instr. Meth A. **A1059** (2024) 1.

Evaluation of OTS coating on AR coating by XPS

S. Kumahara, H. Nagahama[a], T. Nakashita[b, c], A. Hatakeyama[d], K. Asakawa[d], and Y. Sakemi[a]

Department of Applied Physics and Chemical Engineering, Tokyo University of Agriculture and Technology
[a]*Center for Nuclear Study, University of Tokyo*
[b]*The Institute of Physical and Chemical Research, RIKEN*
[c]*Graduate School of Arts and Sciences, University of Tokyo*
[d]*Department of Applied Physics, Tokyo University of Agriculture and Technology*

1. Introduction

Anti-relaxation coatings that prevent spin relaxation are often used in atomic physics such as magnetometers. It prevents the adsorption of atoms, so they also function as "anti-adsorption coatings".

In few-atom trap experiments, it is important that atoms are not adsorb on the inner wall of the trapping cell , which leads to the decrease of the number of atoms. Therefore, anti-adsorption coating is valuable to increase the number of trapped atoms.

Magneto-optical trap (MOT) is one of the trapping techniques that cools and gathers atoms to a point using laser cooling and magnetic gradient. The number of trapped atoms is calculated by measuring the fluorescence of trapped atoms. It is difficult to measure the fluorescence if there is scattered light of the laser from the trapping cell. We use the cell shown in Figure 1 to trap francium atoms. To subject the laser into the cell, there are glass windows. The light is scattered when passing through the windows. In order to prevent this, the windows are coated with "anti-reflection coating (AR coating)".

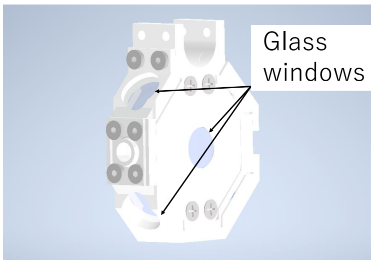

Figure 1: CAD image of MOT cell

The part of the cell except the windows is coated with anti-adsorption coating. In other words, the windows do not have anti-adsorption coatings, so that atoms to trap can decrease because they adsorb on the windows. Therefore, the both abilities of anti-reflection and anti-adsorption are required for the windows.

2. Purpose

Figure 2 shows a conceptual image of this study. We studied the coating that has both abilities of anti-reflection and anti-adsorption using the glass substrate coated with an anti-adsorption coating on an AR coating. We used octadecyltrichlorosilane (OTS: $C_{18}H_{37}SiCl_3$) as an anti-adsorption coating and magnesium fluoride (MgF_2) as an AR coating. In this study, we discussed the anti-reflection and anti-adsorption effect of the substrate.

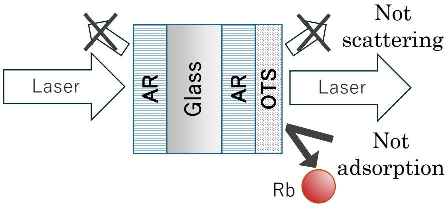

Figure 2: Image of this study

3. Experiment

We prepared 3 types of samples shown in Table 1. Cleaning with piranha solution, a 4:1 mixture of nitric acid and hydrogen peroxide is the process to remove organic contaminants on the surface. However, there was a possibility that the process takes off the AR coating, so we prepared sample 2 and 3.

sample number	OTS coating	Piranha cleaning
1	No	No
2	Yes	Yes
3	Yes	No

Table 1: Samples coated with OTS coating and Piranha cleaned or not: all samples coated with AR coating of MgF_2

Figure 3 shows a conceptual diagram of the apparatus used in this study. We measured the surface composition of the sample using X-ray photoelectron spectroscopy (XPS). Then, rubidium (Rb) atoms are subjected to the sample for arbitrary time (5-30 minutes). After that, we conduct the XPS measurement to check the Rb adsorption. We repeated the Rb irradiation and XPS measurement, and examined the amount of Rb on the samples.

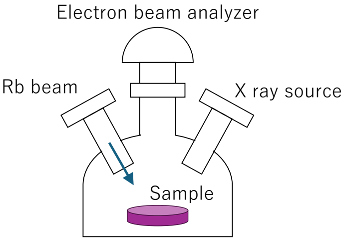

Figure 3: A conceptual diagram of the apparatus

4. Result and Discussion

Figure 4 shows the changes of the amount of Rb adsorption during the irradiation time: the amount of Rb adsorption is calculated from the peak area fitted Rb peak of XPS results shown in Figure 5. It means that sample 2 and 3 have the ability of anti-adsorption compared with sample 1 obviously. In addition, the plots are fitted with the formula $y = A(1-\exp\{(-t/\tau)\})$: y is the photoelectron counts, A is the proportionality coefficient, τ is the time constant, and t is time. The fitting means that the adsorption is becoming saturated.

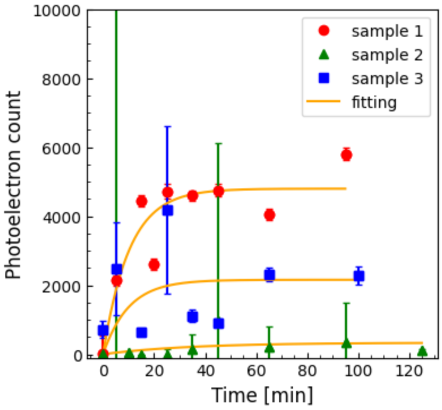

Figure 4: Change in adsorption versus time

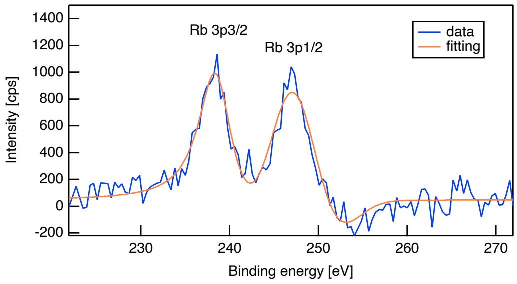

Figure 5: Energy spectrum near the peak of Rb and the result of the fitting, using the Rb 3p3/2 peak

It shows the peak area ratio of carbon and Magnesium C/Mg by the first XPS measurement in Table 2. It is regarded as which the sample 2 and 3 are coated with OTS because these ratios are greater than sample 1 one: the existence of C in sample 1 is considered by organic contaminants. In addition, the smaller sample 3 ratio compared with sample 2 one is regarded as that the coating rate of OTS of sample 3 is lower than sample 2 one. It can explain the difference between sample 2 and sample 3 in Figure 4.

sample number	C/Mg
1	0.63 ± 4
2	4.8 ± 4
3	4.1 ± 4

Table 2: Peak area of carbon divided by peak area of magnesium

Table 3 shows the optical attenuation rate measured by transmitted laser light. It means that the smaller the optical attenuation, the more light is transmitted, i.e., the less scattering. Sample 1 has the best optical attenuation and is effective in AR coating. Then, sample 2 and 3 get worse compared with sample 1. In particular, sample 2 has a large attenuation. This could be due to cleaning the surface coated with AR coating using piranha solution, causing peeling off the coating. Thus, the value of sample 3 that was not cleaned with piranha solution is not bad compared to that of sample 2.

sample number	Optical attenuation [%]
1	0.65
2	7.6
3	1.1

Table 3: Optical attenuation of samples

These results suggest that sample 3 which is coated with OTS without piranha cleaning on AR coating has the abilities of anti-reflection and anti-adsorption. On the other hand, there is a question about the process that OTS was coated on AR coating, not glass surface.

In general, the chlorine atoms in the end group of OTS react with OH groups on the glass surface and form HCl, breaking the bonds to the silicon atom of OTS. Then the silicon atom binds to the remaining oxygen atoms of the glass surface, forming chemisorption [1]. However, it is different that the process is coated with OTS on the AR coating of MgF_2. It is known that MgF_2 can make bonds with OH groups: OH groups bond to magnesium atoms of MgF_2, though not all magnesium atoms are bonded [2], [3]. Therefore, in this study, it is considered that magnesium atoms in the topmost surface layer of the MgF_2 multilayer are bonded to some OH groups, causing the bonding to OTS such as in the case of the bonding of glass and OTS.

5. Conclusion

We studied the performance of anti-reflection and anti-adsorption using the glass windows coated with OTS as anti-adsorption coating on MgF_2 as AR coating. As a result, OTS coating on AR coating without piranha cleaning process had the abilities because piranha solution did not peel off AR coating. It is considered that an oxygen atom mediates a silicon atom of OTS and magnesium of MgF_2.

References

[1] Scott Jeffrey Seltzer, “Developments in alkali-metal atomic magnetometry”, Princeton University, (2008)

[2] Hillary A. Prescott *et al.*, “New magnesium oxide fluorides with hydroxy groups as catalysts for Michael additions", J. Mater. Chem., **15**, 4616–4628 (2005)

[3] Jie Cen *et al.*, “Adsorption of Water Molecule on Calcium Fluoride and Magnesium Fluoride Surfaces: A Combined Theoretical and Experimental Study”, J. Phys. Chem. C, **124**, 7853-7859 (2020)

Laser and optical system for magneto-optical trapping of Fr atoms

K. Nakamura, S. Nagase[a], T. Nakashita[b, c], T. Aoki[b], H. Nagahama and Y. Sakemi

Center for Nuclear Study, Graduate School of Science, University of Tokyo
[a]*Department of Physics, University of Tokyo*
[b]*Graduate School of Arts and Sciences, University of Tokyo*
[c]*RIKEN (The Institute of Physical and Chemical Research)*

Francium (Fr), the heaviest alkali atom, is one of the most promising candidates for probing fundamental symmetry violations such as the permanent electric dipole moment (EDM) and atomic parity nonconservation (APNC) [1–3]. Our long-term goal is to realize ultra-precise EDM/APNC measurements using cold Fr atoms trapped in an optical lattice [4, 5]. To prepare the atoms for loading into the optical lattice, they must first be pre-cooled and trapped using methods such as magneto-optical trapping (MOT).

In this report, we present a laser and optical system developed at RIKEN for Fr MOT. Figure 1 shows a bird ’ s eye view of the RIKEN Nishina Center for Accelerator-Based Science. The laser source was located in the laser room (K2L), the ^{210}Fr MOT apparatus was located in the target room E7, and the ^{221}Fr MOT apparatus was located in the hot laboratory (HL). The ^{210}Fr isotope (half-life: 3.2 minutes [6]) is produced via the nuclear fusion-evaporation reaction $^{197}\mathrm{Au} + {}^{18}\mathrm{O} \rightarrow {}^{215-x}\mathrm{Fr} + x\mathrm{n}$ by bombarding a ^{197}Au target with an $^{18}\mathrm{O}^{6+}$ beam from the RIKEN AVF cyclotron [7]. Meanwhile, ^{221}Fr (4.8 minutes [6]) is produced by the alpha decay of ^{225}Ac (10.0 days [6]) [8]. Both isotopes exhibit a significant enhancement factor for electron EDM [5], and ^{221}Fr possesses an additional enhancement factor for nuclear EDM [9]. Therefore, the use of both isotopes is anticipated to yield diverse information. The laser beams initially traverse from K2L to the optical relay rack, which serves as the central hub for optical transmission, via a 400 m fiber-optic cable. In addition, the optical relay rack is linked to room E7 and room HL with 40 m and 55 m fiber cables, respectively. The direction of transmission can be altered using fiber connectors. Each of the three fiber cables consists of PVC-coated flexible stainless steel tubes “Picoflec” (Nippon Steel Welding Engineering) containing seven bare PM single-mode PANDA fibers (Fujikura): four are Fujikura PM63 (cutoff wavelength: 520-620 nm, mode field diameter: 4. 5 ± 0.5 μm at 630 nm), two are PM85 (650-800 nm, 5.5 ± 0.5 μm at 850 nm), and one is PM98 (870-950 nm, 6.6 ± 0.5 μm at 980 nm). The numerical aperture (NA) of each PM fiber is 0.12, and the connectors at both ends are FC/APC.

Figure 2 shows the laser and optical system developed at RIKEN. A Ti:sapphire (Ti:Sa) laser (M SQUARED LASERS, model SolsTiS, wavelength tunable in the 700-1000 nm range) was used as the trapping laser source for Fr. A home-made interference filter type external cavity diode laser (ECDL) [10] was used as the D1 repumping laser source for Fr. The trapping transitions for ^{210}Fr and ^{221}Fr are from $7\mathrm{S}_{1/2}$, $F = 13/2$ to $7\mathrm{P}_{3/2}$, $F = 15/2$ and from $7\mathrm{S}_{1/2}$, $F = 3$ to $7\mathrm{P}_{3/2}$, $F = 4$ on the D2 line (718

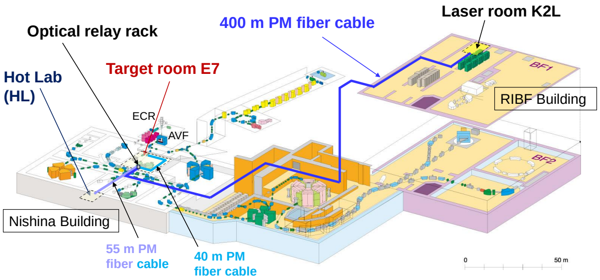

Figure 1: The path of the PM fiber cables we installed at the RIKEN Nishina Center for Accelerator-Based Science. The bird’s eye view diagram was provided by RIKEN.

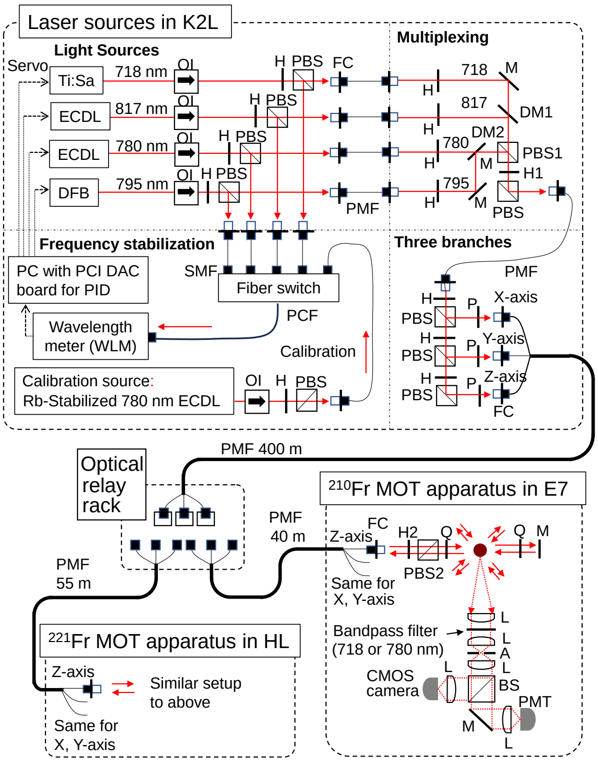

Figure 2: Schematic of the laser and optical system for Fr MOT at RIKEN. Key components include: OI - optical isolator, FC - fiber collimator, H - half-wave plate, Q - quarter-wave plate, P - polarizer, DM - dichroic mirror, M - mirror, L - lens, A - aperture, PMF - polarization-maintaining fiber, PCF - photonic crystal fiber, SMF - single-mode fiber.

nm), respectively; the repumping transitions are from $7S_{1/2}$, $F = 11/2$ to $7P_{1/2}$, $F = 13/2$ and from $7S_{1/2}$, $F = 2$ to $7P_{1/2}$, $F = 3$ on the D1 line (817 nm). In addition, a Littrow-type ECDL (780 nm) and a distributed feedback (DFB) laser source (795 nm) were used as trapping and repumping laser sources, respectively, for ^{87}Rb MOT. All laser sources were operated in CW mode.

The wavelength meter (WLM, HighFinesse, model WS8-2 Standard, wavelength range: 330 to 1180 nm), with an optional 8-channel fiber switch, can measure laser wavelengths while switching up to 8 optical inputs every few 10 ms. The laser frequency of up to seven laser beams can also be controlled simultaneously via the voltage output of the proportional-integral-derivative (PID) controller. One of the eight channels of the fiber switch serves as the optical input port of the calibration source. The WLM was calibrated every 10 min by another interference filter type ECDL (Rb stabilized laser) frequency stabilized by the modulation transfer method [11] to the D2 line (780 nm) of ^{87}Rb in the Rb vapor cell.

The Fr trapping and repumping laser beams were combined into a common beam path by the dichroic mirror DM1 and the Rb beam by DM2. These combined beams are referred to as MOT beams. The Fr and Rb MOT beams were orthogonally combined at the polarizing beam splitter PBS1. The Fr and Rb MOT beams can be interchanged by rotating the half-wave plate H1. The MOT beam was split into three paths using PBS and H and then directed into three PM fibers (Fujikura PM63). A linearly polarized MOT beam was aligned with the slow axis of the PM fiber and transmitted in a linearly polarized state. Polarization crosstalk components coupled to the fast axis were eliminated as unwanted polarization components by a PBS positioned in free space after exiting the fiber. A quarter-wave plate (Q) was placed in front of the input of the MOT apparatus to change the polarization state of the light to circular polarization. In the stable ^{87}Rb MOT experiment, an ^{87}Rb dispenser was placed directly under the MOT apparatus to provide ^{87}Rb atoms. The MOT apparatus consists of a metal vacuum chamber with an ICF34 glass viewing window through which a 16 mm diameter laser beam passes. The MOT beam was introduced from three axes, and the beam was reflected back by mirrors on the diagonal of each axis to create a three-dimensional MOT [12].

The transmission loss was measured at 718 nm for a 400 m PM fiber. Figure 3 shows the experimental setup. A WLM-stabilized Ti:Sa laser beam at 718 nm was used as the measurement source. Linearly polarized light aligned with the slow axis was coupled to the A-end of a 1 m PM fiber (Fujikura PM63), and the optical power at the B-end was measured to calculate the coupling efficiency of the light at the A-end, denoted as η_A. Subsequently, the fiber was temporarily connected at the D-end with a fiber connector to another installed 400 m PM fiber. A laser beam injected into this fiber from the room K2L side enabled the measurement of the optical power at the C-end and A-end, respectively. The coupling loss ξ_{BC} between the B and C-ends was determined from their ratio. Using η_A and ξ_{BC}, the input power (P_{in}) to the 400 m PM fiber was estimated. At a sufficiently low P_{in} to avoid stimulated Brillouin scattering (SBS) [13], the output power (P_{out}) of the 400 m PM fiber was measured at the D-end, and the transmission loss was calculated from the ratio of P_{in} to P_{out}, resulting in a transmission loss of -2.2 dB at 718 nm for the installed 400 m PM fiber. Typical values for η_A and ξ_{BC} were approximately -0.7 dB and -0.5 dB, respectively.

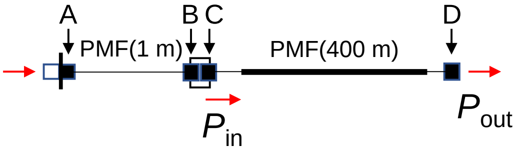

Figure 3: Schematic of transmission loss measurement of 400 m PM fiber.

The transmitted optical power of the 400 m fiber for the 718 nm laser beam was finally limited to 20 mW by SBS [14]. However, the power was sufficient to perform MOT with the current beam diameter of 16 mm. We have achieved Rb MOTs in both room E7 and room HL using the fiber-optic delivery systems. Experiments to achieve Fr MOT are being conducted intermittently and progress is being made toward this goal.

Acknowledgment

This experiment was performed at RI Beam Factory operated by RIKEN Nishina Center and CNS, The University of Tokyo. This work was supported by Japan Society for the Promotion of Science (19H05601, 20K14482, 22K18273, 23K03430) and Murata Science Foundation.

References

[1] J. S. M. Ginges *et al.*, Phys. Rep. **397** 63-154 (2004).
[2] N. Shitara *et al.*, JHEP **2021** 124 (2021).
[3] B. K. Sahoo *et al.*, Phys. Rev. A **92** 052511 (2015).
[4] Y. Sakemi *et al.*, AIP Conference Proceedings **2319** 080020 (2021).
[5] Y. Sakemi *et al.*, CNS Annual Report 2019, 31 (2021).
[6] National Nuclear Data Center, information extracted from the NuDat 2 database.
[7] N. Ozawa *et al.*, Rev. Sci. Instrum. **94** 023306 (2023).
[8] M. Sato *et al.*, RIKEN Accel. Prog. Rep. **55** 129 (2022).
[9] V. Spevak, *et al.*, Phys. Rev. C **56** 1357 (1997).
[10] X. Baillard, *et al.*, Opt. Commun. **266** 609-613 (2006).
[11] J. H. Shirley, Opt. Lett. **7**(11) 537–539 (1982).
[12] S. Nagase, *et al.*, CNS Annual Report 2021, 21 (2023).
[13] G. P. Agrawal, Nonlinear Fiber Optics,5th edition (Academic Press, 2013).
[14] K. Nakamura *et al.*, (to be submitted).

Machine learning-Aided Diagnostics for HyperECR Ion Source

K. Kamakura, Y. Morita[a], A. Kasagi[b], N. Oka[c], T. Nishi[a],
M. Nakagawa[d], Y. Kotaka, and Y. Sakemi

Center for Nuclear Study, Graduate School of Science, the University of Tokyo
[a]*Nishina Center for Accelerator-Based Science, RIKEN*
[b]*Graduate School of Artificial Intelligence and Science, Rikkyo University*
[c]*National Institute of Information and Communications Technology*
[d]*Cluster for Pioneering Research, RIKEN*

1. Introduction

CNS 14 GHz HyperECR ion source provides various metal ion beams to the RIKEN AVF cyclotron. It was built in the early 1990s and installed in the injection line of the RIKEN AVF cyclotron in 2004. More than thirty years of development led to high-intensity productions of various required beams [1]. However, long-term stable operations of the ion source still have difficulties, especially for metal beam productions. Recently, a novel control system aided by machine learning has been proposed to improve its stability.

2. Control Parameters

There are 6 parameters to control the ion source: RF power input, upstream and downstream mirror coil currents, main and support gas flow, and RF tuner position. When a metal beam is required, the main gas valve is closed and the RF tuner is replaced by a sample crucible or a sample rod, hence 5 parameters. After extraction, the beam is controlled by 6 parameters in the LEBT: einzel electrode voltage, quadrupole magnet current, and slit positions (top, bottom, left, right). Although acceleration voltage and analyzer magnet current also affect the beam property, their values are predetermined by the injection conditions of the AVF cyclotron.

Several values can be observed to diagnose the state of the ion source such as the reflected RF power, vacuum pressure of the extraction chamber, and the total drain current of the high-voltage power supply. Also, images inside the plasma chamber can be observed using a video camera through the extraction aperture.

Since there is no one-to-one relationship between control parameters and beam conditions, tuning a dozen parameters to optimize beam conditions is a complicated process. The optimization heavily relies on the experience of a few operators. For metal beams, the ionization process involves a state change from solid to gas. This further complicates the operation, and sometimes, stable production of the beam is interrupted.

3. Beam Intensity Prediction Model

Machine learning technologies have a huge potential to replace human experience-based knowledge for AI models. If the ion source tuning could be done automatically, it would greatly contribute to the reliability and reproducibility of the ion source operations.

When the ion source needs tuning, an operator observes the information listed in the previous section to determine the state of the ion source before changing the control parameters.

As a first step for the automatic control, we developed a beam intensity prediction model with a neural network model. It takes the control parameters, the observable values, and the plasma image as input, and predicts the beam intensity at that instance. Figure 1 shows the outline of the neural network model. ResNet50 is used to process plasma images. It is a convolutional neural network model pretrained with general images [2]. Outputs from the ResNet50 are fed into a fully connected layer and then combined with the numerical values. After two other fully connected layers, the output is set to a single value: the beam intensity.

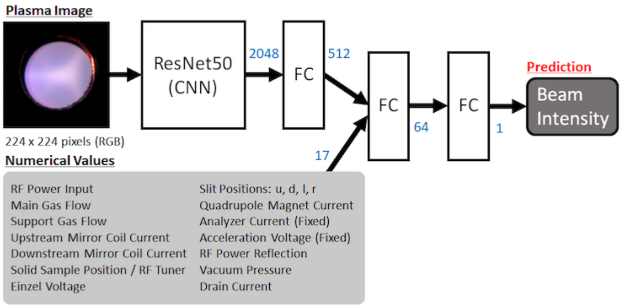

Figure 1: Outline of the beam current prediction model. ResNet50 takes 224×224 RGB images as input and characterizes the image in 2048 parameters. A fully connected layer (FC) compresses them down to 512. They are combined with 17 numerical values and fed into another layer. It returns 64 parameters. The final layer processes them and returns the beam intensity.

4. Model Evaluation

The model is evaluated using data acquired during tuning a $^{56}\mathrm{Fe}^{15+}$ beam. There are two sets of data. The first data is taken after a user experiment. The beam intensity was around 2 eμA at that time. An operator tuned the control parameters to raise it to around 6 eμA. Numerical data and plasma images were recorded for 13 minutes and 16 seconds with 4,900 data points during the tuning. Next, similar tuning was recreated for the second time. This time, the beam intensity was raised from around 2 eμA to 7 eμA. The second data was recorded for 18 minutes and 31 seconds with 6,850 data points. Since the second data set covers a wider range of beam intensity and has more data points, it was used to train the model. The first data set was used for validation. First, the model was trained with the second data using a mean square error as a loss function. As shown in Figure 2, the predicted beam intensity is close to the measured value. The deviation from the measured beam intensity is 0.033 eμA (RMS). Next, the trained model is validated by the first data. The result is shown in Figure 3. The prediction follows the measurement with the deviation of 0.94 eμA (RMS).

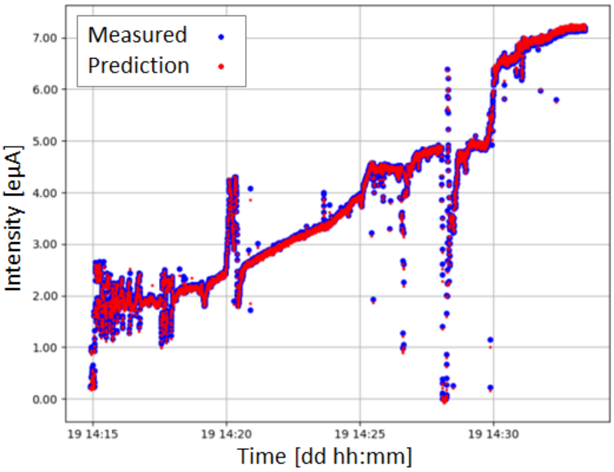

Figure 2: Training: Measured ^{56}Fe^{15+} beam intensity during the second tuning sequence (blue) used for training, and the predicted beam intensity (red) by the model trained by the same data.

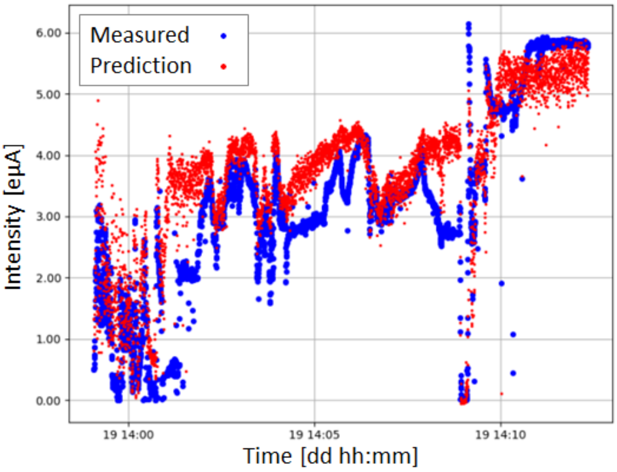

Figure 3: Validation: Measured ^{56}Fe^{15+} beam intensity during the first tuning sequence (blue), and the predicted beam intensity (red) by the model trained with the second tuning data.

5. Conclusion

The final goal is to establish a fully automated control system for the ECR ion source to deal with the instability issues. We have been using machine learning technology and implementing a neural network model to predict the beam intensity of the ECR ion source. It is performing well enough to follow the trend of the beam intensity. For now, it merely predicts the condition using the observable parameters and camera images to diagnose the condition of the beam. It will be a crucial part of the feedback control system that we are presenting.

References

[1] K. Kamakura *et al.*, CNS Annual Report 2020, 45-46 (2021).

[2] K. He *et al.*, Proceedings of the IEEE Conference on Computer Vision and Pattern Recognition, 770-778 (2016)

Current status of the development of the emittance monitor for high-intensity ion beams accelerated by AVF Cyclotron

Y. Kotaka, K. Kamakura, H. Yamaguchi, N. Imai, Y. Sakemi, and J. Ohnishi[a]

Center for Nuclear Study, Graduate School of Science, University of Tokyo
[a]*RIKEN Nishina Center*

1. Introduction

There are three experimental courses in the E7 room of RIKEN Nishina Center. On these courses, the experimental equipments of CNS are installed. Currently the beam transport efficiency at intensities larger than 10 eμA is limited and the overall average efficiency drops to 66% [1, 2]. We think these are caused by increasing beam emittance as the beam intensity is higher. Therefore, we are developing the pepper-pot emittance monitor (PEM) [3,4] capable of working at high beam intensities and aim at optimizing the beam transport system. In this fiscal year, we evaluated the precision required for PEM measurement, started beam tests to investigate the actual measurement error, and prepared a beam shutter system for PEM.

2. Required measurement error

We plan to optimize the beam transport system to decrease the beam loss and to achieve the beam size of 1 mm on EDM target by calculating the beam trajectory using the beam emittances measured by PEM as initial values. If the measurements errors of PEM are not negligible, we will not be able to calculate the real beam size on EDM target. Therefore, we must know the required PEM measurement errors and produce PEM deserving of it.

For this, we must know the typical emittance of the beam accelerated by AVF Cyclotron. We have measured many beam emittances by two-dimensional emittance monitor, but it was found that those measurements suffer from errors which cannot be studied quantitatively. Therefore, we estimate the emittance in another way.

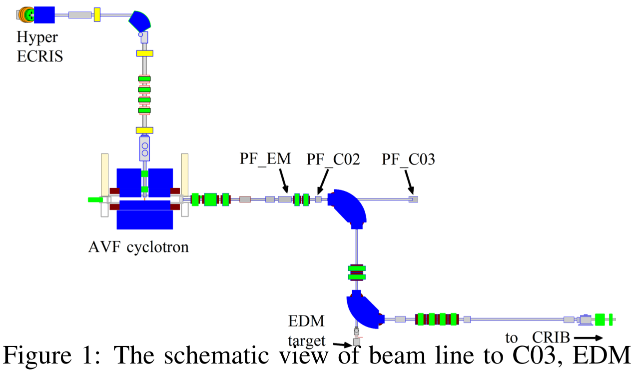

Figure 1: The schematic view of beam line to C03, EDM Target, and CRIB from AVF Cyclotron.

An beam emittance is calculated by using so-called σ matrix which is constituted by the variance of beam position, the variance of beam angle, and covariance between beam position and angle. The σ matrix can be calculated by using three measurements of Beam Profile Monitor (BPM) theoretically. We selected three BPMs of PF_C03, PF_C02, and PF_EM shown in Fig. 1, and irradiated them with $^{19}F^{7+}$ beam of energy 6.68 MeV/u and intensity 5 eμA. Beam distributions at each BPM are shown in Fig. 2. Here the horizontal and vertical directions perpendicular to beam direction are denoted as x and y (in mm), respectively. We regard the variances of x and y distributions as σ_{xx} and σ_{yy}, respectively. The ($\sqrt{\sigma_{xx}}$, $\sqrt{\sigma_{yy}}$) values measured by PF_C03, PF_C02, and PF_EM are (1.6, 1.3), (5.6, 4.8), and (7.1, 2.8) in mm, respectively. From these values, σ matrix is numerically obtained at 320 mm upstream of PF_EM, the candidate location of installing the PEM. We found a set of solution for the matrix elements in Eq. (1) by slightly changing the $\sqrt{\sigma_{xx}}$ value of PF_EM from 7.1 mm to 8.0 mm. We expect that this change of 0.9 mm is insignificant because it is very small compared with the full x-width of 40 mm at PF_EM and the beam distribution is left-right asymmetric. We assume Eq. (1) results from the error-free measurement because the position measurement error of BPM is thought to be 0.4 mm which is negligible compared with beam width.

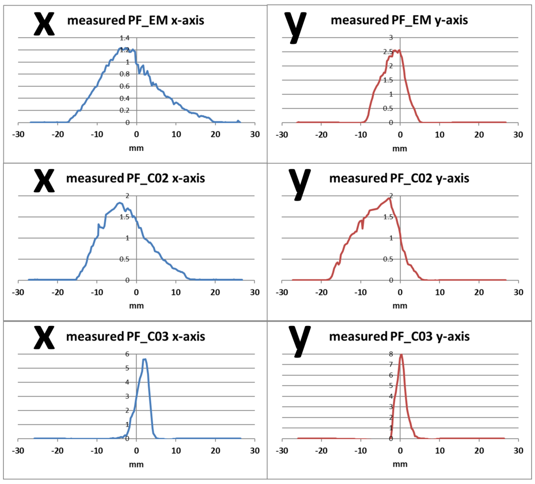

Figure 2: The beam distributions measured by BPMs. The top is PF_EM. The middle is PF_C02. The bottom is PF_C03.

$$\begin{pmatrix} \sigma_{xx} & \sigma_{xx'} & \sigma_{xy} & \sigma_{xy'} \\ \sigma_{x'x} & \sigma_{x'x'} & \sigma_{x'y} & \sigma_{x'y'} \\ \sigma_{yx} & \sigma_{yx'} & \sigma_{yy} & \sigma_{yy'} \\ \sigma_{y'x} & \sigma_{y'x'} & \sigma_{y'y} & \sigma_{y'y'} \end{pmatrix} = \begin{pmatrix} 28.1 & 44.6 & 0 & 0 \\ 44.6 & 72.0 & 0 & 0 \\ 0 & 0 & 7.9 & 1.3 \\ 0 & 0 & 1.3 & 0.6 \end{pmatrix} \tag{1}$$

Here x' and y' (in mrad) are the angles of x and y directions, respectively. The variances of x' and y' are denoted as $\sigma_{x'x'}$ and $\sigma_{y'y'}$, respectively, and the covariances between x and x' and between y and y' are $\sigma_{xx'}$ and $\sigma_{yy'}$, respectively. The other matrix elements in Eq. (1) is set to 0 as couplings between x and y are not apperared.

Defining the beam direction as z axis (mm), Fig. 3 is the envelope from the position of an emittance monitor (z = 0) to EDM target (z = 8120) calculated by TRANSPORT [5] applying Eq. (1) as initial values. The views of lower and upper half are envelopes for x and y axes, respectively. Though the last quadrupole magnets is currently doublet, a triplet quadrupole magnets is used in this simulation to obtain a good convergence of the beam at the EDM target. The momentum dispersion (dp/p) is 0.006 as an typical value.

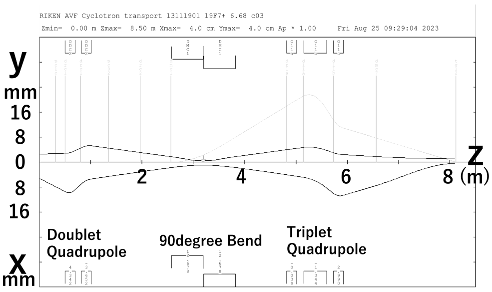

Figure 3: The beam envelopes applying Eq. (1) as initial values by TRANSPORT for $\sqrt{\sigma_{xx}}$ and $\sqrt{\sigma_{yy}}$ to be around 1 mm at the EDM target.

Next, we calculated the beam width at the EDM target as a function of angular error. Introducing four-variable (x, x', y, y') normal distribution having the elements of Eq. (1) as the initial values and adding arbitrary position and angluer errors statistically, we calculated $\sqrt{\sigma_{xx}}$ and $\sqrt{\sigma_{yy}}$ at the EDM target with the same parameter setting of the magnets. The relationship between $\sqrt{\sigma_{xx}}$ or $\sqrt{\sigma_{yy}}$ at the EDM target and the angular error is shown in Fig. 4. Since we regard Fig. 3 to be an error-free beam envelope, we used values of Fig. 3 when anglular error is 0. The required angular error of PEM is found to be less than 0.3 mrad [6].

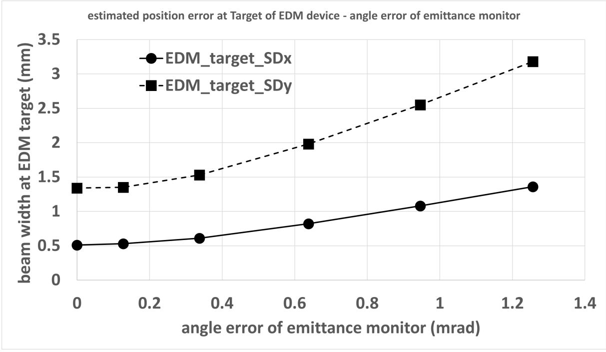

Figure 4: The relationship between angular errors (mrad) of an emittance monitor and the calculated SD of beam position distribution at the EDM target.

3. Beam test to see measuring error of PEM

We estimated the measurement errors based on the structure of PEM, but there might be unconsidered errors. Therefore, we plan to identify the measurement errors of PEM by beam tests. As we require low beam emittance, no correlation between x and y, and three BPMs in a beam line, we decided to test in Micro Analysis Laboratory, Tandem accelerator, The University of Tokyo [7]. The PEM installation with tele lens camera optics was complete. We performed the first beam test in February 2024.

4. Beam shutter system

The beam shutter system is the equipment produced to avoid heating of PEM due to beam irradiation of 400 W or more by shortening the irradiation time. The way is that the beam is rapidly bent away by applying a high voltage to the electrode just behind the ion source when the irradiation is sttoped. A high voltage of -2kV is supplied by Hamamatsu Photonics C9619 with a rise time of 0.15 seconds. Figure 5 shows the schematic diagram of the beam shutter system and the circuit to measure the transition time of output with oscilloscope. By this system, a beam exposure time of 0.27 seconds, which is between (3) and (5) in Fig. 6 of an oscilloscope display, has been achieved by now.

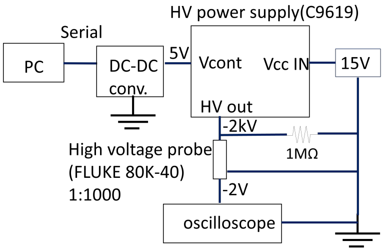

Figure 5: The schematic diagram of beam shutter system.

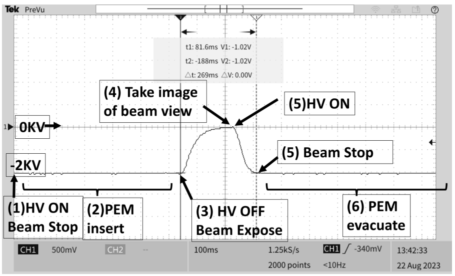

t1: 81.6ms V1: -1.02V
t2: -188ms V2: -1.02V
△t: 269ms △V: 0.00V

CH1 500mV CH2 -- 100ms 1.25kS/s 2000 points CH1 -340mV <10Hz 13:42:33 22 Aug 2023

Figure 6: The measured chopping time by oscilloscope.

References

[1] Y. Kotaka *et al.*, CNS Ann. Rep. 2020 (2022), p.43-44.

[2] Y. Kotaka *et al.*, Proc. 18th Annual Meeting of PASJ, (2021), p.873-877.

[3] L. E. Collins and P. T. Stroud, Nucl. Instr. and Meth. **26** (1964), p.157-166.

[4] T. Hoffmann *et al.*, AIP Conf. Proc. **546**, 432 (2000).

[5] D.C. Carey, K.L. Brown and F. Rothacker, FERMILAB-Pub-98/310.

[6] Y. Kotaka *et al.*, Proc. 12th IBIC2023, Saskatoon, Canada, (2024), p.339-342.

[7] https://malt.um.u-tokyo.ac.jp/

Theoretical Nuclear Physics

Calculation of pulse control for Cs Ramsey spectroscopy with two photon Raman resonance

M. Nakazawa, S. Nagase, K. Nakamura, and Y. Sakemi

Center for Nuclear Study, Graduate School of Science, University of Tokyo

Since the splitting of atomic Zeeman sublevels is typically within the MHz range, performing Ramsey spectroscopy directly between these states is challenging. However, by utilizing two photon Raman resonance, fully optical Ramsey spectroscopy can be achieved [1]. In this paper, the time development of Cs $^2\mathrm{S}_{1/2}$ - $^2\mathrm{P}_{1/2}$ Zeeman sublevels under Raman resonance is considered and a possible pulse control for Ramsey spectroscopy is proposed.

The calculation here supposes an experiment using laser cooled stable atom ^{133}Cs, which has a nuclear spin $I = 7/2$, with a weak magnetic field B being applied. The calculation is on the basis of hyperfine structure of the atom, corresponding to eigenstates of total spin operator $\hat{F} = \hat{J} + \hat{I}$, where $\hat{J}$ is the total angular momentum operator of electrons. The quantization axis is taken along the magnetic field.

We consider a situation electron is pumped to either of $^2\mathrm{S}_{1/2}, F = 3, m_F = -2, 0, 2$ state at time $t = 0$. It is enough to take $^2\mathrm{S}_{1/2}, F = 3$ and $^2\mathrm{P}_{1/2}, F = 3, 4$ manifold into account. The states are labelled

$$\begin{aligned}
\mathscr{G} &= \{|-3\rangle, |-2\rangle, \ldots, |3\rangle\} \quad \text{for} \quad {}^2\mathrm{S}_{1/2} F = 3, \\
\mathscr{E}_1 &= \{|-3'\rangle, |-2'\rangle, \ldots, |3'\rangle\} \quad \text{for} \quad {}^2\mathrm{P}_{1/2} F = 3, \\
\mathscr{E}_2 &= \{|-4''\rangle, |-3''\rangle, \ldots, |4''\rangle\} \quad \text{for} \quad {}^2\mathrm{P}_{1/2} F = 4,
\end{aligned}$$

each number in ket representing the magnetic quantum number m_F of its level. The energy eigenvalue of atomic Hamiltonian H_0 for $|n\rangle$ is denoted $\hbar\omega_n$, whereas the energy difference between $|n\rangle$ and $|m\rangle$ as ω_m^n. Zeeman shifts $\delta_{m_F}^\mathrm{Z}$ induced by the magnetic field are treated using Breit-Rabi formula, and the relative shifts $a = \delta_2^\mathrm{Z} - \delta_0^\mathrm{Z}$ and $b = \delta_{-2}^\mathrm{Z} - \delta_0^\mathrm{Z}$ are decomposed into the antisymmetric and symmetric components, as

$$\delta^{(1)} := (a - b)/2, \quad \delta^{(2)} := (a + b)/2.$$

To induce Raman coupling, two opposite circularly polarized lights are injected parallel to the magnetic field. The intensity and frequency of σ_+ and σ_- polarized light are denoted as (I_+, ω_+), (I_-, ω_-) respectively. The frequencies are set largely detuned from energy difference, as follows

$$\begin{aligned}
\mathit{\Delta}_{-3'} &= \omega_{-2}^{-3'} - \omega_- - d'_{-3} \\
\mathit{\Delta}_{-1'} &= \omega_{-2}^{-1'} - \omega_+ + d'_{-1} = \omega_0^{-1'} - \omega_- - d'_{-1} \\
\mathit{\Delta}_{1'} &= \omega_0^{1'} - \omega_+ + d'_1 \quad\;\; = \omega_2^{1'} - \omega_- - d'_1 \\
\mathit{\Delta}_{3'} &= \omega_2^{3'} - \omega_+ + d'_3 \qquad\quad (\text{same for } '').
\end{aligned}$$

Here six variables $\mathit{\Delta}_{-3'}, \mathit{\Delta}_{-1'}, \mathit{\Delta}_{1'}, \mathit{\Delta}_{3'}$, $d'_{-1} = -d'_{-3} = \frac{\delta'_{0,-2}}{2}, d'_1 = -d'_3 = \frac{\delta'_{0,2}}{2}$ are defined by six equations. Since $\mathit{\Delta}_*$ are set to be large, we can assume $\delta'_{0,-2} = \delta''_{0,-2} =: \delta_{0,-2}$ and $\delta'_{0,2} = \delta''_{0,2} =: \delta_{0,2}$. There exist relations

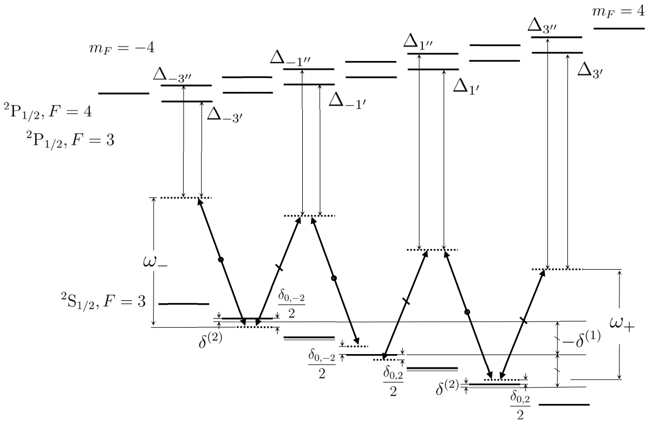

Figure 1: Energy levels and detunings Solid black lines: real energy levels, gray lines: energy levels ignoring symmetric component of Zeeman shift, dashed lines: imaginary levels.

$$\begin{aligned}
\delta_{0,2} &= \mathit{\Delta}\delta^{(1)} - \delta^{(2)}, \\
\delta_{0,-2} &= \mathit{\Delta}\delta^{(1)} + \delta^{(2)}, \qquad (1)
\end{aligned}$$

where $\mathit{\Delta}\delta^{(1)} = \omega_+ - \omega_- - \delta^{(1)}$. These detuning definitions are summarized in Figure 1.

The wave function and the Hamiltonian are expanded as

$$\begin{aligned}
|\Psi\rangle &= \sum_{n=-3}^{3} c_n(t)\,|n\rangle + \sum_{m=-3}^{3} c_{m'}(t)\,|m'\rangle + \sum_{l=-4}^{4} c_{l''}\,|l''\rangle, \\
H_0 &= \sum_{n=-3}^{3} \hbar\omega_n\,|n\rangle\langle n| + \sum_{m=-3}^{3} \hbar\omega_{m'}\,|m'\rangle\langle m'| \\
&\quad + \sum_{l=-4}^{4} \hbar\omega_{l''}\,|l''\rangle\langle l''|.
\end{aligned}$$

Although the full-quantum approach provides a simpler representation, here the interaction is handled semi-classically (electric field is not quantized). Electric field can be expanded on spherical basis as,

$$\boldsymbol{E} = \boldsymbol{\varepsilon}^+ E_+ e^{-\mathrm{i}(\omega_+ t + \xi_+)} + 0\boldsymbol{\varepsilon}^0 + \boldsymbol{\varepsilon}^- E_- e^{-\mathrm{i}(\omega_- t + \xi_-)}.$$

$E_\pm$ represents amplitudes of electric field, and are related to light intensities as

$$I_\pm \;[\mathrm{W/cm^2}] = \frac{1}{\mu_0} |\overline{\boldsymbol{E}_\pm \times \boldsymbol{B}_\pm}| = \frac{\varepsilon_0 c}{2} E_\pm^2,$$

where $\boldsymbol{B} = \boldsymbol{E}/c$ is magnetic field and the overline means taking the time average.

Then, the interaction Hamiltonian reads

$$\begin{aligned} H_{\mathrm{I}} &= \boldsymbol{d}\cdot\boldsymbol{E}(t) \\ &= \sum_{n=-3}^{3}\sum_{m'=-3}^{3} \left|m'\right\rangle \frac{K_{nm'}(t)}{2} \left\langle n\right| + \text{h.c.} \\ &\quad + (' \to '') \end{aligned}$$

where

$$\begin{aligned} K_{nm'}(t) &= \sum_{q\in\{+,-\}} \left\langle m' \middle| d_q \middle| n \right\rangle E_q\, e^{-\mathrm{i}(\omega_q t+\xi_q)} \\ &=: \sum_{q\in\{+,-\}} \Omega_{m'n}^{\tilde{q}}\, e^{-\mathrm{i}(\omega_q t+\xi_q)},\ \left(\tilde{q} = \left\{ \begin{smallmatrix} 1\ (q=+) \\ -1\ (q=-) \end{smallmatrix} \right.\right). \end{aligned}$$

By utilizing Wigner-Eckart theorem, the matrix element is calculated as follows [2].

$$\begin{aligned} &\left\langle m' \middle| d_q \middle| n \right\rangle \\ &= \left\langle \begin{smallmatrix} L'=1,S=\frac{1}{2}, \\ J'=\frac{1}{2},F'=3(4),m'_{\mathrm{F}} \end{smallmatrix} \middle| d_q \middle| \begin{smallmatrix} L=0,S=\frac{1}{2}, \\ J=\frac{1}{2},F=3,m_{\mathrm{F}} \end{smallmatrix} \right\rangle \\ &= (-1)^{F'-m'_{\mathrm{F}}} \left\langle \begin{smallmatrix} L'=1,S=\frac{1}{2}, \\ J'=\frac{1}{2},F' \end{smallmatrix} \middle\| \boldsymbol{d} \middle\| \begin{smallmatrix} L=0,S=\frac{1}{2}, \\ J=\frac{1}{2},F=3 \end{smallmatrix} \right\rangle \begin{pmatrix} F' & 1 & F \\ -m'_{\mathrm{F}} & \tilde{q} & m_{\mathrm{F}} \end{pmatrix} \\ &= (-1)^{J'+I+F+1+F'-m_{\mathrm{F}'}} \left\langle \begin{smallmatrix} J'=1/2 \\ L'=1 \end{smallmatrix} \middle\| \boldsymbol{d} \middle\| \begin{smallmatrix} J=1/2 \\ L=0 \end{smallmatrix} \right\rangle \\ &\quad \times \sqrt{(2F+1)(2F'+1)} \begin{Bmatrix} J' & F' & I \\ F & J & 1 \end{Bmatrix} \begin{pmatrix} F' & 1 & F \\ -m'_{\mathrm{F}} & \tilde{q} & m_{\mathrm{F}} \end{pmatrix} \end{aligned}$$

where

$$\begin{aligned} \left| \left\langle \begin{smallmatrix} J'=1/2 \\ L=1 \end{smallmatrix} \middle\| \boldsymbol{d} \middle\| \begin{smallmatrix} J=1/2 \\ L=0 \end{smallmatrix} \right\rangle \right|^2 &= \frac{1}{\tau}\cdot\frac{3\pi\varepsilon_0\hbar c^3}{\omega_0^3}\cdot(2J'+1) \\ &= 1.46\times10^{-57}\,\mathrm{C}^2\mathrm{m}^2 \end{aligned}$$

and $\tau = 34.791(90)\,\mathrm{ns}$ is the lifetime of $^2\mathrm{P}_{1/2} \to {}^2\mathrm{S}_{1/2}$, $\omega_0 = 2\pi\cdot 335.116\,\mathrm{THz}$ is its transition frequency [3, 4]. Since, when n, m' is specified, at most single element of $q \in \{+,-\}$ has nonzero value, from here on $\Omega_{nm'}$ is denoted without q index. The same logic holds for n and l''.

By considering Schrödinger equation, the time development of a wavefunction is

$$\begin{cases} \mathrm{i}\partial_t c_n(t) = \ \omega_n c_n(t) & + \dfrac{\Omega_{n,n-1'}}{2\hbar} e^{\mathrm{i}(\omega_- t+\xi_-)} c_{n-1'}(t) \\ & + \dfrac{\Omega_{n,n+1'}}{2\hbar} e^{\mathrm{i}(\omega_+ t+\xi_+)} c_{n+1'}(t) \\ & + (m' \to l''), \\ \mathrm{i}\partial_t c_{m'}(t) = \omega_{m'} c_{m'}(t) & + \dfrac{\Omega_{m',m-1}}{2\hbar} e^{-\mathrm{i}(\omega_+ t+\xi_+)} c_{m-1}(t) \\ & + \dfrac{\Omega_{m',m+1}}{2\hbar} e^{-\mathrm{i}(\omega_- t+\xi_-)} c_{m+1}(t), \\ (\text{same for } c_{l''}(t)). \end{cases}$$

First, define the coefficients

$$\begin{aligned} c'_n(t) &:= c_n(t) e^{\mathrm{i}\omega_n t} \\ c'_{m'}(t) &:= c_{m'}(t) e^{\mathrm{i}(\omega_{m'}-\Delta_{m'})t} \end{aligned}$$

to go to the rotating frame. The time development equations are simplified to

$$\begin{cases} \mathrm{i}\partial_t c'_n(t) = \dfrac{\Omega_{n,n-1'}}{2\hbar} e^{\mathrm{i}(\xi_- - d_{n-1'}t)} c'_{n-1'}(t) \\ \qquad + \dfrac{\Omega_{n,n+1'}}{2\hbar} e^{\mathrm{i}(\xi_+ + d_{n+1'}t)} c'_{n+1'}(t) \\ \qquad + (' \to '') \\ \mathrm{i}\partial_t c'_{m'}(t) - \Delta_{m'} c'_{m'}(t) = \dfrac{\Omega_{m',m-1}}{2\hbar} e^{-\mathrm{i}(\xi_+ + d_{m'}t)} c'_{m-1}(t) \\ \qquad + \dfrac{\Omega_{m',m+1}}{2\hbar} e^{-\mathrm{i}(\xi_- - d_{m'}t)} c'_{m+1}(t) \\ (\text{same for } c_{l''}(t)). \end{cases}$$

By adopting adiabatic elimination ($\partial_t c'_{m'}(t) \sim 0$), the time development of $^2\mathrm{S}_{1/2}$ states is described as

$$i\partial_t c'_n(t) = \frac{1}{4\hbar^2} \left[\begin{aligned} & \frac{\Omega_{n,n-1'}\Omega_{n-1',n-2}}{\Delta_{n-1'}} e^{-\mathrm{i}(\xi_\Delta+2d_{n-1'}t)} c'_{n-2}(t) \\ & + \left(\frac{\left|\Omega_{n,n-1'}\right|^2}{\Delta_{n-1'}} + \frac{\left|\Omega_{n,n+1'}\right|^2}{\Delta_{n+1'}} \right) c'_n(t) \\ & + \frac{\Omega_{n,n+1'}\Omega_{n+1',n+2}}{\Delta_{n+1'}} e^{\mathrm{i}(\xi_\Delta+2d_{n+1'}t)} c'_{n+2}(t) \\ & + (' \to '') \end{aligned} \right].$$

where $\xi_\Delta = \xi_+ - \xi_-$.
Finally, defining

$$\begin{aligned} c''_{-2}(t) &= e^{-\mathrm{i}\delta_{0,-2}t} c'_{-2}(t), \\ c''_2(t) &= e^{\mathrm{i}\delta_{0,2}t} c'_2(t), \end{aligned}$$

one can write effective Hamiltonian for equation $\mathrm{i}\partial_t \boldsymbol{c}(t) = H_{\mathrm{eff}}\boldsymbol{c}(t)$ where $\boldsymbol{c}(t) = \left(c''_2(t), c'_0(t), c''_{-2}(t)\right)^\top$,

$$H_{\mathrm{eff}} = \begin{pmatrix} \chi_2^1+\chi_2^3-\Delta\delta^{(1)}+\delta^{(2)} & \eta_{0,2}^1 e^{-\mathrm{i}\xi_\Delta} & 0 \\ \eta_{0,2}^1 e^{\mathrm{i}\xi_\Delta} & \chi_0^1+\chi_0^{-1} & \eta_{-2,0}^{-1} e^{-\mathrm{i}\xi_\Delta} \\ 0 & \eta_{-2,0}^{-1} e^{\mathrm{i}\xi_\Delta} & \chi_{-2}^{-1}+\chi_{-2}^{-3}+\Delta\delta^{(1)}+\delta^{(2)} \end{pmatrix}.$$

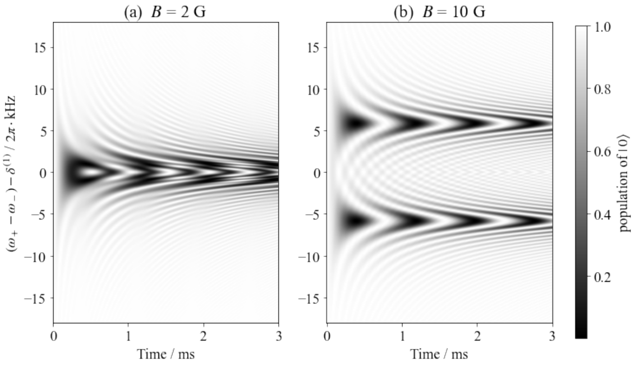

Figure 2: The dependence of $C_0(t)$ on $\omega_+ - \omega_-$ when megnetic field $B = 2\,\mathrm{G}$ ($\delta^{(1)} = 1.40\,\mathrm{MHz}, \delta^{(2)} = 213\,\mathrm{Hz}$) and $10\,\mathrm{G}$ ($\delta^{(1)} = 7.01\,\mathrm{MHz}, \delta^{(2)} = 5.33\,\mathrm{kHz}$).

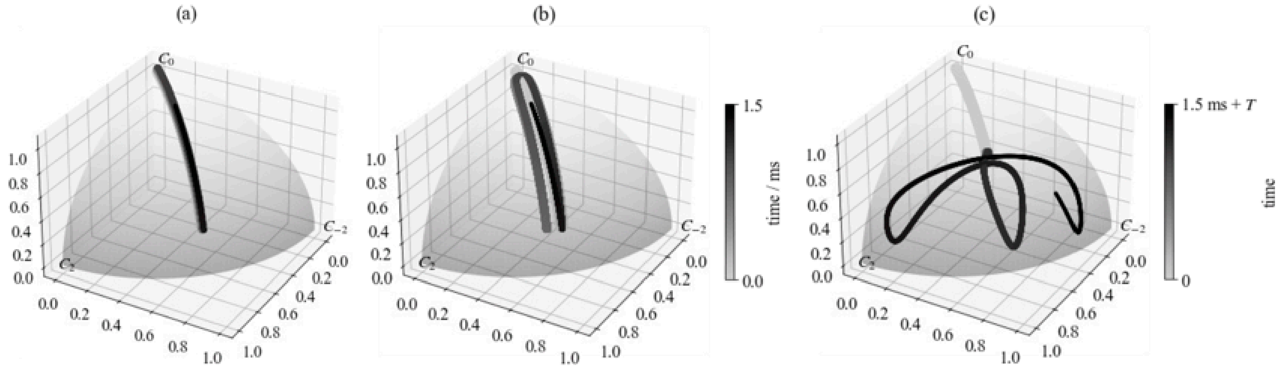

Figure 3: Dynamics of $C_2(t), C_0(t), C_{-2}(t)$. (a), (b): lights of $I_+ = I_- = 1.0\,\mathrm{mW/cm^2}$ are continuously injected. (c): lights of the same intensity are injected only when $t < \tau$ and $\tau + T < t$ under the condition of (2). Detunings are set as (a) $\Delta\delta^{(1)} = 0$, $B = 2\,\mathrm{G}$, (b) $\Delta\delta^{(1)} = 50\,\mathrm{Hz}$, $B = 2\,\mathrm{G}$, (c) $\Delta\delta^{(1)} = 50\,\mathrm{Hz}$, $B = 2\,\mathrm{G}$.

where

$$\eta^n_{m,l} = \frac{\Omega_{m,n'}\Omega_{n',l}}{4\hbar^2\Delta_{n'}} + ('\to''),$$

$$\chi^m_n = \frac{\left|\Omega_{n,m'}\right|^2}{4\hbar^2\Delta_{m'}} + ('\to''),$$

and used (1).

By solving eigenvalue problem of H_{eff}, we can determine the time development of $\{|-2\rangle, |0\rangle, |2\rangle\}$ system, and establish the pulse control for Ramsey spectroscopy. The following scheme is assumed for the calculation: initially, the atom is prepared in the $|0\rangle$ state, i.e., $\boldsymbol{c}(0) = (0,1,0)^\top$. Two circularly polarized light fields are then applied until $t = \tau$. Afterward, the lights are switched off for a duration T, and finally, they are reapplied for a time τ.

First, we consider a case that from $t = 0$, two polarized lights of intensity $I_+ = I_- = 1.0\,\mathrm{mW/cm^2}$ are continuously injected. At this light intensity, the light shifts (represented by η and χ in H_{eff} matrix) are within kHz range, which means population shifts occur at ms scale. In the following discussion, $\Delta = -1\,\mathrm{GHz}$.

When $\delta^{(2)}$ is much larger than light shifts, it is possible to distinguish two different population evolutions between $|2\rangle \leftrightarrow |0\rangle$ and $|0\rangle \leftrightarrow |-2\rangle$ (Figure 2 (b)). However, When $\delta^{(2)}$ is smaller than or comparable to the light shifts $\sim$ kHz, we have to treat the time evolution of the three level mixing (Figure 2 (a)). To intuitively understand the evolution, the quantum state dynamics is visualized in Figure 3 [5]. When $\delta = 0$, the state comes back to the initial one periodicaly, while when $\delta \neq 0$ the path is dissipated.

We examine Ramsey spectroscopy where $\delta^{(2)} \sim$ light shift. Here, τ, T are chosen as the time at which the population transition reaches its maximum when $\omega_+ - \omega_- = \delta^{(1)}$, and we have to be careful that, different from qubit case, even when $\Delta\delta = 0$ time evolution is not a simple Rabi oscillation for nonzero T, because of unignorable energy shift. One example is

$$\tau = 0.132\,\mathrm{ms}, \quad T = 4.17\,\mathrm{ms}, \tag{2}$$

at which parameter the expected Ramsey spectrum is represented in Figure 4. The state dynamics under this condition is drawn in Figure 3 (c), and by comparing it to (a), we observe the path dissipation is larger than (b) to (a), which means the sensitivity to $\omega_+ - \omega_-$ is enhanced compared to $T = 0$ case.

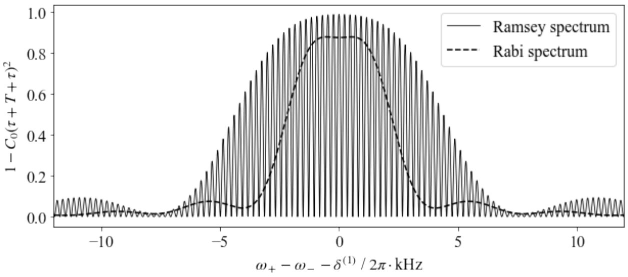

Figure 4: Example of possible Ramsey spectrum. $C_0(\tau + T + \tau)$ is plotted when lights are injected $t < \tau$ and $\tau + T < t < \tau + T + \tau$ under the magnetic field of $2\,\mathrm{G}$. Ramsey spectrum: T, τ follows the values of (2), Rabi spectrum: $T = 0$ while τ follows (2).

References

[1] K. C. Wright, L. S. Leslie, and N. P. Bigelow: Phys. Rev. A **78** (2008) 053412.

[2] M. Auzinsh, D. Budker, and S. Rochester: *Optically Polarized Atoms: Understanding Light-atom Interactions* (OUP Oxford, 2010).

[3] D. A. Steck: Quantum and Atom Optics, revision 0.14, 23 August 2023, available at http://steck.us/teaching .

[4] D. A. Steck: Cesium D Line Data, revision 2.3.3, 28 May 2024, available at http://steck.us/alkalidata .

[5] Festenstein, Max Z: An Intuitive Visualisation Method for Arbitrary Qutrit (Three Level) States, arXiv preprint arXiv:2304.01741 (2023).

Other Activities

The 22th CNS International Summer School CNSSS23

N. Aoi[a], T. Gunji, N. Imai, H. Liang[b,c], S. Michimasa, H. Nagahama, T. Otsuka[b], H. Sakai[b], Y. Sakemi, H. Sakurai[b,c], N. Shimizu, S. Shimoura, H. Ueno[b], T. Uesaka[b], Y. Utsuno[d], T. Wakasa[e], K. Yako, H. Yamaguchi, K. Yoneda

Center for Nuclear Study, Graduate School of Science, University of Tokyo
[a]*RCNP, Osaka University*
[b]*RIKEN Nishina Center*
[c]*Department of Physics, Univ. of Tokyo*
[d]*Advanced Science Research Center, Japan Atomic Energy Agency*
[e]*Department of Physics, Kyushu University*

The 22nd CNS International Summer School (CNSSS23) was organized by the Center for Nuclear Study (CNS) and held from August 4 to 10, 2023. The school was co-hosted by the JSPS A3-Foresight Program, the Super Heavy Element Center (RCSHE), and the Center for Accelerator and Beam Applied Science (CABAS) at Kyushu University. It was supported by the RIKEN Nishina Center and conducted in cooperation with the Asian Nuclear Physics Association (ANPhA).

The aim of the school was to provide graduate students and postdoctoral researchers with foundational knowledge and a broad perspective on nuclear physics. Further details about the school can be found on its web.

This year ' s school was held fully in person for the first time since 2019. Due to the COVID-19 pandemic, the schools in 2020 and 2021 were conducted online. In 2022, although the school resumed in-person sessions, students from Asian countries were unable to attend in person because of COVID-related restrictions imposed by the Japanese government.

The primary venue for this year's school was the Nishina Hall at RIKEN. On the second day, sessions were held at the Koshiba Hall on the Hongo Campus of the University of Tokyo. Additionally, a tour of the RIBF facility was conducted on the first day.

The school began with a welcome address by Prof. Shin'ichi Ohgoshi, Dean of the School of Science at the University of Tokyo. The program included lectures by leading scientists specializing in both experimental and theoretical nuclear physics. Each lecture started with a foundational overview and concluded with discussions on the latest advancements in the respective fields.

The list of the lecturers and the title of lectures are following:

- Prof. Hiroyuki Takahashi (Univ. of Tokyo, Japan), "Radiation detector, quantum sensing and its medical applications"
- Prof. Umesh Garg (Univ. of Notre Dame, USA), "Equation of state of the nuclear matter"
- Dr. Takayuki Miyagi (TU Darmstadt, Germany), "Ab-initio calculation"
- Dr. Marco Rosenbusch (RNC) "The RIBF Facility: A brief overview for newcomers", "High-precision mass measurements at low ion energies: Penning traps and multi-reflection devices"
- Dr. Nodoka Yamanaka (Nagoya Univ.), "Fundamental physics with atomic nucleus"
- Prof. Nobuaki Imai (CNS, Univ. of Tokyo, Japan), "Direct reaction and r-process nucleosynthesis"
- Prof. Yuji Yamazaki (Kobe University) "Partonic structure of hadrons through DIS and physics at the EIC"

Figure 1: A group photos of the participants of A3F-CNSSS23 with the lecturers.

Eight lecturers and eighty-seven participants registered for the school, including five from Korea, five from India, and one from Vietnam. Figure 1 is a group photo of the participants with the lecturers.

As per tradition, the program included three "Young Scientist Sessions," where graduate students and postdoctoral researchers delivered oral presentations. In total, twenty-two presentations were given. Since 2017, the CNSSS Young Scientist Awards (CNSSSYS Awards) have been established to honor exceptional presentations. A select number of winners were chosen from each session by members of the organizing committee and the lecturers. The recipients of the third CNSSSYS Awards were:

- CNS award winners (oral)
  - XiaoXu Dong(Beihang Univ. and Univ. of Tokyo) "High precision calculations of nuclear charge radii using Bayesian neural networks"

  - Yixin Guo (Univ. of Tokyo)“Cooper quartet correlations in infinite symmetric nuclear matter”
  - Vishal Malik (Tata Institute) “High spin spectroscopy of nuclei near A 90”

- CNS award winners (poster)
  - Jiatai Li (CNS, Univ. of Tokyo) “Development of a mosaic type array formed by Si photodiodes for charged-particle detection in heavy ion collisions”
  - Mirai Fukase (CNS, Univ. of Tokyo) “Development of a Radio Frequency Dipole Mass Filter for the Francium Permanent Electric Dipole Moment Search”
  - Shintaro Nagase (CNS, Univ. of Tokyo) “Development of a novel comagnetometer for high-precision measurement of the electron’s electric dipole moment using laser-cooled Fr atoms”

The certificate of the awards were presented to them from the school master, Prof. Sakemi.

The top presenter, Mr. Yixin Go, was also awarded the AAPPS-DNP/ANPhA Prize for Young Physicists, sponsored by AAPPS-DNP/ANPhA. He received a certificate and prize money, which were presented by Prof. W. Liu, the Chair of ANPhA.

We sincerely thank ANPhA for their support. Our gratitude also extends to the administrative staff of CNS for their invaluable assistance. We greatly appreciate the dedication of the graduate students and postdoctoral researchers at CNS for their hard work. Finally, we acknowledge the significant contributions of all the lecturers and participants, which ensured the success of A3F-CNSSS23.

Laboratory Exercise for Undergraduate Students

N. Kitamura, S. Nagao[a], K. Yako, S. N. Nakamura[a], K. Okawa, S. Nagase, K. Nishi[a], K. Nishida[a], S. Michimasa, N. Imai, Y. Yamaguchi, and H. Sakemi

Center for Nuclear Study, Graduate School of Science, University of Tokyo
[a]*Department of Physics, University of Tokyo*

Nuclear scattering experiments were performed as a laboratory exercise for undergraduate students of the University of Tokyo. This program was aiming at providing undergraduate students with an opportunity to learn how to study subatomic physics by using an ion beam from an accelerator. In 2023, 32 students attended this program.

Four beam times were scheduled in the second semester for third-year students, and 8 students participated in each beam time. The experiments were performed at the RIBF using a 26-MeV alpha beam accelerated by the AVF cyclotron. The alpha beam extracted from the AVF cyclotron was transported to the E7B beam line in the E7 experimental hall. The scattering chamber has two separate target ports which enable us to perform two independent experiments without opening the chamber during the beam time. In each beam time, the students were divided into two groups and took one of the following two subjects:

1. Measurement of elastic scattering of incident alpha particle with ^{197}Au, to learn how to determine nuclear size.
2. Measurement of gamma rays emitted from the cascade decay of highly excited ^{154}Gd and ^{184}Os, to learn the nuclear deformation.

Before the experiment, the students took a course on the basic handling of the semiconductor detectors and electronic circuits at the Hongo campus, and attended a radiation safety lecture at RIKEN. CNS conducted tours to the RI beam factory for the students.

In the α+^{197}Au measurement, α particles scattered with the Au target with a thickness of 1 μm were detected using a silicon PIN-diode located 15-cm away from the target. A collimator with a diameter of 6 mm was attached on the silicon detector. The energy spectrum of the scattered α particles was recorded by a multi-channel analyzer (MCA) system. The beam was stopped by a Faraday cup located downstream of the scattering chamber. The cross section for the alpha elastic scattering was measured in the angular range of $\theta_{\rm lab} = 20-150^\circ$.

The measured cross section was compared with the calculated cross section of the Rutherford scattering. The cross section was also analyzed by the potential model calculation, and the radius of the ^{197}Au nucleus was discussed. Some students obtained the radius of $\sim$10 fm by using a classical model where the trajectory of the α particle in the nuclear potential is obtained using the Runge-Kutta method.

In the measurement of gamma rays, excited states in ^{154}Gd and ^{184}Os nuclei were populated by the ^{152}Sm(α,2n) and ^{182}W(α,2n) reactions, respectively. The gamma rays emitted from the cascade decay of the rotational bands were measured by a high-purity germanium detector located 30-cm away from the target. The energy of the gamma ray were recorded by the MCA system. The gain and the efficiency of the detector system had been calibrated using standard gamma-ray sources of ^{60}Co, ^{133}Ba, and ^{137}Cs. The gamma rays from the 10^+ and 8^+ states in ^{154}Gd and ^{184}Os, respectively, were successfully identified. Based on the energies of the gamma rays, the moment of inertia and the deformation parameters of the excited states were discussed by using a classical rigid rotor model and a irrotational fluid model. The students found that the reality lies between the two extreme models. The initial population among the levels in the rotational band was also discussed by taking the effect of the internal conversion into account.

It was the first time for most of the students to use large experimental equipments. They learned basic things about the experimental nuclear physics and how to extract physics from the data. We believe this program was very impressive for the students. The authors would like to thank Dr. K. Tanaka, the CNS accelerator group, and the RIBF cyclotron crew for their helpful effort in the present program.

On the 1st IReNA-Ukakuren Joint Workshop "Advancing Professional Development in Nuclear Astrophysics and Beyond"

S. Hayakawa[a], C. Ishizuka[b], T. Chillery[a,c], A. Dohi[d,e], N. Fukagawa[f], T. Hatsuda[g], S. Iimura[h], M. Ishigaki[i], T. Isobe[j], K. Mori[f], N. Nishimura[a,e], K. Otsuki[k], R. Sawada[l], S. Yoshida[m], and T. Kawabata[n]

[a]*Center for Nuclear Study, Graduate School of Science, the University of Tokyo*
[b]*Institute of Innovative Research, Tokyo Institute of Technology*
[c]*Laboratori Nazionali del Gran Sasso, Istituto Nazionale di Fisica Nucleare*
[d]*Graduate School of Advanced Science and Engineering, Hiroshima University*
[e]*RIKEN Astrophysical Big Bang Laboratory*
[f]*Division of Science, National Astronomical Observatory of Japan*
[g]*RIKEN iTHEMS*
[h]*Department of Physics, Rikkyo University*
[i]*Subaru Telescope, National Astronomical Observatory of Japan*
[j]*RIKEN Nishina Center*
[k]*Department of Physics, Fukuoka University*
[l]*Graduate School of Arts and Sciences, the University of Tokyo*
[m]*Department of Data Science and Management, Utsunomiya University*
[n]*Department of Physics, Osaka University*

The 1st IReNA-Ukakuren Joint Workshop "Advancing Professional Development in Nuclear Astrophysics and Beyond" [1] took place on site between August 28th and September 1st, 2023 on the Mitaka Campus of National Astronomical Observatory of Japan (NAOJ). This was the first attempt at promoting exchange of human resources between Japan Forum of Nuclear Astrophysics (JaFNA or Ukakuren [2]) and International Research Network for Nuclear Astrophysics (IReNA [3]) of the United States of America (US), with a core emphasis on professional development of young scientists under the support of IReNA Focus Area 8 (FA8): Professional Development and Broadening Participation. This workshop was jointly hosted by IReNA, Ukakuren and also several Ukakuren partners including Center for Nuclear Study, the University of Tokyo (CNS), NAOJ, Research Center for Nuclear Physics, Osaka University (RCNP) and RIKEN iTHEMS. The organizing committee mainly consisted of voluntary young researchers from the Ukakuren network as their names in the authors list above, chaired by C. Ishizuka who is also one of the IReNA FA8 coordinators.

The workshop covered a wide range of research topics in nuclear astrophysics:

- Nuclear Equation of State
- Nuclear structures and reactions for astrophysics
- Stellar evolution, explosive phenomena, and nucleosynthesis
- The early Universe: Big Bang nucleosynthesis and metal-poor stars
- Chemical evolution of star clusters and galaxies
- New facilities and experimental techniques
- Neutrino and particle physics
- Recent hot topics and others

Table 1: Participants breakdown.

Japan		US		Others		Total	
58		9		2		69	
M	F	M	F	M	F	M	F
49	9	4	5	2	0	55	14
Faculty		Post Docs		Grad. Stu.		Total	
20		15		34		69	
M	F	M	F	M	F	M	F
14	6	12	3	29	5	55	14

and we invited relevant speakers considering balances of experimentalists or theorists, nuclear physicists or astrophysicists, Japan- or US-based researchers, and also genders. There were 69 participants in total, mainly from Japan and the US, and neighboring countries (a group photo in Fig. 1). Its breakdown is shown in Table 1 in terms of the countries and positions of the participants. The characters M and the F therein stand for male and female participants, respectively. Although the invited speakers were mostly balanced, there were still gaps between the numbers of the Japan- and

Figure 1: Group photo of the workshop.

US-based participants, and also genders especially in the Japan-based participants.

We arranged multiple invited talks in each research topic and contributed talks for the five-day long workshop in a large seminar room. We secured 40 and 30 minutes for the invited and contributed talks, respectively, which consequently provided sufficient time for detailed talks and active discussion. The workshop also provided several characteristic events: (1) Welcome Dinner on the first-day's evening: Arranged in the session room in stand-up buffet style for active intercommunion between the Japan- and US-based participants. (2) Mentor lunch and Career Development Session on the third day: One of the main purposes of the workshop was to assist career developments of next-generation researchers. Three mentors were invited from the IReNA network: Dr. Ana Becerril-Reyes (Michigan State University), Prof. Alfredo Estrade (Central Michigan University), and Prof. Anna Frebel (Massachusetts Institute of Technology, unfortunately not able to come for a personal reason). In the mentoring lunch, participants had lunch boxes together with the mentors, and sat around for free discussion. In the subsequent afternoon session, the mentors provided talks about professional development in academia occasionally mentioning their own careers paths and experiences. (3) Unconference on the fourth day — a participant-driven meeting: Participants proposed several agendas (Fig. 2) during the workshop period, and in the session time they separated into groups of their interests for free discussions on the agendas. At the end, summary of the discussions were briefly presented by each session leader. Such a freestyle session is not quite common in Japan, but basically went well actively with a little assistance by the organizers. (4) Poster Session on the fourth day: 15 contributions in total. Each presenter gave a 5-minute oral presentation to briefly introduce their poster in advance of the main poster session. We had active discussions in the 50-minute main session in a open space in front of the large seminar room with some beverages and snacks. The organizers scored each poster, and selected winners of the poster session:

- Kosuke Sakanashi (Osaka University),
- Mackenzie Smith (Michigan State University/FRIB),
- Yugo Motogami (Saitama University),
- Kurumi Furutsuka (University of Hyogo).

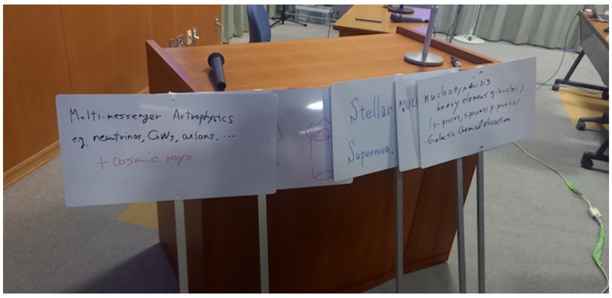

Figure 2: Part of agendas of the unconference written on placards.

Figure 3: Poster of the workshop.

In summary, we think that the workshop was basically successful, covering most of recent research topics in nuclear astrophysics with invited and contributed speakers from Japan, the US, and neighboring countries. We also organized the career-development events with the invited mentors. We expect that it was valuable for young researchers as they usually have few such occasions in Japan. The unconference, which is not common in Japan either, promoted active face-to-face communications among the participants, as well as the poster session. The organizers suggest possible improvements which may be helpful for the second workshop: more efficient organization of mentoring events (mentor talks before the mentor lunch, sharing gathered questions in advance, etc.), locating a more easy-to-access venue, organizing an excursion, more effective announcement to encourage balanced participation (countries, genders), and so on.

Finally, the organizers would like to thank IReNA, CNS, RCNP and RIKEN iTHEMS for their financial supports, and NAOJ for the venue provision and administrative supports. Special thanks to Agedoridori [4] for creating the nice workshop poster (Fig. 3).

References

[1] Workshop web page https://indico3.cns.s.u-tokyo.ac.jp/event/249/

[2] Ukakuren web page https://www.cns.s.u-tokyo.ac.jp/ukakuren/indexnew_e.html

[3] IReNA web page https://www.irenaweb.org/

[4] Agedoridori, Illustrator / Science Communicator https://agedoridori.jimdofree.com/

Appendices

Symposium, Workshop, Seminar, and PAC
CNS Reports
Publication List
Talks and Presentations
Awards, Press Releases, and Others
Personnel

Symposium, Workshop, Seminar, and PAC

A. Symposium and Workshop

1. OEDO/SHARAQ Workshop 2023
   CNS, July 6, 2023.
2. The 1st IReNA-Ukakuren Joint Workshop "Advancing Professional Development in Nuclear Astrophysics and Beyond"
   NAOJ, August 28–September 1, 2023.
3. ALICE+sPHENIX+STAR+EIC-J Workshop
   RIKEN Wako Campus, September 28–29, 2023.
4. 低エネルギー重イオン反応と超重元素の科学
   Gakushi Kaikan, March 3, 2023.

B. CNS Seminar

1. Prof. Kosuke Nomura (Hokkaido University), "Microscopic description of octupole collective excitations," June 15, 2023.
2. Prof. Hidetoshi Otono (Kyushu University), "First results from the FASER experiment at the LHC and prospect toward Forward Physics Facility in HL-LHC era," September 15, 2023.
3. Prof. Yi-Hua Lam (IMP, CAS), "Sensitivity of SAX J1808.4 $-$ 3658 Photospheric Radius Expansion Bursts to Thermonuclear Reaction-Rate Variations," February 27, 2024.
4. Prof. Angela Bonaccorso (INFN-Pisa), "Phenomenological and ab-initio optical potentials for nucleon-^{12}C scattering," March 13, 2024.

C. Program Advisory Committee for Nuclear-Physics Experiments at RI Beam Factory

1. The 24th NP-PAC meeting, December 5–7, 2023.

CNS Reports

#102 “CNS Annual Report 2022”
Edited by N. Kitamura, H. Nagahama, and S. Michimasa
March, 2024

Publication List

A. Original Papers

1. S. M. Cha, K. Y. Chae, K. Abe, S. Bae, D. N. Binh, S. H. Choi, N. N. Duy, Z. Ge, K. I. Hahn, S. Hayakawa, B. Hong, N. Iwasa, D. Kahl, L. H. Khiem, A. Kim, D. Kim, E. J. Kim, G. W. Kim, M. J. Kim, K. Kwak, M. S. Kwag, E. J. Lee, S. I. Lim, B. Moon, J. Y. Moon, S. Y. Park, V. H. Phong, H. Shimizu, H. Yamaguchi, L. Yang, "Investigation of ^{22}Mg levels via resonant scattering of ^{18}Ne + α", Frontiers in Physics **11** doi:10.3389/fphy.2023.1163299 (2023).

2. M. Z. Wang, D. Wu, H. Y. Lan, J. Y. Zhang, J. X. Liu, H. G. Lu, J. F. Lv, X. Z. Wu, H. Zhang, J. Cai, Q. Y. Ma, Y. H. Xia, Z. N. Wang, Z. Y. Yang, X. L. Xu, Y. X. Geng, Y. Y. Zhao, H. R. Wang, F. L. Liu, J. Q. Yu, K. J. Luo, W. Luo, X. Q. Yan, "Cross section measurements of ^{27}Al (γ, x) ^{24}Na reactions as monitors for laser-driven bremsstrahlung γ-ray", Nucl. Phys. A, **1043** 122834 (2024).

3. Xiaofeng Xi, Chong Lv, Wenjun Ma, Fulong Liu, Defeng Kong, Xiaopeng Zhang, Guoqiang Zhang, Wei Sun, Chuangye He, Xiangai Deng, Zhiguo Ma, Jiarui Zhao, Changbo Fu and Bing Guo, "Deuterium–deuterium fusion in nanowire plasma driven with a nanosecond high-energy laser", Frontiers in Physics, **11** 1212293 (2023).

4. C. B. Li, Y. Zheng, T. X. Li, X. G. Wu, H. Y. Wu, M. Zheng, Z. H. Zhao, Y. Q. Li, R. Hong, Z. Y. He, J. Z. Li, J. L. Wang, C. Y. Guo, Z. X. Zhou, L. Ni, G. S. Li, X. H. Zhou, B. Guo, S. Y. Wang, M. L. Liu, Y. H. Zhang, C. Y. He, F. L. Liu, S. Wang, and L. H. Zhu, "Lifetime measurements of the first 2^+ states in Te-116, 118", Phys. Rev. C **109**, 034310 (2024).

5. N. Imai, M. Dozono, S. Michimasa, T. Sumikama, S. Ota, S. Hayakawa, J. W. Hwang, K. Iribe, C. Iwamoto, S. Kawase, K. Kawata, N. Kitamura, S. Masuoka, K. Nakano, P. Schrock, D. Suzuki, R. Tsunoda, K. Wimmer, D. S. Ahn, O. Beliuskina, N. Chiga, N. Fukuda, E. Ideguchi, K. Kusaka, H. Miki, H. Miyatake, D. Nagae, S. Ohmika, M. Ohtake, H. J. Ong, H. Otsu, H. Sakurai, H. Shimizu, Y. Shimizu, X. Sun, H. Suzuki, M. Takaki, H. Takeda, S. Takeuchi, T. Teranishi, Y. Watanabe, Y. X. Watanabe, K. Yako, H. Yamada, H. Yamaguchi, L. Yang, R. Yanagihara, Y. Yanagisawa, K. Yoshida, S. Shimoura, "Neutron capture reaction cross-section of ^{79}Se through the ^{79}Se(d, p) reaction in inverse kinematics", Phys. Lett. B **850**, 138470 (2024).

6. Y. Shimizu, T. Kubo, T. Sumikama, N. Fukuda, H. Takeda, H. Suzuki, D. S. Ahn, N. Inabe, K. Kusaka, M. Ohtake, Y. Yanagisawa, K. Yoshida, Y. Ichikawa, T. Isobe, H. Otsu, H. Sato, T. Sonoda, D. Murai, N. Iwasa, N. Imai, Y. Hirayama, S. C. Jeong, S. Kimura, H. Miyatake, M. Mukai, D. G. Kim, E. Kim, A. Yagi "Production of new neutron-rich isotopes near the $N = 60$ isotones ^{92}Ge and ^{93}As by in-flight fission of a 345 MeV/nucleon ^{238}U beam" Phys. Rev. C **109**, 044313 (2024).

7. Shutaro Hanai, Shinsuke Ota, Reiko Kojima, Shoichiro Masuoka, Masanori Dozono, Nobuaki Imai, Shin ’ ichiro Michimasa, Susumu Shimoura, Juzo Zenihiro, Kento Inaba, Yuto Hijikata, Ru Longhi, Ryo Nakajima "Development of a fast-response Parallel-Plate Avalanche Counter with strip-readout for heavy-ion beams" Prog. Theor. Exp. Phys. **2023**, 123H02 (2023).

8. Thomas Chillery, Jongwon Hwang, Masanori Dozono, Nobuaki Imai, Shin ’ ichiro Michimasa, Toshiyuki Sumikama, Nobuyuki Chiga, Shinsuke Ota, Shinsuke Nakayama, Deuk Soon Ahn, Olga Beliuskina, Kazuya Chikaato, Naoki Fukuda, Seiya Hayakawa, Eiji Ideguchi, Kotaro Iribe, Chihiro Iwamoto, Shoichiro Kawase, Keita Kawata, Noritaka Kitamura, Kensuke Kusaka, Shoichiro Masuoka, Hareru Miki, Hiroari Miyatake, Daisuke Nagae, Ryo Nakajima, Keita Nakano, Masao Ohtake, Shunichiro Omika, Hooi Jin Ong, Hideaki Otsu, Hiroyoshi Sakurai, Philipp Schrock, Hideki Shimizu, Yohei Shimizu, Xiaohui Sun, Daisuke Suzuki, Hiroshi Suzuki, Motonobu Takaki, Maya Takechi, Hiroyuki Takeda, Satoshi Takeuchi, Takashi Teranishi, Rieko Tsunoda, He Wang, Yukinobu Watanabe, Yutaka X Watanabe, Kathrin Wimmer, Kentaro Yako, Hiroki Yamada, Kazunari Yamada, Hidetoshi Yamaguchi, Lei Yang, Rikuto Yanagihara, Yoshiyuki Yanagisawa, Hiroya Yoshida, Koichi Yoshida, Susumu Shimoura, "Studying the impact of deuteron non-elastic breakup on ^{93}Zr + d reaction cross sections measured at 28 MeV/nucleon", Prog. Theor. Exp. Phys. **2023**, 121D01 (2023).

9. J. G. Cubiss, A. N. Andreyev, A. E. Barzakh, P. Van Duppen, S. Hilaire, S. Peru, S. Goriely, M. Al Monthery, N. A. Althubiti, B. Andel, S. Antalic, D. Atanasov, K. Blaum, T. E. Cocolios, T. Day Goodacre, A. de Roubin, G. J. Farooq-Smith, D. V. Fedorov, V. N. Fedosseev, D. A. Fink, L. P. Gaffney, L. Ghys, R. D. Harding, M. Huyse, N. Imai, D. T. Joss, S. Kreim, D. Lunney, K. M. Lynch, V. Manea, B. A. Marsh, Y. Martinez Palenzuela, P. L.

Molkanov, D. Neidherr, G. G. O’Neill, R. D. Page, S. D. Prosnyak, M. Rosenbusch, R. E. Rossel, S. Rothe, L. Schweikhard, M. D. Seliverstov, S. Sels, L. V. Skripnikov, A. Stott, C. Van Beveren, E. Verstraelen, A. Welker, F. Wienholtz, R. N. Wolf, K. Zuber, “Deformation versus Sphericity in the Ground States of the Lightest Gold Isotopes”, Phys. Rev. Lett. **131**, 202501 (2023).

10. K. Wimmer, P. Ruotsalainen, S. M. Lenzi, A. Poves, T. Huyuk, F. Browne, P. Doornenbal, T. Koiwai, T. Arici, K. Auranen, M. A. Bentley, M. L. Cortes, C. Delafosse, T. Eronen, Z. Ge, T. Grahn, P. T. Greenlees, A. Illana, N. Imai, H. Joukainen, R. Julin, A. Jungclaus, H. Jutila, A. Kankainen, N. Kitamura, B. Longfellow, J. Louko, R. Lozeva, M. Luoma, B. Mauss, D. R. Napoli, M. Niikura, J. Ojala, J. Pakarinen, X. Pereira-Lopez, P. Rahkila, F. Recchia, M. Sandzelius, J. Saren, R. Taniuchi, H. Tann, S. Uthayakumaar, J. Uusitalo, V. Vaquero, R. Wadsworth, G. Zimba, R. Yajzey, “Isospin symmetry in the $T = 1, A = 62$ triplet”, Phys. Lett. B **847**, 138249 (2023).

11. S. Koyama, D. Suzuki, M. Assié, L. Lalanne, O. Sorlin, T. Abe, D. Beaumel, Y. Blumenfeld, L. Caceres, F. De Oliveira Santos, F. Delaunay, F. Flavigny, S. Franchoo, J. Gibelin, V. Girard-Alcindor, J. Guillot, F. Hammache, O. Kamalou, A. Kamenyero, N. Kitamura, V. Lapoux, A. Lemasson, A. Matta, B. Mauss, P. Morfouace, M. Niikura, H. Otsu, J. Pancin, T. Roger, T. Y. Saito, H. Sakurai, C. Stodel, and J-C. Thomas, “Mirror symmetry at far edges of stability: The cases of ^{8}C and ^{8}He”, Phys. Rev. C **109**, L031301 (2024).

12. Shoichiro Kawase, Takuya Murota, Hiroya Fukuda, Masaya Oishi, Teppei Kawata, Kentaro Kitafuji, Seiya Manabe, Yukinobu Watanabe, Hiroki Nishibata, Shintaro Go, Tamito Kai, Yuto Nagata, Taiga Muto, Yuichi Ishibashi, Megumi Niikura, Daisuke Suzuki, Teiichiro Matsuzaki, Katsuhiko Ishida, Rurie Mizuno, Noritaka Kitamura, “Effect of large-angle incidence on particle identification performance for light-charged ($Z \leq 2$) particles by pulse shape analysis with a pad-type nTD silicon detector”, Nuclear Instruments and Methods in Physics Research Section A **1059**, 168984 (2024).

13. P. J. Li, D. Beaumel, J. Lee, M. Assié, S. Chen, S. Franchoo, J. Gibelin, F. Hammache, T. Harada, Y. Kanada-En’yo, Y. Kubota, S. Leblond, P. F. Liang, T. Lokotko, M. Lyu, F. M. Marqués, Y. Matsuda, K. Ogata, H. Otsu, E. Rindel, L. Stuhl, D. Suzuki, Y. Togano, T. Tomai, X. X. Xu, K. Yoshida, J. Zenihiro, N. L. Achouri, T. Aumann, H. Baba, G. Cardella, S. Ceruti, A. I. Stefanescu, A. Corsi, A. Frotscher, J. Gao, A. Gillibert, K. Inaba, T. Isobe, T. Kawabata, N. Kitamura, T. Kobayashi, Y. Kondo, A. Kurihara, H. N. Liu, H. Miki, T. Nakamura, A. Obertelli, N. A. Orr, V. Panin, M. Sasano, T. Shimada, Y. L. Sun, J. Tanaka, L. Trache, D. Tudor, T. Uesaka, H. Wang, H. Yamada, Z. H. Yang, and M. Yasuda, “Validation of the 10Be ground state molecular structure using ^{10}Be(p,pα)^{6}He triple differential reaction cross-section measurements” Phys. Rev. Lett. **131**, 212501 (2023).

14. L. Lalanne, O. Sorlin, A. Poves, M. Assié, F. Hammache, S. Koyama, D. Suzuki, F. Flavigny, V. Girard-Alcindor, A. Lemasson, A. Matta, T. Roger, D. Beaumel, Y Blumenfeld, B. A. Brown, F. De Oliveira Santos, F. Delaunay, N. de Séréville, S. Franchoo, J. Gibelin, J. Guillot, O. Kamalou, N. Kitamura, V. Lapoux, B. Mauss, P. Morfouace, J. Pancin, T. Y. Saito, C. Stodel, and J-C. Thomas, “$N = 16$ Magicity Revealed at the Proton Drip Line through the Study of ^{35}Ca”, Phys. Rev. Lett. **131**, 092501 (2023).

15. R. Yokoyama, R. Grzywacz, B. C. Rasco, N. Brewer, K. P. Rykaczewski, I. Dillmann, J. L. Tain, S. Nishimura, D. S. Ahn, A. Algora, J. M. Allmond, J. Agramunt, H. Baba, S. Bae, C. G. Bruno, R. Caballero-Folch, F. Calvino, P. J. Coleman-Smith, G. Cortes, T. Davinson, C. Domingo-Pardo, A. Estrade, N. Fukuda, S. Go, C. J. Griffin, J. Ha, O. Hall, L. J. Harkness-Brennan, J. Heideman, T. Isobe, D. Kahl, M. Karny, T. Kawano, L. H. Khiem, T. T. King, G. G. Kiss, A. Korgul, S. Kubono, M. Labiche, I. Lazarus, J. Liang, J. Liu, G. Lorusso, M. Madurga, K. Matsui, K. Miernik, F. Montes, A. I. Morales, P. Morrall, N. Nepal, R. D. Page, V. H. Phong, M. Piersa-Siłkowska, M. Prydderch, V. F. E. Pucknell, M. M. Rajabali, B. Rubio, Y. Saito, H. Sakurai, Y. Shimizu, J. Simpson, M. Singh, D. W. Stracener, T. Sumikama, H. Suzuki, H. Takeda, A. Tarifeño-Saldivia, S. L. Thomas, A. Tolosa-Delgado, M. Wolińska-Cichocka, P. J. Woods, X. X. Xu, “β-delayed neutron emissions from $N > 50$ gallium isotopes” Phys. Rev. C **108**, 064307 (2023).

16. Z. Y. Xu, M. Madurga, R. Grzywacz, T. T. King, A. Algora, A. N. Andreyev, J. Benito, T. Berry, M. J. G. Borge, C. Costache, H. De Witte, A. Fijalkowska, L. M. Fraile, H. O. U. Fynbo, A. Gottardo, C. Halverson, L. J. Harkness-Brennan, J. Heideman, M. Huyse, A. Illana, Ł. Janiak, D. S. Judson, A. Korgul, T. Kurtukian-Nieto, I. Lazarus, R. Lică, R. Lozeva, N. Marginean, R. Marginean, C. Mazzocchi, C. Mihai, R. E. Mihai, A. I. Morales, R. D. Page, J. Pakarinen, M. Piersa-Siłkowska, Zs. Podolyák, P. Sarriguren, M. Singh, Ch. Sotty, M. Stepaniuk, O. Tengblad, A. Turturica, P. Van Duppen, V. Vedia, S. Viñals, N. Warr, R. Yokoyama, C. X. Yuan, “^{133}In: A Rosetta Stone for Decays of r-Process Nuclei”, Phys. Rev. Lett. **131**, 022501 (2023).

17. Z. Y. Xu, M. Madurga, R. Grzywacz, T. T. King, A. Algora, A. N. Andreyev, J. Benito, T. Berry, M. J. G. Borge, C. Costache, H. De Witte, A. Fijalkowska, L. M. Fraile, H. O. U. Fynbo, A. Gottardo, C. Halverson, L. J. Harkness-Brennan, J. Heideman, M. Huyse, A. Illana, Ł. Janiak, D. S. Judson, A. Korgul, T. Kurtukian-Nieto, I. Lazarus, R. Lică, R. Lozeva, N. Marginean, R. Marginean, C. Mazzocchi, C. Mihai, R. E. Mihai, A. I. Morales, R. D. Page, J. Pakarinen, M. Piersa-Siłkowska, Zs. Podolyák, P. Sarriguren, M. Singh, Ch. Sotty, M. Stepaniuk, O. Tengblad, A. Turturica, P. Van Duppen, V. Vedia, S. Viñals, N. Warr, R. Yokoyama, C. X. Yuan "β-delayed neutron spectroscopy of ^{133}In", Phys. Rev. C **108**, 014314 (2023).

18. L. G. Pedersen, E. Sahin, A. Görgen, F. L. Bello Garrote, Y. Tsunoda, T. Otsuka, M. Niikura, S. Nishimura, Z. Xu, H. Baba, G. Benzoni, F. Browne, A. M. Bruce, S. Ceruti, F. C. L. Crespi, R. Daido, G. de Angelis, M.-C. Delattre, Zs. Dombradi, P. Doornenbal, Y. Fang, S. Franchoo, G. Gey, A. Gottardo, T. Isobe, P. R. John, H. S. Jung, I. Kojouharov, T. Kubo, N. Kurz, I. Kuti, Z. Li, G. Lorusso, I. Matea, K. Matsui, D. Mengoni, T. Miyazaki, V. Modamio, S. Momiyama, A. I. Morales, P. Morfouace, D. R. Napoli, F. Naqvi, H. Nishibata, A. Odahara, R. Orlandi, Z. Patel, S. Rice, H. Sakurai, H. Schaffner, L. Sinclair, P.-A. Söderström, D. Sohler, I. G. Stefan, T. Sumikama, D. Suzuki, R. Taniuchi, J. Taprogge, Z. Vajta, J. J. Valiente-Dobón, H. Watanabe, V. Werner, J. Wu, A. Yagi, M. Yalcinkaya, R. Yokoyama, K. Yoshinaga, "First spectroscopic study of odd-odd ^{78}Cu", Phys. Rev. C **107**, 044301 (2023)

19. W. Xian, S. Chen, S. Nikas, M. Rosenbusch, M. Wada, H. Ishiyama, D. Hou, S. Iimura, S. Nishimura, P. Schury, A. Takamine, S. Yan, F. Browne, P. Doornenbal, F. Flavigny, Y. Hirayama, Y. Ito, S. Kimura, T. M. Kojima, J. Lee, J. Liu, H. Miyatake, S. Michimasa, J. Y. Moon, S. Naimi, T. Niwase, T. Sonoda, D. Suzuki, Y. X. Watanabe, V. Werner, K. Wimmer, and H. Wollnik, "Mass measurements of neutron-rich $A \approx 90$ nuclei constrain element abundances," Phys. Rev. C **109**, 035804 (2024).

20. D. S. Hou, A. Takamine, M. Rosenbusch, W. D. Xian, S. Iimura, S. D. Chen, M. Wada, H. Ishiyama, P. Schury, Z. M. Niu, H.Z. Liang, S. X. Yan, P. Doornenbal, Y. Hirayama, Y. Ito, S. Kimura, T.M. Kojima, W. Korten, J. Lee, J. J. Liu, Z. Liu, S. Michimasa, H. Miyatake, J. Y. Moon, S. Naimi, S. Nishimura, T. Niwase, T. Sonoda, D. Suzuki, Y.X. Watanabe, K. Wimmer, and H. Wollnik, "First direct mass measurement for neutron-rich ^{112}Mo with the new ZD-MRTOF mass spectrograph system," Phys. Rev. C **108**, 054312 (2023).

21. Chihiro Iwamoto, Shinsuke Ota, Reiko Kojima, Hiroshi Tokieda, Seiya Hayakawa, Yutaka Mizoi, Taku Gunji, Hidetoshi Yamaguchi, Nobuaki Imai, Masanori Dozono, Ryo Nakajima, Olga Beliuskina, Shin'ichiro Michimasa, Rin Yokoyama, Keita Kawata, Daisuke Suzuki, Tadaaki Isobe, Juzo Zenihiro, Yohei Matsuda, Jun Okamoto, Tetsuya Murakami, and Eiichi Takada, "Performance of prototype dual gain multilayer thick gas electron multiplier with high-intensity heavy-ion beam injections in low-pressure hydrogen gas," Prog. Theor. Exp. Phys. **2023**, 083H01 (2023).

22. Rurie Mizuno, Megumi Niikura, Tokihiro Ikeda, Teiichiro Matsuzaki, Shintaro Go, Takeshi Y. Saito, Shin'ichiro Michimasa, and Hiroyoshi Sakurai, "Response of germanium detectors for high-energy γ-rays by ^{27}Al(p,γ)^{28}Si at $E_p = 992$ keV," Prog. Theor. Exp. Phys. **2023**, 053H01 (2023).

23. W. Horiuchi, T. Inakura, S. Michimasa, and M.Tanaka, "Enlarged deformation region in neutron-rich Zr isotopes promoted by the second intruder orbit," Phys. Rev. C **107**, L041304 (2023).

24. J. Alme *et al.* [ALICE TPC], "Signal shapes in multiwire proportional chamber-based TPCs," JINST **19**, no.02, P02038 (2024)

25. N. J. Abdulameer *et al.* [PHENIX], "Identified charged-hadron production in p+Al, He3+Au, and Cu+Au collisions at $\sqrt{s_{NN}}$=200 GeV and in U+U collisions at $\sqrt{s_{NN}}$=193GeV," Phys. Rev. C **109**, no.5, 054910 (2024)

26. S. Acharya *et al.* [ALICE], "Emergence of Long-Range Angular Correlations in Low-Multiplicity Proton-Proton Collisions," Phys. Rev. Lett. **132**, no.17, 172302 (2024)

27. S. Acharya *et al.* [ALICE], "Observation of abnormal suppression of f0(980) production in p–Pb collisions at $\sqrt{s_{NN}}$ = 5.02 TeV," Phys. Lett. B **853**, 138665 (2024)

28. T. N. Murakami, K. Aoki, S. Ashikaga, H. En'yo, T. Gunji, H. Hamagaki, M. Ichikawa, K. Kanno, S. Kobayashi and Y. Komatsu, *et al.* "Construction of gas electron multiplier tracker for the J-PARC E16 experiment," Nucl. Instrum. Meth. A **1058**, 168817 (2024)

29. S. Acharya *et al.* [ALICE], "Charged-particle production as a function of the relative transverse activity classifier in pp, p–Pb, and Pb–Pb collisions at the LHC," JHEP **01**, 199 (2024)

30. S. Acharya *et al.* [ALICE], “Femtoscopic correlations of identical charged pions and kaons in pp collisions at $\sqrt{s}$=13 TeV with event-shape selection,” Phys. Rev. C **109**, no.2, 024915 (2024)

31. S. Acharya *et al.* [ALICE], “Multiplicity and event-scale dependent flow and jet fragmentation in pp collisions at $\sqrt{s}$ = 13 TeV and in p–Pb collisions at $\sqrt{s_{\mathrm{NN}}}$ = 5.02 TeV,” JHEP **03**, 092 (2024)

32. S. Acharya *et al.* [ALICE], “Measurements of long-range two-particle correlation over a wide pseudorapidity range in p−Pb collisions at $\sqrt{s_{NN}}$ = =5.0 TeV,” JHEP **01**, 199 (2024)

33. S. Acharya *et al.* [ALICE], “Probing the chiral magnetic wave with charge-dependent flow measurements in Pb-Pb collisions at the LHC,” JHEP **12**, 067 (2023)

34. S. Acharya *et al.* [ALICE], “Prompt and non-prompt J/ψ production at midrapidity in Pb–Pb collisions at $\sqrt{s_{\mathrm{NN}}}$ = 5.02 TeV,” JHEP **02**, 066 (2024)

35. S. Acharya *et al.* [ALICE], “K*(892)± resonance production in Pb-Pb collisions at $\sqrt{s_{NN}}$=5.02 TeV,” Phys. Rev. C **109**, no.4, 044902 (2024)

36. S. Acharya *et al.* [ALICE], “Skewness and kurtosis of mean transverse momentum fluctuations at the LHC energies,” Phys. Lett. B **850**, 138541 (2024)

37. S. Acharya *et al.* [ALICE], “System-size dependence of the hadronic rescattering effect at energies available at the CERN Large Hadron Collider,” Phys. Rev. C **109**, no.1, 014911 (2024)

38. S. Acharya *et al.* [ALICE], “Study of flavor dependence of the baryon-to-meson ratio in proton-proton collisions at $\sqrt{s}$=13 TeV,” Phys. Rev. D **108**, no.11, 112003 (2023)

39. S. Acharya *et al.* [ALICE], “Charm production and fragmentation fractions at midrapidity in pp collisions at $\sqrt{\mathrm{s}}$ = 13 TeV,” JHEP **12**, 086 (2023)

40. S. Acharya *et al.* [ALICE], “Measurement of non-prompt D^0-meson elliptic flow in Pb–Pb collisions at $\sqrt{s_{\mathrm{NN}}}$ = 5.02 TeV,” Eur. Phys. J. C **83**, no.12, 1123 (2023)

41. S. Acharya *et al.* [ALICE], “Modification of charged-particle jets in event-shape engineered Pb–Pb collisions at $\sqrt{s_{NN}}$=5.02 TeV,” Phys. Lett. B **851**, 138584 (2024)

42. S. Acharya *et al.* [ALICE], “Measurement of inclusive charged-particle jet production in pp and p-Pb collisions at $\sqrt{s_{\mathrm{NN}}}$ = 5.02 TeV,” JHEP **05**, 041 (2024)

43. S. Acharya *et al.* [ALICE], “Pseudorapidity dependence of anisotropic flow and its decorrelations using long-range multiparticle correlations in Pb–Pb and Xe–Xe collisions,” Phys. Lett. B **850**, 138477 (2024) [erratum: Phys. Lett. B **853**, 138659 (2024)]

44. S. Acharya *et al.* [ALICE], “Measurement of the low-energy antitriton inelastic cross section,” Phys. Lett. B **848**, 138337 (2024)

45. S. Acharya *et al.* [ALICE], “Energy dependence of coherent photonuclear production of J/ψ mesons in ultra-peripheral Pb-Pb collisions at $\sqrt{\mathrm{s_{NN}}}$ = 5.02 TeV,” JHEP **10**, 119 (2023)

46. S. Acharya *et al.* [ALICE], “Accessing the strong interaction between Λ baryons and charged kaons with the femtoscopy technique at the LHC,” Phys. Lett. B **845**, 138145 (2023)

47. S. Acharya *et al.* [ALICE], “First Measurement of the |t| Dependence of Incoherent J/ψ Photonuclear Production,” Phys. Rev. Lett. **132**, no.16, 162302 (2024)

48. S. Acharya *et al.* [ALICE], “Exclusive and dissociative J/ψ photoproduction, and exclusive dimuon production, in p-Pb collisions at sNN=8.16 TeV,” Phys. Rev. D **108**, no.11, 112004 (2023)

49. J. Alme *et al.* [ALICE TPC], “Correction of the baseline fluctuations in the GEM-based ALICE TPC,” JINST **18**, no.11, P11021 (2023)

50. S. Acharya *et al.* [ALICE], “Data-driven precision determination of the material budget in ALICE,” JINST **18**, no.11, P11032 (2023)

51. S. Acharya *et al.* [ALICE], “Measurement of inclusive J/ψ pair production cross section in pp collisions at $\sqrt{s}$=13 TeV,” Phys. Rev. C **108**, no.4, 045203 (2023)

52. S. Acharya *et al.* [ALICE], “Study of the p–p–K^{+} and p–p–K^{-} dynamics using the femtoscopy technique,” Eur. Phys. J. A **59**, no.12, 298 (2023)

53. S. Acharya *et al.* [ALICE], “Inclusive and multiplicity dependent production of electrons from heavy-flavour hadron decays in pp and p-Pb collisions,” JHEP **08**, 006 (2023)

54. S. Acharya *et al.* [ALICE], “Measurements of inclusive J/ψ production at midrapidity and forward rapidity in Pb–Pb collisions at $\sqrt{s_{NN}}$ = 5.02 TeV,” Phys. Lett. B **849**, 138451 (2024)

55. S. Acharya *et al.* [ALICE], “Higher-order correlations between different moments of two flow amplitudes in Pb-Pb collisions at $\sqrt{s_{NN}}$=5.02 TeV,” Phys. Rev. C **108**, no.5, 055203 (2023)

56. N. J. Abdulameer *et al.* [PHENIX], “Transverse single-spin asymmetry of midrapidity π0 and η mesons in p+Au and p+Al collisions at $\sqrt{s_{NN}}$=200 GeV,” Phys. Rev. D **107**, no.11, 112004 (2023)

57. N. J. Abdulameer *et al.* [PHENIX], “Transverse single-spin asymmetry of charged hadrons at forward and backward rapidity in polarized p+p, p+Al, and p+Au collisions at $\sqrt{s_{NN}}$=200 GeV,” Phys. Rev. D **108**, no.7, 072016 (2023)

58. S. Acharya *et al.* [ALICE], “Inclusive photon production at forward rapidities in pp and p–Pb collisions at $\sqrt{s_{\mathrm{NN}}}$ = 5.02 TeV,” Eur. Phys. J. C **83**, no.7, 661 (2023)

59. S. Acharya *et al.* [ALICE], “Azimuthal correlations of heavy-flavor hadron decay electrons with charged particles in pp and p–Pb collisions at $\sqrt{s_{NN}}$ = 5.02 TeV,” Eur. Phys. J. C **83**, no.8, 741 (2023)

60. S. Acharya *et al.* [ALICE], “Measurement of the radius dependence of charged-particle jet suppression in Pb–Pb collisions at $\sqrt{s_{NN}}$=5.02TeV,” Phys. Lett. B **849**, 138412 (2024)

61. S. Acharya *et al.* [ALICE], “Measurement of the non-prompt D-meson fraction as a function of multiplicity in proton-proton collisions at $\sqrt{s}$ = 13 TeV,” JHEP **10**, 092 (2023)

62. S. Acharya *et al.* [ALICE], “Symmetry plane correlations in Pb-Pb collisions at $\sqrt{s_{NN}}$ = 2.76 TeV,” Eur. Phys. J. C **83**, no.7, 576 (2023)

63. S. Acharya *et al.* [ALICE], “Measurement of the fraction of jet longitudinal momentum carried by Λc+ baryons in pp collisions,” Phys. Rev. D **109**, no.7, 072005 (2024)

64. S. Acharya *et al.* [ALICE], “Production of pions, kaons, and protons as a function of the relative transverse activity classifier in pp collisions at $\sqrt{s}$ = 13 TeV,” JHEP **06**, 027 (2023)

65. S. Bhattacharya, V. Tripathi, E. Rubino, S. Ajayi, L. T. Baby, C. Benetti, R. S. Lubna, S. L. Tabor, J. Döring, Y. Utsuno, N. Shimizu, J. M. Almond, and G. Mukherjee, “Coexistence of single-particle and collective excitation in ^{61}Ni,” Phys. Rev. C **107**, 054311 (2023).

66. S. Chen, F. Browne, P. Doornenbal, J. Lee, A. Obertelli, Y. Tsunoda, T. Otsuka, Y. Chazono, G. Hagen, J. D. Holt, G. R. Jansen, K. Ogata, N. Shimizu, Y. Utsuno, K. Yoshida, N. L. Achouri, H. Baba, D. Calvet, F. Château, N. Chiga, A. Corsi, M. L. Cortés, A. Delbart, J.-M. Gheller, A. Giganon, A. Gillibert, C. Hilaire, T. Isobe, T. Kobayashi, Y. Kubota, V. Lapoux, H. N. Liu, T. Motobayashi, I. Murray, H. Otsu, V. Panin, N. Paul, W. Rodriguez, H. Sakurai, M. Sasano, D. Steppenbeck, L. Stuhl, Y. L. Sun, Y. Togano, T. Uesaka, K. Wimmer, K. Yoneda, O. Aktas, T. Aumann, L. X. Chung, F. Flavigny, S. Franchoo, I. Gašparić, R.-B. Gerst, J. Gibelin, K. I. Hahn, D. Kim, T. Koiwai, Y. Kondo, P. Koseoglou, C. Lehr, B. D. Linh, T. Lokotko, M. MacCormick, K. Moschner, T. Nakamura, S. Y. Park, D. Rossi, E. Sahin, P.-A. Söderström, D. Sohler, S. Takeuchi, H. Törnqvist, V. Vaquero, V. Wagner, S. Wang, V. Werner, X. Xu, H. Yamada, D. Yan, Z. Yang, M. Yasuda and L. Zanetti, “Level structures of ^{56,58}Ca cast doubt on a doubly magic ^{60}Ca,” Phys. Lett. B **843**, 138025 (2023).

67. S. Lechner, T. Miyagi, Z. Y. Xu, M. L. Bissell, K. Blaum, B. Cheal, C. S. Devlin, R. F. Garcia Ruiz, J. S. M. Ginges, H. Heylen, J. D. Holt, P. Imgram, A. Kanellakopoulos, Á. Koszorús, S. Malbrunot-Ettenauer, R. Neugart, G. Neyens, W. Nörtershäuser, P. Plattner, L. V. Rodríguez, G. Sanamyan, S. R. Stroberg, Y. Utsuno, X. F. Yang, and D. T. Yordanov, “Electromagnetic moments of the antimony isotopes $^{112-133}$Sb,” Phys. Lett. B **847**, 138278 (2023).

68. T. Shizuma, M. Omer, T. Hayakawa, F. Minato, S. Matsuba, S. Miyamoto, N. Shimizu ,and Y. Utsuno, “Parity assignment for low-lying dipole states in ^{58}Ni,” Phys. Rev. C **109**, 014302 (2024).

69. S. Ajayi, V. Tripathi, E. Rubino, S. Bhattacharya, L. T. Baby, R. S. Lubna, C. Benetti, C. Wibisono, MacMillan B. Wheeler, S. L. Tabor, Y. Utsuno, N. Shimizu, and J. M. Allmond, “Observation of collective modes of excitations in ^{59}Co, ^{59}Ni, and ^{61}Co and the influence of the $g_{9/2}$ orbital,” Phys. Rev. C **109**, 014305 (2024).

70. D. Patel, P. C. Srivastava, N. Shimizu, and Y. Utsuno, “Systematic shell-model study of $^{99-129}$Cd isotopes and isomers in neutron-rich $^{127-131}$In isotopes,” Phys. Rev. C **109**, 014310 (2024).

71. H. Utsunomiya, S. Goriely, M. Kimura, N. Shimizu, Y. Utsuno, G. M. Tveten, T. Renstrøm, T. Ari-izumi, and S. Miyamoto, “Photoneutron emission cross sections for ^{13}C,” Phys. Rev. C **109**, 014617 (2024).

72. B. D. Linh, A. Corsi, A. Gillibert, A. Obertelli, P. Doornenbal, C. Barbieri, T. Duguet, M. Gómez-Ramos, J. D. Holt, B. S. Hu, T. Miyagi, A. M. Moro, P. Navrátil, K. Ogata, S. Péru, N. T. T. Phuc, N. Shimizu, V. Somá, Y. Utsuno, N. L. Achouri, H. Baba, F. Browne, D. Calvet, F. Château, S. Chen, N. Chiga, M. L. Cortés, A. Delbart, J.-M. Gheller, A. Giganon, C. Hilaire, T. Isobe, T. Kobayashi, Y. Kubota, V. Lapoux, H. N. Liu, T. Motobayashi, I. Murray, H. Otsu, V. Panin, N. Paul, W. Rodriguez, H. Sakurai, M. Sasano, D. Steppenbeck, L. Stuhl, Y. L. Sun, Y. Togano, T. Uesaka, K. Wimmer, K. Yoneda, O. Aktas, T. Aumann, L. X. Chung, F. Flavigny, S. Franchoo, I. Găsparić, R.-B. Gerst, J. Gibelin, K. I. Hahn, N. T. Khai, D. Kim, T. Koiwai, Y. Kondo, P. Koseoglou, J. Lee, C. Lehr, T. Lokotko, M. MacCormick, K. Moschner, T. Nakamura, S. Y. Park, D. Rossi, E. Sahin, D. Sohler, P.-A. Söderström, S. Takeuchi, H. Törnqvist, V. Vaquero, V. Wagner, S. T. Wang, V. Werner, X. Xu, H. Yamada, D. Yan, Z. Yang, M. Yasuda and L. Zanetti, “Onset of collectivity for argon isotopes close to $N = 32$,” Phys. Rev. C **109**, 034312 (2024).

73. Y. Tsunoda, N. Shimizu, and T. Otsuka, “Shape transition of Nd and Sm isotopes and the neutrinoless double-β-decay nuclear matrix element of ^{150}Nd,” Phys. Rev. C **108**, L021302 (2023).

74. A. Illana, M. Zielińska, M. Huyse, E. Rapisarda, P. Van Duppen, K. Wrzosek-Lipska, S. M. Lenzi, F. Nowacki, D. D. Dao, T. Otsuka, Y. Tsunoda, K. Arnswald, M. J. G. Borge, J. Cederkäll, K. Chrysalidis, M. L. Cortés, D. M. Cox, T. Day Goodacre, H. De Witte, D. T. Doherty, V. Fedosseev, L. P. Gaffney, K. Hadyńska-Klek, H. Hess, C. Henrich, M. Hlebowicz, M. Komorowska, W. Korten, Th. Kröll, M. L. Lozano Benito, R. Lutter, B. Marsh, L. Martikainen, M. Matejska-Minda, P. L. Molkanov, E. Nacher, A. Nannini, P. J. Napiorkowski, J. Pakarinen, P. Papadakis, M. Queiser, P. Reiter, M. Rocchini, J. A. Rodriguez, T. Rolke, D. Rosiak, S. Rothe, M. Seidlitz, C. Seiffert, B. Siebeck, E. Siesling, J. Snäll, J. Srebrny, S. Thiel, N. Warr, and F. Wenander, “Coulomb excitation of ^{74,76}Zn,” Phys. Rev. C **108**, 044305 (2023).

75. Daid Kahl, Hidetoshi Yamaguchi and Seiya Hayakawa, “Alpha Clustering in Nuclear Astrophysics and Topology”, Frontiers in Physics **11** doi:10.3389/fphy.2023.1189040 (2023).

B. Proceedings

1. Y. Kotaka, K. Kamakura, H. Yamaguchi, N. Imai, Y. Sakemi, J. Ohnishi, K. Hatanaka, “Development of pepper-pot emittance monitor for high-intensity ion beam accelerated by RIKEN AVF Cyclotron,” Proceedings of the 12th International Beam Instrumentation Conference, doi:10.18429/JACoW-IBIC2023-WEP006 (2024).

2. A. A. Oliva, A. Tumino, N. Soic, P. M. Prajapati, L. Acosta, R. Alba, F. Barba, S. Cherubini, G. D ’ Agata, D. Dell ’ Aquila, A. Di Pietro, J. P. Fernandez, P. Figuera, D. Galaviz Redondo, L. Guardo, M. Gulino, F. Hammache, D. Jelavic Malenica, A. I. Kilic, M. La Cognata, M. La Commara, L. Lamia, D. Lattuada, C. Maiolino, G. Manico, M. Mazzocco, M. Milin, Nanru Ma, A. Nurmukhanbetova, D. Nurkic, S. Palmerini, T. Parascandolo, D. Pierroutsakou, R.G., Pizzone, R. Popocovski, G. G. Rapisarda, S. Romano, D. Santonocito, M.L. Sergi, A. Shotter, R. Sparta, A. Spiridon, L. Trache, N. Vukman, H. Yamaguchi, “Study of the ^{12}C+^{16}O fusion reaction in carbon burning via the trojan horse method”, EPJ Web Conf. **279**, 11015 (2023).

3. H. Murakami for the ALICE collaboration, “Electromagnetic radiation in pp and Pb–Pb collisions with dielectrons in ALICE”, Proceedings of European Physical Society Conference on High Energy Physics (EPS-HEP2023), PoS, Vol. EPS-HEP2023, Page 207, 2024

4. S. Michimasa, T. Chillery, J.W. Hwang, T. Sumikama, S. Hanai, N. Imai, M. Dozono, S. Ota, D.S. Ahn, S. Hayakawa, Y. Hijikata, K. Kameya, K. Kawata, R. Kojima, K. Kusaka, J. Li, K. Miki, M. Ohtake, Y. Shimizu, D. Suzuki, H. Suzuki, H. Takeda, K. Yako, Y. Yanagisawa, K. Yoshida, M. Yoshimoto, S. Shimoura, “OEDO-SHARAQ system: Multifaceted performances in low-energy RI production and high-resolution spectroscopy”, Nuclear Instruments and Methods B, **540** 194 (2023).
5. S. Hanai, S. Ota, R. Kojima, S. Masuoka, M. Dozono, N. Imai, S. Michimasa, S. Shimoura, J. Zenihiro, K. Inaba, Y. Hijikata, “Development of Strip-Readout PPAC for high-intensity heavy ions”, Nuclear Instruments and Methods B **541**, 194 (2023).
6. Y. Hijikata, J. Zenihiro, H. Baba, M. Dozono, S. Enyo, N. Fukuda, T. Harada, Y. Matsuda, S. Michimasa, D. Nishimura, S. Nishimura, S. Ota, Y. Shimizu, H. Sakaguchi, H. Sato, S. Sugawara, H. Suzuki, H. Takahashi, H. Takeda, S. Takeshige, J. Tanaka, S. Terashima, R. Tsuji, T. Uesaka, K. Yoshida, “Development of a gaseous Xe scintillator for particle identification of high-intensity and heavy ion beams”, Nuclear Instruments and Methods B **541**, 333 (2023).

C. Theses

1. M. Sato: “Development of an Atomic Beam Source of Francium-221 for its Permanent Electric Dipole Moment Search” PhD Thesis, the University of Tokyo, March, 2024.

Talks and Presentations

A. International Conference

1. Y. Kotaka (poster), “Development of pepper-pot emittance monitor for high-intensity ion beam accelerated by RIKEN AVF Cyclotron”, 12th International Beam Instrumentation Conference, Saskatoon, Canada, September 11-14,2023.

2. Y. Kotaka (poster), “Beam emittance measurement and beam trajectory calculation”, UTokyo ETHZ UZH Symposium 2023, ETHZ Hönggerberg, Zurich, Switzerland, October 15–17, 2023.

3. K. Kamakura (poster), “Status Report on the 14 GHz ECR Ion Source at CNS/UTokyo”, UTokyo ETHZ UZH Symposium 2023, ETHZ Hönggerberg, Zurich, Switzerland, October 15–17, 2023.

4. H. Yamaguchi (oral), “Nuclear Astrophysics with low-energy RI beams at CRIB”, 17th International Symposium on Nuclei in the Cosmos (NIC XVII), Institute for Basic Science (IBS), Daejeon, Korea, September 17–22, 2023.

5. H. Yamaguchi (oral, invited), “Nuclear Astrophysics with Exotic Beam; thick-target method measurements at CRIB”, International Symposium on Nuclear Astrophysics (ISNA2023), Manipal Centre for Natural Sciences (MCNS), Manipal Academy of Higher Education (MAHE), Manipal, India, October 30–November 3, 2023.

6. H. Yamaguchi (oral, invited), “Experiments with low-energy RI beams at CRIB - history, present and future”, The 3rd RIKEN-IBS Joint Conference on Nuclear Physics, RIKEN Nishina Center, Wako, Japan, January 25–26, 2024.

7. S. Hayakawa (invited), “Measurement and R-matrix analysis of the ^{7}Be + n reactions updating the primordial lithium abundance”, 2023 R-matrix Workshop on Methods and Applications, Athens, Ohio, USA, June 20–23, 2023.

8. S. Hayakawa (poster), “Measurement and evaluation of the ^{7}Be + n reactions approaching the cosmological lithium problem”. 17th International Symposium on Nuclei in the Cosmos (NIC XVII), Daejeon, Republic of Korea, September 17—22, 2023.

9. S. Hayakawa (oral), “^{26}Si + α resonant scattering measurement for the astrophysical ^{26}Si(α, p)^{29}P reaction rate”, The 2023 Fall Meeting of the Division of Nuclear Physics of the American Physical Society and the Physical Society of Japan, Waikoloa, Hawaii, USA, November 26–December 1, 2023.

10. S. Hayakawa (invited), “Measurements of the ^{7}Be-destructive reactions relevant to the primordial ^{7}Li abundance”, ASRC International Workshop “Nuclear Astrophysics with Stable Beams”, Tokai, Ibaraki, Japan, February 20–24, 2024.

11. K. Okawa (poster), “Direct measurement of the ^{26}Si(α, p)^{29}P reaction for the nucleosynthesis in the X-ray bursts”, The 1st IReNA-Ukakuren Joint Workshop “Advancing Professional Development in Nuclear Astrophysics and Beyond”, Mitaka, Tokyo, Japan, August 28–Sepember 1, 2023.

12. K. Okawa (poster), “Direct measurement of the ^{26}Si(α, p)^{29}P reaction at CRIB for the nucleosynthesis in the X-ray bursts,” 17th International Symposium on Nuclei in the Cosmos (NIC XVII), Daejeon, Republic of Korea, September 17—22, 2023.

13. K. Okawa (oral), “Direct measurement of the ^{26}Si(α, p)^{29}P reaction for the nucleosynthesis in the X-ray bursts”, The 2023 Fall Meeting of the Division of Nuclear Physics of the American Physical Society and the Physical Society of Japan, Waikoloa, Hawaii, USA, November 26–December 1, 2023.

14. Q. Zhang (oral), “Experimental study of halo structure and neutron correlations in ^{6}He nuclei at CRIB via elastic and transfer reaction: p+^{6}He,” The 22nd CNS International Summer School (A3F-CNSSS23), Nishina hall, RIKEN, Japan, August 4–10, 2023.

15. Q. Zhang (poster), “Astrophysical S(E) for the ^{9}Be(p, d)^{8}Be and ^{9}Be(p, α)^{6}Li Reactions by Direct Measurement,” The 1st IReNA-Ukakuren Joint Workshop “Advancing Professional Development in Nuclear Astrophysics and Beyond”, National Astronomical Observatory of Japan (NAOJ), Mitaka, Japan, August 28–September 1, 2023.

16. Q. Zhang (poster), “A study of ^{6}He+p reaction: elastic scattering and neutron transfer reactions Investigation of the ^{6}He beam for the ^{6}He+p reaction at CRIB,” Workshop on Nuclear Cluster Physics (WNCP2023), Osaka, Japan, November 27–29, 2023.

17. F. L. Liu (poster), “Direct measurement of the cross section for ^{102}Pd(p, γ)^{103} reaction in the p-process,” The 22nd CNS International Summer School (A3F-CNSSS23), Nishina hall, RIKEN, Japan, August 4–10, 2023.

18. F. L. Liu (poster), “Direct measurement of the cross section for ^{102}Pd(p, γ)^{103} reaction in the p-process”, The 1st IReNA-Ukakuren Joint Workshop “Advancing Professional Development in Nuclear Astrophysics and Beyond”, National Astronomical Observatory of Japan (NAOJ), Mitaka, Tokyo, Japan, August 28–Sepember 1, 2023.

19. F. L. Liu (poster), “Direct measurement of the cross section for ^{102}Pd(p, γ)^{103}Ag reaction in the p-process,” 17th International Symposium on Nuclei in the Cosmos (NIC XVII), Daejeon, Republic of Korea, September 17—22, 2023.

20. R. Yokoyama (invited), “Future Programs at RIBF OEDO/SHARAQ: Utilizing Low Energy Heavy Ion Beams and Liq H2 Targets”, Direct reactions and spectroscopy with hydrogen targets: past 10 years at the RIBF and future prospects, Hilton York Hotel, July 31–August 4, 2023.

21. N. Imai (invited), “A new technique to determine gamma emission probability above the neutron threshold without gamma-ray detectors”, 17th International Symposium on Capture Gamma-Ray Spectrosopy and Related Topics CGS17, Grenoble, France, July 17–21, 2023.

22. N. Imai (invited), “Experimental study on neutron-capture rate using the decelerating and focusing device OEDO in RIBF”, 6th Joint Meeting of the APS Division of Nuclear Physics and the Physical Society of Japan, Hilton Waikoloa Village, Hawaii, USA, November 26–December 1, 2023.

23. T. Chillery (invited), “OEDO: Recent Studies using Energy-Degraded Beams and Future Perspectives”, 6th Joint Meeting of the APS Division of Nuclear Physics and the Physical Society of Japan, Hilton Waikoloa Village, Hawaii, USA, November 26–December 1, 2023.

24. R. Yokoyama (invited), “Decay spectroscopy of exotic nuclei at RIBF”, 6th Joint Meeting of the APS Division of Nuclear Physics and the Physical Society of Japan, Hilton Waikoloa Village, Hawaii, USA, November 26–December 1, 2023.

25. S. Hanai (invited), “Development of detection systems in the OEDO-SHARAQ beamline for RI beam experiments”, 6th Joint Meeting of the APS Division of Nuclear Physics and the Physical Society of Japan, Hilton Waikoloa Village, Hawaii, USA, November 26–December 1, 2023.

26. R. Yokoyama (oral) “Study of the fi-delayed multi-neutron emission process through fl-neutron spectroscopy of Gallium Isotopes”, 6th Joint Meeting of the APS Division of Nuclear Physics and the Physical Society of Japan, Hilton Waikoloa Village, Hawaii, USA, November 26–December 1, 2023.

27. N. Kitamura (invited), “OEDO-SHARAQ: achievements and prospects”, 2023 Annual Meeting of JSPS/NRF/NSFC A3 Foresight Program “Nuclear Physics in the 21st Century”, Xi’an, China, December, 2023.

28. N. Imai (invited), “Physics with the decelerated RI beams”, Advancing physics at next RIBF (ADRIB24), RIKEN Wako campus, January 23–24, 2024.

29. R. Yokoyama (invited), “Systematic beta3 measurement around octupole magic at Z = 56 and N = 88”, A3F-Workshop on frontier nuclear studies with gamma-ray spectrometer arrays, Osaka University Minoh Campus, March 26–28, 2024.

30. N. Kitamura (invited), “Detailed in-beam gamma-ray spectroscopy using GRETINA: the case of ^{32}Mg”, A3F-Workshop on frontier nuclear studies with gamma-ray spectrometer arrays, Osaka University Minoh Campus, March 26–28, 2024.

31. S. Hanai (invited), “Mass measurement in the vicinity of 2 proton emitters”, RCNP workshop Microscopic approach from pair correlation to pair condensation, RCNP, Osaka University, September 26–28, 2023.

32. T. Chillery (oral) “Astrophysical Reactions Important in r- and vp processes Measured Using (d,p) Transfer Reactions at OEDO-SHARAQ”, Nuclei in the Cosmos XVII, Daejeon, Korea, September 17–22, 2023.

33. N. Imai (oral) “Possible experiments with 8pi”, A3F-Workshop on frontier nuclear studies with gamma-ray spectrometer arrays (gamma24), Osaka University Minoh Campus, March 26–28, 2024.
34. S. Michimasa (oral) “OEDO-SHARAQ system: Its multifaceted performance and recent experimental achievements,” The 4th International Conference on Advances in Radioactive Isotope Science (ARIS 2023), Palais des Papes, Avignon, France, June 4–9, 2023.
35. J. T. Li (poster) “Development of a mosaic type array formed by Si photodiodes for charged-particle detection in heavy-ion collisions”, International Conference on Heavy-Ion Collisions at near-barrier energies (FUSION23), Shizuoka, November 15–19, 2023.
36. J. T. Li (poster) “Performance of the Si photodiodes for the ancillary detector of in-beam γ experiments”, A3F-Workshop on frontier nuclear studies with gamma-ray spectrometer arrays (gamma24), Osaka University Minoh Campus, March 26–28, 2024.
37. S. Hanai (poster) “Direct mass measurement of neutron-deficient Fe isotopes”, Advances in Radioactive Isotope Science (ARIS2023), Avignon, France, June 4–9, 2023.
38. D. Sekihata for the ALICE collaboration (oral), “Electromagnetic radiation in pp and Pb–Pb collisions with dielectrons in ALICE”, Quark Matter 2023-XXXth International Conference on Ultra-relativistic Nucleus-Nucleus Collisions (QM2023), September 3–9, 2023, Houston, Texas, USA
39. Y. Sekiguchi for the ALICE collaboration (poster), “Measurements of long-range two-particle correlation over a wide pseudorapidity range in p–Pb collisions at 5.02 TeV”, Quark Matter 2023-XXXth International Conference on Ultra-relativistic Nucleus-Nucleus Collisions (QM2023), September 3–9, 2023, Houston, Texas, USA
40. D. Sekihata for the ALICE collaboration (oral), “Electromagnetic radiation in ALICE at the LHC”, 52nd International Symposium on Multiparticle Dynamics (ISMD2023), August 21–26, 2023, Gyöngyös, Hungary
41. H. Murakami for the ALICE collaboration (oral), “Electromagnetic radiation in pp and Pb–Pb collisions with dielectrons in ALICE”, European Physical Society Conference on High Energy Physics (EPS-HEP2023), August 21–25, 2023, Hamburg, Germany
42. D. Sekihata for the ALICE collaboration (oral), “Low mass dielectron measurements in Pb–Pb collisions with ALICE at the LHC”, 9th Asian Triangle Heavy-Ion Conference (ATHIC2023), April 24–27, 2023, Hiroshima, Japan
43. H. Murakami for the ALICE collaboration (oral), “Dielectron production in high-multiplicity pp collisions at $\sqrt{s}$ = 13 TeV with ALICE”, 9th Asian Triangle Heavy-Ion Conference (ATHIC2023), April 24–27, 2023, Hiroshima, Japan
44. H. Baba for the ALICE collaboration (oral), “Studies of space-charge distortion corrections using machine learning techniques”, 9th Asian Triangle Heavy-Ion Conference (ATHIC2023), April 24–27, 2023, Hiroshima, Japan
45. Y. Sekiguchi (invited), “QGP in small systems (Experiment)”, 9th Asian Triangle Heavy-Ion Conference (ATHIC2023), April 24–27, 2023, Hiroshima, Japan
46. T. Gunji (oral), “Hadron Physics at EIC”, Fourth Internatinal Workshop on the Extention Project for the J-PARC Hadron Experimental Facility, February 19–21, 2024, Tokai, Japan
47. D. Sekihata (oral), “Overview of direct photon measurements at the LHC”, EMMI Rapid Reaction Task Force for Direct Photon Puzzle, July 24–27, 2023, Heidelberg University, Germany
48. T. Gunji (invited), “Online data processing using hardware accelerators for nuclear physics experiments”, 6th Joint Meeting of the APS Division of Nuclear Physics and the Physical Society of Japan, November 26–December 1, 2023, Waikoloa, Hawaii, USA
49. T. Gunji (invited), “Future prospects of hot and cold QCD physics at RHIC and LHC”, 6th Joint Meeting of the APS Division of Nuclear Physics and the Physical Society of Japan, November 26–December 1, 2023, Waikoloa, Hawaii, USA
50. H. Murakami for the ALICE collaboration (oral), “Dielectron production in high-multiplicity pp collisions at *sqrts* = 13 TeV with ALICE”, 6th Joint Meeting of the APS Division of Nuclear Physics and the Physical Society of Japan, November 26–December 1, 2023, Waikoloa, Hawaii, USA

51. H. Baba for the ALICE collaboration (oral), “Application of machine learning techniques for the ALICE TPC space-charge distortion correction and for particle tracking in Si detectors”, 6th Joint Meeting of the APS Division of Nuclear Physics and the Physical Society of Japan, November 26–December 1, 2023, Waikoloa, Hawaii, USA

52. S. Shindo for the ALICE collaboration (oral), “Simulation studies of Monolithic CMOS Si sensor with gain layer for timing measurements”, 6th Joint Meeting of the APS Division of Nuclear Physics and the Physical Society of Japan, November 26–December 1, 2023, Waikoloa, Hawaii, USA

53. Y. Sekiguchi for the ALICE collaboration (oral), “Measurements of long-range correlations and $v_2(\eta)$ in small system with ALICE”, 6th Joint Meeting of the APS Division of Nuclear Physics and the Physical Society of Japan, November 26–December 1, 2023, Waikoloa, Hawaii, USA

54. Y. Tsunoda (invited), “Large-Scale Shell-Model Calculations in Medium-Heavy Nuclei and Neutrinoless Double-Beta Decay Matrix Elements”, The 2023 Gordon Research Conference on Nuclear Chemistry, New London, USA, June 11–16, 2023.

55. Y. Utsuno (invited), “Overview of shell evolution in the $N = 28 - 40$ region,” Symposium on Direct reactions and spectroscopy with hydrogen targets: past 10 years at the RIBF and future prospects, York, UK, July 31–August 4, 2023.

56. Y. Tsunoda (invited), “Nuclear Structure in neutron-rich Ni region”, Symposium on Direct reactions and spectroscopy with hydrogen targets: past 10 years at the RIBF and future prospects, York, UK, July 31–August 4, 2023.

57. Y. Tsunoda, N. Shimizu, T. Otsuka (oral), “Structure of medium-mass nuclei studied by Monte Carlo shell model calculations”, Sixth Joint Meeting of the Nuclear Physics Divisions of the APS and The JPS (HAWAII 2023), Hawaii, USA, November 26–December 1, 2023

58. Y. Tsunoda (invited), “Nuclear structure studied by shell model calculations using two-nucleon amplitudes”, Reimei Workshop “Intersection of Nuclear Structure and Direct Reaction”, Tokai, Japan, February 28–March 1, 2024

59. Y. Tsunoda (invited), “Nuclear shapes studied by Monte Carlo shell model calculations”, The workshop on frontier nuclear studies with gamma-ray spectrometer arrays (gamma24), Minoh, Japan, March 26–28, 2024.

60. A. Sakaue (oral), “Search for double Gamow–Teller giant resonance using the double charge exchange $(^{12}\mathrm{C}, ^{12}\mathrm{Be}(0_2^+))$ reaction”, 6th Joint Meeting of the APS DNP and JPS, Hawaii, November 27, 2023.

61. M. Fukase (oral), “Present status of high intensity Fr source development to search for the EDM,” Symposium University of Tokyo - ETH Zurich - University of Zurich, ETH Zurich Hönggerberg Campus, October 15–17, 2023.

62. K. Nakamura (oral), “Current status of development of laser optics for Fr permanent electric dipole moment,” Symposium University of Tokyo - ETH Zurich - University of Zurich, ETH Zurich Hönggerberg Campus, October 15–17, 2023.

63. T. Nakashita (poster), “Search for Fundamental Symmetry by Trapping Francium Atoms,” Summit of Materials Science 2023 and GIMRT User Meeting 2023, Sendai, Japan, November 21, 2023.

64. H. Nagahama (oral), “Electron EDM search with laser-cooled heavy elements,” 6th Joint Meeting of the APS Division of Nuclear Physics and the Physical Society of Japan, Hawaii, the Big Island, November 26–December 1, 2023.

65. H. Nagase (oral), “Development of a novel comagnetometer for high-precision measurement of the electron’s electric dipole moment using laser-cooled francium atoms,” 6th Joint Meeting of the APS Division of Nuclear Physics and the Physical Society of Japan, Hawaii, the Big Island, November 26–December 1, 2023.

B. Domestic Conference

1. 小高康照 (ポスター発表),「理研 AVF サイクロトロンで加速される大強度イオンビーム用ペッパーポット型エミッタンス測定器開発の現状」, 第 20 回日本加速器学会年会, , 日本大学理工学部船橋校舎，2023 年 8 月 29-9 月 1 日.

2. 鎌倉恵太 (ポスター発表),「機械学習を用いた HyperECR イオン源制御の準備状況」, 第 20 回日本加速器学会年会, 日本大学理工学部船橋校舎, 2023 年 8 月 29-9 月 1 日.

3. 小高康照 (口頭発表),「AVF 入射ビーム横向き軌道に対する入射バンチャーの影響」, 第 21 回 AVF 合同打ち合わせ, 住友重機械工業西条工場, 2023 年 11 月 13 日.

4. 鎌倉恵太 (口頭発表),「東大 HyperECR イオン源の現状」, 第 21 回 AVF 合同打ち合わせ, 住友重機械工業西条工場, 2023 年 11 月 13 日.

5. 鎌倉恵太 (口頭発表),「東京大学 HyperECR イオン源機械学習制御に向けたビーム電流予測モデルの開発」, 加速器・ビーム物理の機械学習ワークショップ 2023, 理化学研究所仁科加速器科学研究センター, 2023 年 11 月 27 日-29 日

6. S. Hayakawa (oral), "Recent collaborations and activities at CRIB," RIBF Users Meeting 2023, Session 3, Wako, Saitama, Japan and online, 2023 年 9 月 6-7 日.

7. S. Hayakawa (invited), "CRIB で開拓する宇宙核反応測定", 第 12 回 停止・低速 RI ビームを用いた核分光研究会 (12th SSRI), Toshima, Tokyo, Japan, September 4-5, 2023.

8. N. Imai, "Study of the low-energy nuclear reaction at HIMAC", HIMAC における原子核物理学研究の展望, 理研仁科センター, November 17, 2023.

9. N. Kitamura,「高分解能波形ディジタイザ FW 開発の現状と展望」, The 2nd Workshop on Signal processing and data acquisition infrastructure (SPADI2024), 理研仁科センター, March, 2024.

10. 郡司 卓 (oral), "EIC/ePIC 実験での Streaming DAQ の開発と物理展望", 日本物理学会 2024 年春季大会, 2024 年 3 月 18–21 日, オンライン

11. 関畑 大貴 for the ALICE collaboration (oral), "LHC-ALICE 実験を用いた核子対あたり重心系エネルギー 5.02TeV 鉛+鉛衝突における電子対生成", 日本物理学会 2024 年春季大会, 2024 年 3 月 18–21 日, オンライン

12. 馬場 仁志 for the ALICE collaboration (oral), "機械学習とハードウェアアクセラレータを用いた MAPS シリコン検出器における飛跡再構成", 日本物理学会 2024 年春季大会, 2024 年 3 月 18–21 日, オンライン

13. 新堂 柊二朗 for the ALICE collaboration (oral), "ALICE3 実験に向けた CMOS-LGAD 検出器の時間分解能に関するシミュレーションを用いた研究", 日本物理学会 2024 年春季大会, 2024 年 3 月 18–21 日, オンライン

14. 小原 遼太郎 for the ALICE collaboration (oral), "ALICE-ITS3 アップグレードに向けた babyMOSS の性能評価", 日本物理学会 2024 年春季大会, 2024 年 3 月 18–21 日, オンライン

15. 関口 裕子 (oral), "フロー、粒子相関", 第 41 回 Heavy Ion Cafe & 第 38 回 Heavy Ion Pub 合同研究会, November 4, 名古屋大学, 名古屋, 日本

16. 村上 ひかり (oral), "電磁プローブ", 第 41 回 Heavy Ion Cafe & 第 38 回 Heavy Ion Pub 合同研究会, November 4, 名古屋大学, 名古屋, 日本

17. T. Gunji (oral), "ALICE3 and EIC", Platform B (Silicon) meeting : Semiconductor detectors for energy frontier experiments, July, 14, 2023, KEK, Japan

18. 宇都野穣（招待講演),「大規模殻模型計算による M1 バンドの解析」, RCNP 研究会「原子核におけるスピン自由度の織り成すダイナミクス」, 大阪府吹田市（大阪大学）, 2023 年 12 月 11–13 日.

19. 宇都野穣, 清水則孝, D. Patel, P. C. Srivastava（口頭発表),「殻模型計算による中性子過剰カドミウム同位体の四重極モーメントと変形の解析」, 日本物理学会 2024 年春季大会, オンライン, 2024 年 3 月 18–21 日.

20. 角田佑介（口頭発表),「モンテカルロ殻模型とその発展的手法による核構造の研究」,「成果創出加速」基礎科学合同シンポジウム, 東京都文京区（筑波大学東京キャンパス）, 2023 年 12 月 18–20 日.

21. Y. Tsunoda（招待講演), "Structure of medium-mass nuclei studied by Monte Carlo shell model", 日本物理学会 2024 年春季大会, オンライン, 2024 年 3 月 18–21 日.

22. 阪上朱音, 「二重荷電交換反応 (^{12}C, ^{12}Be(0_2^+)) を用いた二重ガモフ・テラー巨大共鳴の探索」, RCNP 研究会「原子核におけるスピン自由度の織り成すダイナミクス」, RCNP, 12 月 11 日。
23. S. Nagase (口頭発表), 「フランシウム永久電気双極子能率の精密測定に向けた光格子共存磁力計開発」, 第 5 回アトムの会, 名古屋, 2023 年 8 月.
24. 中村圭佑 (口頭発表), 「冷却 Fr 原子を用いた EDM 探索プロジェクトの開発状況」, 第 12 回 停止・低速 RI ビームを用いた核分光研究会（12th SSRI)、立教大学、2023 年 9 月.
25. 佐藤幹 (口頭発表) , 「225Ac を用いた 221Fr 原子線源の開発」, 大洗アルファ合同研究会, 東北大学東京分室, 2023 年 9 月 28 日.

C. Seminar Talks

1. T. Gunji, “High Energy QCD Physics”, International School for Strangeness Nuclear Physics, December 11–15, 2023, Tokai, Japan
2. D. Sekihata, “Electromagnetic probes in ALICE at the LHC”, Nuclear Physics Colloquium, November 16, 2023, Goete University Frankfurt, Germany
3. N. Imai, “OEDO, the deceleration and focusing device at RIBF, and the nuclear astrophysics program with OEDO”, GANIL, France, July 13, 2023.
4. N. Imai, “Direct reaction and r-process nucleosynthesis”, Nuclear Physics School For Young Scientists(NUSYS-2023), Fudan University in Shanghai, China, August 7–12, 2023.
5. N. Imai, “Direct reaction and r-process nucleosynthesis”, A3F-CNS Summer School 2023, August 4–10, 2023.

D. Lectures

1. K. Yako, H. Yamaguchi, Y. Sakemi: “Nuclear Physics III”, Summer, 2022.
2. K. Yako (with M. Ishino): “Experimental Techniques in Particle and Nuclear Physics”, Autumn, 2022.
3. H. Yamaguchi: “Hadron Physics” at Rikkyo University, Summer, 2022.
4. T. Gunji: “Physics Seminar”, Autumn, 2022.
5. K. Yako: “Classical Mechanics A for Undergraduate Students”, Summer, 2022.
6. N. Kitamura, K. Yako: “Physics Experiment II”, Autumn, 2023.
7. H. Yamaguchi, T. Gunji, S. Michimasa: “Experience Seminar for Freshmen and Sophomores”, Autumn, 2023.

E. Awards

1. J. T. Li, A3F-CNSSS23 Young Scientist Award, August 10, 2023.
2. S. Nagase, A3F-CNSSS23 Young Scientist Award, August 10, 2023.
3. M. Fukase, A3F-CNSSS23 Young Scientist Award, August 10, 2023.

Press Releases

1. N. Imai, “Measuring neutrons to reduce nuclear waste,” February 16, 2024.

Personnel

Director

SAKEMI, Yasuhiro	*Professor, Graduate School of Science* *Center for Nuclear Study*

Scientific Staff

YAKO, Kentaro	*Associate Professor*
IMAI, Nobuaki	*Associate Professor*
GUNJI, Taku	*Associate Professor*
YAMAGUCHI, Hidetoshi	*Lecturer*
MICHIMASA, Shin'ichiro	*Assistant Professor*
NAGAHAMA, Hiroki	*Assistant Professor*
KITAMURA, Noritaka	*Assistant Professor*

Visiting Scientists

UTSUNO, Yutaka	*JAEA*
NISHIMURA, Daiki	*Tokyo City University*
KAJINO, Toshitaka	*NAOJ*
HAMAMOTO, Ikuko	*Lund University*
HWANG, Jongwon	*IBS*
NAKAGAWA, Takahide	*RIKEN*
SHIMOURA, Susumu	*RIKEN*
SHIMIZU, Noritaka	*University of Tsukuba*
OTA, Shinsuke	*RCNP*
DOZONO, Masanori	*Kyoto University*

Technical Specialist

KOTAKA, Yasuteru

Technical Assistant

YAGYU, Masayoshi

Project Research Associates

HAYAKAWA, Seiya

SEKIHATA, Daiki

YOKOYAMA, Rin

KAMAKURA, Keita

Post Doctoral Associates

NAKAMURA, Keisuke

TSUNODA, Yusuke

CHILLERY, Thomas William

LIU, Fulong

Academic Specialist

KOJIMA, Reiko

SEKIGUCHI, Yuko

Assistant Teaching Staff

KAWATA, Keita

SAKAUE, Akane

MURAKAMI, Hikari

Graduate Students

HANAI, Shutaro

KOHARA, Ryotaro

OKAWA, Kodai

FUKASE, Mirai

NAGASE, Shintaro

LI, Jiatai

BABA, Hitoshi

SHINDO, Shujiro

Administration Staff

HOSO, Takeo

YAMAMOTO, Ikuko

KOTAKA, Aki

KISHI, Yukino

Committees

Steering Committee

OHKOSHI, Shin-ichi	*Department of Chemistry, Graduate School of Science, UT*
TSUNEYUKI, Shinji	*Department of Physics, Graduate School of Science, UT*
OGATA, Masao	*Department of Physics, Graduate School of Science, UT*
NAKAMURA, Satoshi N.	*Department of Physics, Graduate School of Science, UT*
WAKASA, Tomotsugu	*Department of Physics, Graduate School of Science, Kyushu University*
MORI, Toshinori	*International Center for Elementary Particle Physics, UT*
TAKAHASHI, Hiroyuki	*Department of Nuclear Engineering and Management, Graduate School of Engineering, UT*
SAKEMI, Yasuhiro	*Center for Nuclear Study, Graduate School of Science, UT*
YAKO, Kentaro	*Center for Nuclear Study, Graduate School of Science, UT*